EVALUTION OF S-SCHEME IRON TUNGSTATE/STRONTIUM TITANATE (Fe$_2$WO$_6$/SrTiO$_3$) COMPOSITE FOR VISIBLE LIGHT PHOTOCATALYSIS AND ANTIBACTERIAL STUDY

ZHAO LIANG

UNIVERSITI TUNKU ABDUL RAHMAN

EVALUTION OF S-SCHEME IRON TUNGSTATE/STRONTIUM TITANATE (Fe$_2$WO$_6$/SrTiO$_3$) COMPOSITE FOR VISIBLE LIGHT PHOTOCATALYSIS AND ANTIBACTERIAL STUDY

ZHAO LIANG

A project report submitted in partial fulfilment of the requirements for the award of Master of Engineering Science

Faculty of Engineering and Green Technology

Univeristi Tunku Abdul Rahman

January 2024

DECLARATION

I hereby declare that this project report is based on my original work except for citations and quotations which have been duly acknowledged. I also declare that it has not been previously and concurrently submitted for any other degree or award at UTAR or other institutions.

Signature   :   *Zhao Liang*

Name   :   ZHAO LIANG
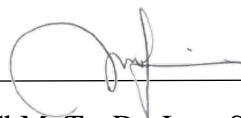
ID No.   :   21AGM01099

Date   :   08/01/24

APPROVAL FOR SUBMISSION

I certify that this project entitled "**EVALUTION OF S-SCHEME IRON TUNGSTATE/STRONTIUM TITANATE (Fe_2WO_6/$SrTiO_3$) COMPOSITE FOR VISIBLE LIGHT PHOTOCATALYSIS AND ANTIBACTERIAL STUDY**" was prepared by **ZHAO LIANG** has met the required standard for submission in partial fulfilment of the requirements for the award of Master of Engineering Science at Universiti Tunku Abdul Rahman.
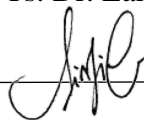
Approved by,

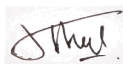Signature   _____

Supervisor   ChM. Ts. Dr. Lam Sze Mun

Signature   _____

Co Supervisor 1   ChM. Ts. Dr. Sin Jin Chung

Signature   _____

Co Supervisor 2   Dr. Ong Yit Thai

Date   :   08/01/24

Specially dedicated to

my beloved father, mother and sister.

ACKNOWLEDGEMENTS

EVALUTION OF S-SCHEME IRON TUNGSTATE/STRONTIUM TITANATE (Fe_2WO_6/$SrTiO_3$) COMPOSITE FOR VISIBLE LIGHT PHOTOCATALYSIS AND ANTIBACTERIAL STUDY

ABSTRACT

Discharge of industrial wastewater containing dyes and microorganisms was dangerous to the human health and ecosystem. Multifarious traditional strategies have been adopted for water purification. Heterogeneous photocatalysis was considered as a green and effective technology to solve environmental problems because it only relies on appropriate light to degrade organic contaminants into non-toxic substance or kill most microorganisms. In the present study, the iron tungstate/strontium titanate (Fe_2WO_6/$SrTiO_3$) composite was prepared by a hydrothermal method and employed in the photodegradation of rhodamine B (RhB) under visible LED light irradiation in 2 h. The prepared photocatalysts were characterized through FESEM, HRTEM, EDX, XRD, FTIR, UV-vis DRS and photoelectrochemical analyses. The Fe_2WO_6/$SrTiO_3$ composite demonstrated better visible light photoactivity for RhB in comparison with those of pure Fe_2WO_6 and pure $SrTiO_3$, respectively. The remarkable photoactivity was ascribed to its smaller band gap and effective charge carrier separation. The results of process parameter studies demonstrated that the optimized Fe_2WO_6 loadings were 20 wt%, photocatalyst dosage were 0.5 g L^{-1} and operated at pH 12. Besides, the antibacterial properties of the prepared photocatalysts were investigated on the bacteria inactivation towards *Escherichia coli* (*E. coli*) and *Bacillus cereus* (*B. cereus*). The Fe_2WO_6/$SrTiO_3$ composite showed the best antibacterial activity as compared to those of pure $SrTiO_3$ and pure Fe_2WO_6. Moreover, the radical scavenging experiment revealed that holes (h^+), hydroxyl (•OH) and superoxide anion (•O_2^-) radicals were major active radicals in the photocatalytic

process. Furthermore, the $Fe_2WO_6/SrTiO_3$ composite also displayed outstanding recyclability which attained high removal efficiency of 93.9% after five successive runs. Lastly, the optimized photocatalyst was used to degrade the real printed ink wastewater to reveal its potential application in the real wastewater purification. Overall, this study offered a novel $Fe_2WO_6/SrTiO_3$ photocatalyst that can be applied in degrading the organic contaminants and disinfecting the bacteria in the actual dye-containing wastewater.

TABLE OF CONTENT

LIST OF TABLES

LIST OF FIGURES

LIST OF SYMBOLS

2θ	Two Theta
A	Absorbance at specific λ
Å	Ångstöm
c	Concentration, mg L^{-1}
°C	Degree Celsius
g	Gram
h	Hour
l	Length of Light Transport Path, cm
L	Liter
M	Molarity
mm	Millimeter
nm	Nanometer
t	Time
$t_{1/2}$	Half-life
W	Watt
ε	Coefficient of Molar Absorption, L mol^{-1} cm^{-1}
λ	Wavelength, cm^{-1}
μA	Microampere

$\cdot O_2^-$	Superoxide Anion Radical
$\cdot OH$	Hydroxyl Radical
ABO_3	Perovskite Oxides
Ag	Silver
$AgFe_2O_4$	Silver Ferrite
$AgNPs$	Silver Nanoparticles
$AgNO_3$	Silver Nitrate
AgO	Silver Oxide
Ag_2O	Silver(I) Oxide
$AgVO_3$	Silver Vanadate
Ag_2WO_4	Silver Tungstate
$AgCl$	Silver Chloride
Au	Gold
$BaTiO_3$	Barium Titanate
Bi_2WO_6	Bismuth Tungstate
$BiFeO_3$	Bismuth Ferrite
Bi_2MoO_6	Bismuth Molybdate
$BiOBr$	Bismuth Oxobromide
Bi_2O_3	Bismuth(III) Oxide
BQ	Benzoquinone
C	Carbon
C_2H_5OH	Ethanol
C_2H_7NO	Ethanolamine
$CaFe_2O_4$	Calcium Ferrite

CdO	Cadmium Oxide
CeO_2	Cerium Oxide
$CoFe_2O_4$	Cobalt Ferrite
$CoAlMnO_4$	Permanganate
CO_2	Carbon Dioxide
Cu	Copper
CuO	Copper Oxide
Cu_2O	Cuprous Oxide
CuS	Copper Sulfide
$CuWO_4$	Copper Tungstate
$CuCr_2O_4$	Copper Chromite
EDTA-2Na	Ethylenediaminetetraacetate-disodium
Fe	Iron
$Fe(NO_3)_3 \cdot 9H_2O$	Iron (III) Nitrate Nonahydrate
Fe_2TiO_5	Pseudobrookite
FeV_2O_4	Iron Vanadium Oxide
Fe_2WO_6	Iron Tungstate
Fe_2O_3	Iron(III) oxide
$g\text{-}C_3N_4$	Graphitic Carbon Nitride
H^+	Hydrogen Ion
H_2O	Water
HCl	Hydrochloric Acid
H_2O	Water
H_2O_2	Hydrogen Peroxide

HCl	Hydrochloric Acid
$HO_2\bullet$	Hydroperoxyl Radical
MnO_2	Manganese Oxide
MnS	Manganese Sulfide
MoS_2	Molybdenum Disulfide
N	Nitrogen
Na_2SO_4	Sodium Sulphate
NaCl	Sodium Chloride
NaOH	Sodium Hydroxide
Na_2WO_4	Sodium tungstate
NH_4OH	Ammonia solution
$NiFe_2O_4$	Nickel Ferrite
O	Oxygen
O_2	Oxygen
O_3	Ozone
O_3/H_2O_2	Peroxone-process
OH^-	Hydroxide Ion
Pt	Platinum
rGO	Reduced Graphene Oxide
SnO_2	Tin(IV) Dioxide
Sr	Strontium
$SrTiO_3$	Strontium Titanate
$Sr(NO_3)_2$	Strontium nitrate
SR-AOP	Sulfate Radical-based Processes

$SO_4\bullet^-$	Sulfate Radical
Ti	Titanium
TiO_2	Titanium Dioxide
$Ti(OBu)_4$	Titanium butoxide
W	Tungsten
WO_3	Tungsten Trioxide
ZnO	Zinc Oxide
$ZnFe_2O_4$	Zinc Ferrite
$ZnIn_2S_4$	Zinc Indium Sulfide

LIST OF ABBREVIATIONS

AGS	Aerobic Granular Sludge
AOP	Advanced Oxidation Process
AOPs	Advanced Oxidation Processes
BOD	Biological Oxygen Demand
BQ	Benzoquinone
B. cereus	*Bacillus cereus*
B. subtilis	*Bacillus subtilis*
CB	Conduction Band
CIP	Ciprofloxacin
COD	Chemical Oxygen Demand
COD_i	Initial COD Value
COD_f	Final COD Value
DI	Deionized Water
DO	Dissolve Oxygen
DNA	Deoxyribonucleic Acid
E. coli	*Escherichia coli*
E. faecalis	*Enterococcus faecalis*
EC	Electrocoagulation
EF	Electro-Fenton

$e^- - h^+$	Electron-Hole Pair
e^-	Electron
EDX	Energy Disperse X-ray
EIS	Electrochemical Impedance
E_{EO}	Electrical Energy per Order
E_{fb}	Flat Band Potential
E_{CB}	Conduction Band Potential
E_{VB}	Valence Band Potential
Eg	Optical Band Gap Energy
Eq.	Equation
eV	Electron Volt
R	Reflectance
FEGT	Faculty of Engineering and Green Technology
FESEM	Field Emission Scanning Electron Microscopy
FTO	Fluorine doped Tin Oxide
FTIR	Fourier-transform Infrared Spectroscopy
h^+	Hole
hv	Photon Energy
HR	High Range
HPLC	High-performance Liquid Chromatography
IPA	Isopropanol
K. pneumoniae	*Klebsiella pneumoniae*
LC-MS	Liquid Chromatography-Mass Spectrometry
LED	Light Emitting Diode

LR	Low Range
LSV	Linear Sweep Voltammetry
M. luteus	*Micrococcus luteus*
MB	Methylene Blue
MBR	Membrane Bioreactor
MG	Malachite Green
MO	Methyl Orange
M-S	Mott Schottky
NP	Nanoparticle
OP	Oxidation Photocatalyst
P. aeruginosa	*Pseudomonas aeruginosa*
P. graminis	*Polymyxa graminis*
P. Vulgaris	*Proteus Vulgaris*
PL	Photoluminescence
RB 220	Reactive Blue 220
RhB	Rhodamine B
RP	Reduction photocatalyst
ROS	Reactive Oxygen Species
S. aureus	*Staphylococcus aureus*
S. pneumonia	*Streptococcus pneumonia*
TC	Tetracycline
TPR	Transient Photocurrent Response
UTAR	Universiti Tunku Abdul Rahman
UV	Ultraviolet

UV-vis DRS	UV-visible Diffuse Reflectance Spectroscopy
UV-Vis	Ultraviolet-Visible
VB	Valence Band
wt.%	Weight Percentage
Xe	Xenon
XPS	X-ray Photoelectron Spectroscopy
XRD	X-ray Diffraction
ZOI	Zone of Inhibition

CHAPTER 1

INTRODUCTION

1.1 Advanced oxidation process for pollutant destruction and bacteria disinfection

In recent years, rapid industrialization and continued population growth have led to a dramatic increase in water pollution. Generally, industrial wastewaters have more complex composition than other wastewater, which contains pollutants such as organic matter, nutrients, solids, heavy metals, dyestuffs, salinity and microorganism (Anantha et al., 2021). Discharge of industrial wastewater containing heavy metals, dyes and microorganisms was dangerous to the human and ecosystem (Singh et al., 2018). It was reported that lots of dyes were used in textile, printing industries of which approximately 20% was lost in wastewater because of the operations of processing (Kishor et al., 2021; Rafiq et al., 2021). These dye-containing wastewaters were toxic and non-biodegradable, and were harmful to the water body even at low concentrations (W. Li et al., 2019a). Consequently, development of efficient technologies for dyestuff wastewater remediation was of critical importance.

Multifarious strategies, such as adsorption, membrane filtration, ion-exchange, chlorination, ultraviolet irradiation and biological methods have been applied in wastewater treatment (Gusain et al., 2020). Nevertheless, high cost and the production of toxic by-products hinder their applications. Among many kinds of wastewater treatment technologies, advanced oxidation processes (AOPs) obtained extensive attention due to high efficiency, rapid reaction rate (Sgroi et al., 2021). AOPs can generate reactive oxygen species (ROS) to fully decompose organic contaminants as well as water sterilization.

AOPs comprise Fenton, Photo-Fenton, ozonation and photocatalytic oxidation according to different conditions (D. Ma et al., 2021). Heterogeneous photocatalysis was considered as a promising technology to solve environmental problems <mark>because it can rely on appropriate light and active photocatalyst</mark> to degrade organic contaminants into non-toxic substance or kill most of the microorganisms.

1.2 Problem Statement

Dyestuff can inhibit the growth of aquatic biota by hindering photosynthesis, and even endanger human health. Rhodamine B (RhB) was commonly found in wastewater from textile, paper and printing industries. This dye was a carcinogen, it can cause skin irritation, eye infection and liver damage (Ding et al., 2020). <mark>Experiments have proven that RhB was harmful to the surface water and living organisms even at low concentrations owing to its color rendering and non-biodegradability</mark> (Rafiq et al., 2021; Kishor et al., 2021; W. Li et al., 2019a). Recently, advanced oxidation processes (AOPs) show great potential in treating the dyestuff wastewater. One of AOPs was heterogeneous photocatalysis using semiconductor photocatalysts, which relies on appropriate light to decompose organic pollutants into innocuous substances like CO_2 and H_2O (P. Li et al., 2019b). Additionally, the photocatalysis was a surface-based process, so the microstructure and morphology of photocatalysts can affect the photocatalytic performance of photocatalysts (Dutta et al., 2021).

As a common semiconductor, strontium titanate ($SrTiO_3$) commonly applied for the actuators, photonics, bioelectronics and multilayer capacitor (Z. Yang et al., 2023; Fu et al., 2022; Y. Zhang et al., 2023). The $SrTiO_3$ with a wide band gap (3.4 eV) can be applied as photocatalysts in photocatalytic wastewater treatment and many other applications <mark>including CO_2 reduction, water splitting and microwave substrate (X. Li et al., 2021a; Z. Yang et al., 2023; Zeng et al., 2022; Pan et al., 2022).</mark> However, pure $SrTiO_3$ was easy to recombine and it can only respond ultraviolet (UV) light because it possessed

wide band gap. Thus, the photoactivity of pure $SrTiO_3$ was still limited in visible light. The combination of $SrTiO_3$ and smaller band gap semiconductors to construct $SrTiO_3$-based composites considered to be a promising strategy to address this problem.

On the other hand, iron tungstate (Fe_2WO_6) semiconductors with an inherently narrow band gap (1.5-1.7 eV). In addition, the Fe_2WO_6 possesses magnetism and transport properties and low cost. Other characteristics such as the photoelectrochemical activity, optical absorption and magnetodielectric properties have also become of interest (Lin et al., 2020). Heterojunction constructed by large-band and small-band gap semiconductors can enhance light absorption. Thereupon, small-band gap Fe_2WO_6 with suitable band edges was considered a suitable candidate to couple with large-band gap $SrTiO_3$ to form heterojunction (Rawal et al., 2014; H. Lin et al., 2020). The constructed heterojunction can boost the transport and separation of the photo-inducted charge and eliminate the relatively useless photoelectrons and photogenerated holes (J. Wang et al., 2020a; P. Xia et al., 2020).

Based on existing literature reports, the construction of novel $Fe_2WO_6/SrTiO_3$ heterojunctions as well as their photoactivity for RhB dyestuff and actual wastewater treatment and gram-negative bacteria (*E. coli*) and gram-positive bacteria (*B. cereus*) inactivation under visible Light Emitting Diode (LED) light irradiation have not been reported to date. The Fe_2WO_6 has narrow bandgap energy, which could absorb visible light. Therefore, the photodegradation and antibacterial studies were conducted in this study to evaluate the photoactivity of $Fe_2WO_6/SrTiO_3$ composites. Both the bacterial strains were chosen due to both they are common bacteria and extensively existed in water bodies.

1.3 Objectives

The aims of this study are:

1. To prepare and characterize the $Fe_2WO_6/SrTiO_3$ composites with different Fe_2WO_6 loadings through a simple solvothermal method.

2. To evaluate the photoactivity of the prepared composite by the degradation of RhB dye and inactivation of *E. coli* and *B. cereus* under visible LED light.

3. To investigate the intrinsic photocatalytic mechanism of the prepared composites using radical scavenger test.

4. To study the recyclability of the prepared composites over cycling tests.

1.4 Research scope

In current research, $Fe_2WO_6/SrTiO_3$ composites were prepared through a simple hydrothermal method. The RhB dye degradation and bacteria inactivation activities were observed under visible LED light irradiation. Various characterization analyses such as X-ray diffraction (XRD), field emission scanning electron microscope (FESEM), high resolution transmission electron microscopy (HRTEM), energy dispersive X-ray (EDX), Fourier-transform infrared spectroscopy (FTIR), UV-vis diffuse reflectance spectroscopy (UV-vis DRS) and photoelectrochemical analyses were carried out on the as-synthesized $Fe_2WO_6/SrTiO_3$ composites. Several process parameters including Fe_2WO_6 loading, initial RhB solution pH and photocatalyst dosage were conducted over the prepared composites. The photocatalytic mechanism of prepared $Fe_2WO_6/SrTiO_3$ composites were investigated using the radical scavenger test. The recycling and stability properties of the prepared samples were also studied. Finally, the real world viability of $Fe_2WO_6/SrTiO_3$ composites were be evaluated by treating the real industrial printing ink wastewater under sunlight irradiation.

CHAPTER 2

LITERATURE REVIEW

2.1 Dye-containing Industrial Wastewater

Global industrialization was rapidly expanding, resulting in the production of large amounts of wastewater. Industrial wastewater can have a serious impact on environment due to its complicated components, poor biodegradability, and high toxicity (L. Liu et al., 2021a). These industries such as textile, food colorant, ink industries, cosmetic, and printing were responsible for generating dye-containing wastewater (Shabir et al., 2022). Generally, the wastewater contained several toxic and harmful contaminants including heavy metals, nutrients, additives, dye compounds, plastics and pathogenic microorganisms (Dey et al., 2021). Due to the high organic content in the wastewater, there were also many microbiological pathogens present such as *E. coli*, *B.cereus*, *S. aureus* and *P. Vulgaris* (Shafi et al., 2021; Manikandan et al., 2021).

According to the statistical data, more than 10^5 kinds of dye were commercially present and applied for various industries. These dyes can be mainly classified into two groups based on raw materials. They can be further divided into different groups on the basis of their physicochemical properties (Varjani et al., 2020). The representation of dye classification was illustrated in Figure 2.1. Rhodamine B (RhB) was a cationic red dye used in paper, textile and printing industries (Adegoke et al., 2022). It has been proven medically that water polluted by RhB dye has the risks of carcinogenic and mutagenic, which can lead to the dysfunction of liver, brain even central nervous system (X. Gao et

al., 2016; Bello et al., 2019). Consequently, the suitable treatment of dye-containing wastewater was necessary before it was discharged into water bodies.
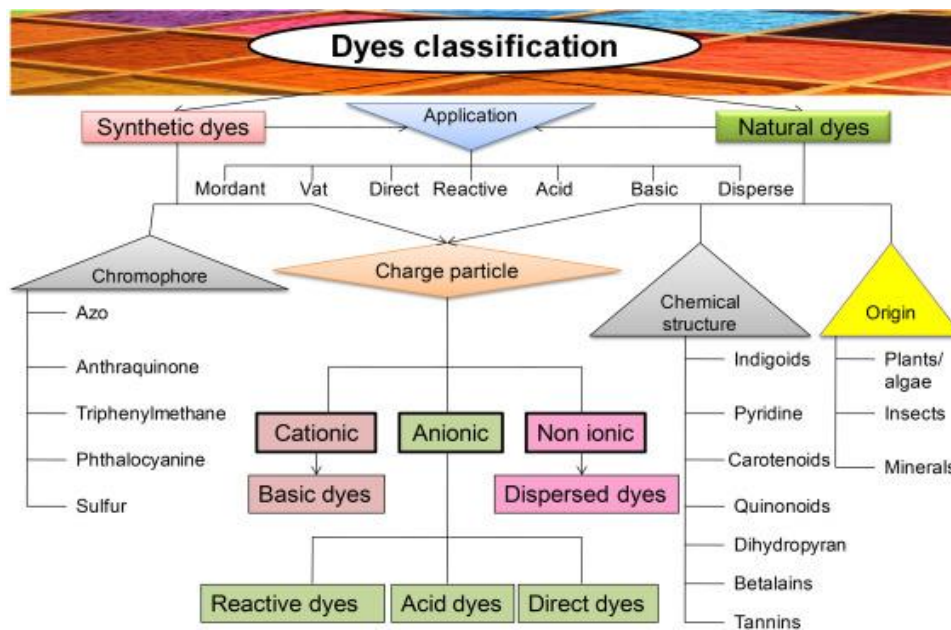
Figure 2.1: Schematic representation of dye classification (Mishra et al., 2021).

2.2 Wastewater Treatment Strategies

Dye-containing wastewater can be harmful since it contains substances with high chemical oxygen demand (COD), biochemical oxygen demand (BOD), surfactants, and other organic and inorganic chemicals. Different traditional techniques including physical, chemical, and biological processes were used to treat dye-containing wastewater.

2.2.1 Physical Treatment

Generally, physical treatment can be divided into four major processes for the physical processes, such as membrane separation, ion exchange, adsorption and coagulation. Adsorption has been adopted in wastewater treatment applications because of its feasible technique, simple and flexible operation. Adsorbents such as activated carbon, graphene, carbon nanotubes and bentonite clays were widely used in industry (W. Li et al., 2019a; Sahin et al., 2015). A study carried by Prasannamedha and co-workers (2021) primarily focused on the production of biochars from sugarcane bagasse through a hydrothermal carbonization method towards the removal of sulfamethoxazole from water (Prasannamedha et al., 2021). In their study, the prepared biochars can achieve the adsorption capacity of 400 mg g^{-1} through spontaneous reaction. The result suggested that the prepared biochars had great adsorption capability towards sulfamethoxazole. However, the use of adsorbents for the dye removal generated the secondary pollutants as these dye molecules stayed on the adsorbent and remained undegraded.

Besides, membrane filtration was another physical technique, which was widely used to remove dye and harmful pollutants from industrial wastewater (Vieira et al., 2020). This technique can be used to separate dyes from textile waste, but a big amount of dye was still preserved after filtration processes (Ezugbe et al., 2020). A study carried out by Ajibade and co-workers (2021) successfully fabricated a polyacrylonitrile membrane modified with composite for the removal of pollutant from wastewater (Ajibade et al., 2021). In their research, the composite membrane exhibited outstanding separation performance. This membrane displayed outstanding anti-corrosion properties in strong acidic or strong alkaline environment. However, the filtration process was not reused due to the risk of membrane clogging and had problems such as high cost and incompatibility.

2.2.2 Chemical Treatment

Chemical processes can be used to treat the toxic and recalcitrant nature of certain industrial wastewater. Examples of chemical treatments are ozonation, Fenton's reagents, electrochemical destruction and sodium hypochlorite. Ozonation was used in the wastewater treatment industry owing to high output and rapid process. Y. Xia and co-workers (2018) investigated the efficiency of the treatment of organics contaminated wastewater using ozone micro-nano-bubbles method. The COD removal efficiency of organics contaminated wastewater can reach 63% for 14 h, and showed an admirable mineralization activity. Nevertheless, this process was really pricey as more ozone was ineffectively employed when dealing with oxidized intermediates that were almost unable to further decompose (Egbuikwem et al., 2020).

Besides, Nidheesh et al. (2022) investigated the use of electro-Fenton (EF) and together with electrocoagulation (EC) processes of mixed industrial wastewater treatment efficiency. In their studies, the authors selected alkali modified laterite soil as a heterogeneous EF catalyst. The COD removal efficiency of the single EF treatment was 54.57% after 60 min. Afterwards, the EF treated wastewater underwent the EC process and a total of 85.27% COD removal was attained. However, applying a chemical treatment process for wastewater had some disadvantages. The cost of synthesis and fabrication for chemical treatments was often expensive, and the secondary pollutants such as sludge or flocks may be produced.

2.2.3 Biological Treatment

The biological processes were another traditional wastewater treatment technique which was widely employed for degrade numerous kinds of wastewater including high organic strength pollutants. Generally, it utilized fungus, algae, bacteria, plant and its enzymes to degrade high COD contaminants. Anaerobic and aerobic digestion were the two basic methods for biological treatment of wastewaters (C. Huang et al., 2017). The

conventional method of treating high strength textile effluent was the anaerobic process, combined with aerobic digestion to further improve the treatment efficiency. There were various biological treatment technologies that can be implemented in the dyestuff wastewater, including constructed wetland, phytoremediation, anaerobic and aerobic membrane bioreactor (Y. Hu et al., 2018; W. Chen et al., 2019; Yurtsever et al., 2021).

The membrane bioreactor (MBR) offered some advantages such as less sludge production, high removal of organic and nutrients and superior performance. Such a system was effective for treating both home and industrial wastewaters (Siddiqui et al., 2017). However, membrane fouling was still an issue of concern during the treatment of high-strength wastewater. Granule size was a crucial factor as it may affect the removal efficiency by affecting cake permeability and pore blocking. W. Zhang and Jiang (2019) investigated the effect of aerobic granular sludge (AGS) sizes on membrane fouling. In their research works, the AGS with 1-1.2 mm size were found to provide high membrane fouling than other sizes. Hence, the almost unavoidable membrane fouling leading to high cost of cleaning the membrane.

2.3 Advanced Oxidation Process

Advanced oxidation processes (AOPs) were the effective chemical procedures for wastewater treatment (Mahmoudi et al., 2022; Khajouei et al., 2022). AOPs were applied in the degradation of organic contaminants due to strong oxidation ability and high reaction speed in industrial wastewater treatment. Such processes relied on the reactive oxygen species (ROS) to degrade organic contaminants into non-toxic substance. Literature survey showed that AOPs based on the superoxide anion radicals ($\bullet O_2^-$), hydroxyl radical ($\bullet OH$) or sulfate radical ($SO_4 \bullet^-$) were very effective for wastewater treatment (Q. Yang et al., 2019; B. Miklos et al., 2018; Bhat and Gogate, 2021). Among these radicals, $\bullet OH$ with high oxidative potential at 2.8 eV was the main ROS in the majority of AOPs (Khajouei et al., 2022). Most commonly researched advanced oxidation

processes include Fenton, Photo Fenton, peroxone (O_3/H_2O_2), UV-based, and sulfate radical-based (SR-AOP) processes (Annabi et al., 2018; S. Gomes et al., 2018; Rehman et al., 2018; Zuo et al., 2022).

In recent years, AOPs have gained appeal in the industry wastewater treatment owing to its advantages over traditional wastewater treatment methods. The advantages such as effectively degrade recalcitrant organic components with less secondary production and high reaction speed. Among the AOPs methods, heterogeneous photocatalytic oxidation process under light irradiation was more promising method due to various advantages. The following list outlines the advantages of heterogeneous photocatalysis (Mahmoudi et al., 2022; H. Wang et al., 2022; Antonopoulou et al., 2021):

1. The milder reaction conditions,
2. The use of sunlight which was a cheap and sustainable resource,
3. The simple and flexibly process,
4. The production of ROS including superoxide anion ($•O_2^-$) and hydroxyl ($•OH$) radicals to completely decompose organic pollutants, and
5. Wide range of wastewater treatment applications such as textile, printing and oil wastewaters.

2.3.1 Principle of Heterogeneous Photocatalysis

The photocatalysis process utilizes a semiconductor that could be excited by light with a suitable energy to generate electron-hole pairs. In details, the photogenerated electrons (e^-) will be photoexcited from valence band (VB) of the semiconductor to the conduction band (CB), resulting in the generation of holes (h^+) in the VB (Thambiliyagodage 2022). In the aqueous solution, the h^+ oxidize hydroxide ion (OH^-) or water molecule (H_2O) and generating hydroxyl radical ($•OH$) radicals which represented in Eq. (2.2) (Shaban et al., 2018; T. Natarajan et al., 2017; X. Wu et al., 2022). In contrast,

recombination of the e^--h^+ pairs may also take place and produce heat as shown in Eq. (2.3) (Al-Mamun et al., 2019).

$$\text{Photocatalyst} + hv \rightarrow e^- + h^+ \qquad (2.1)$$

$$h^+ + H_2O/OH^- \rightarrow \bullet OH \qquad (2.2)$$

$$e^- + h^+ \rightarrow \text{energy} \qquad (2.3)$$
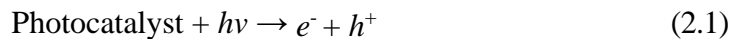
Furthermore, the e^- will reduce oxygen (O_2) to form superoxide radicals ($\bullet O_2^-$) and subsequently other oxidant species including hydroperoxyl radicals ($HO_2\bullet$) and hydrogen peroxide (H_2O_2) as shown in Eqs. (2.4) to (2.7) (F. Zhao et al., 2020; Ma, et al., 2021). These generated reactive oxygen species (ROS) including h^+, $\bullet O_2^-$ and $\bullet OH$ could further decompose various organic pollutants as represented by the Eq. (2.8) (Awfa et al., 2019). The basic mechanism of the photodegradation under light irradiation was illustrated in Figure 2.2.

$$e^- + O_2 \rightarrow \bullet O_2^- \qquad (2.4)$$

$$\bullet O_2^- + H^+ \rightarrow HO_2\bullet \qquad (2.5)$$

$$HO_2\bullet \rightarrow H_2O_2 + O_2 \qquad (2.6)$$

$$H_2O_2 + e^- \rightarrow OH^- + \bullet OH \qquad (2.7)$$

$$\text{Organic compounds} + ROS \rightarrow CO_2 + H_2O \qquad (2.8)$$
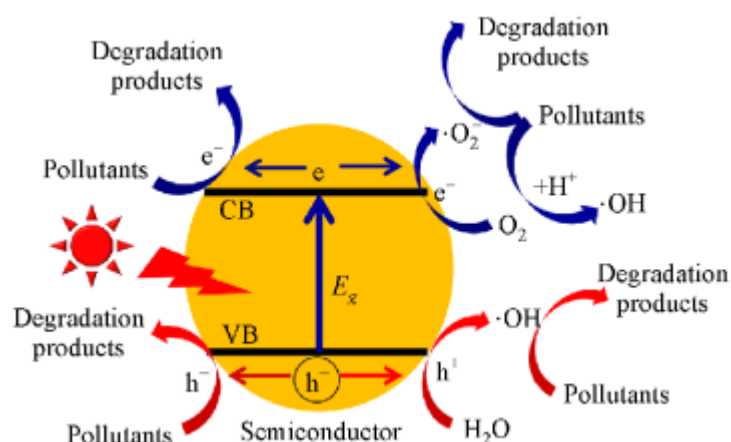
Figure 2.2: Schematic diagram of photodegradation under light irradiation (Li et al., 2018)

The semiconductor photocatalysis has been used in numerous organic pollutants decompositions, including the dyestuff wastewater, pharmaceutical waste, and greywater. In a literature study, G. Shen and co-workers (2022) had developed copper-doped zinc oxide coupled with graphitic carbon nitride (Cu-ZnO/g-C$_3$N$_4$) heterostructure for degrading ciprofloxacin (CIP), a common antibiotic found in pharmaceutical wastewater under visible light irradiation. In their study, the composites had achieved remarkable degradation efficiency of 95% after 6 hours. In addition, Priyanka and co-workers (2020) had studied the degradation of greywater using nitrogen-doped titanium dioxide (NP-TiO$_2$). In their works, NP-TiO$_2$ had attained a high greywater degradation efficiency (total organic carbon, TOC removal of 93.7%) under solar light radiation. Furthermore, O. Agboola and Shakir (2022) had constructed tin(IV) oxide/molybdenum disulfide/reduced graphene oxide (SnO$_2$/MoS$_2$/rGO) ternary photocatalyst towards the removal of methylene blue dye. When exposed to solar light irradiation, ternary composite had achieved remarkable removal efficiency of 90% in 75 min. As a result, the photocatalysis technology might be used in the several organic degrading processes that were mentioned.

2.3.2 SrTiO₃ Photocatalyst

The photocatalysis utilizing nanoscale photo-activated semiconductors, particularly metal oxide to generate the electron-hole pairs for photodegradation of organic pollutants. The reported metal oxides, such as titanium dioxide (TiO_2), zinc oxide (ZnO), tungsten oxide (WO_3), iron(III) oxide (Fe_2O_3) (P. Chen et al., 2018). TiO_2 was a commonly-used metal oxides with large band gap of 3.2 eV have been widely used for wastewater treatment, water splitting, building cleaning facades and so on (Yao et al., 2020; J. Xu et al., 2020). However, it was limited by its wide band gap, which can merely work under ultraviolet (UV) light accounting for only 4% intensity of solar radiation, resulting insufficient use of visible light region which accounted more than 45% of the total solar region. (Grabowska et al., 2016). Consequently, the visible light-driven photocatalyst had becoming researchers' focus for photocatalytic applications.

In comparison to simple metal semiconductors including TiO_2, ZnO, WO_3, Fe_2O_3, the perovskite oxides (ABO_3) have gained much attention in photocatalytic wastewater treatment owing to stable perovskite structure and outstanding photoelectrochemical properties (Wei et al., 2021; M. Zhou et al., 2020). As a typical perovskite oxide, strontium titanate with wide band gap was a suitable material for photocatalytic reaction due to it can produce reactive radicals including superoxide anion ($•O_2^-$) and hydroxyl ($•OH$) radicals. In addition, it has flexible crystal structure, good photo stability and chemical stability (Eskandari et al., 2019; Han et al., 2019). Owing to its outstanding properties, this titanate widely applied for the actuators, photonics, and bioelectronics applications, multilayer capacitor (Eskandari et al., 2019). However, the photocatalytic activity for bare $SrTiO_3$ was still limited under sunlight irradiation due to its wide band gap. Therefore, some researchers have proposed various modification strategies approach to solve this issue (Kumar et al., 2022; I. Ahmad et al., 2022).

Mesoporous-assembled $SrTiO_3$ nanocrystals was prepared by Puangpetch and co-workers (2008) through a sol–gel method. In their study, 98% of 10 mg/L methyl orange (MO) was degraded after 180 min photocatalysis under UV light irradiation. In another

study, S. Huang et al., 2014 synthesized strontium titanate ($SrTiO_3$) nanocubes through the autoclave hydrothermal treatment under the alkaline condition at 130 °C. The as-prepared $SrTiO_3$ was achieved crystal violet (CV) degradation at 99% in 24 h under the UV light radiation. On the other hand, H. Gao and co-workers (2018) fabricated the cubic $SrTiO_3$ using commercial P25 TiO_2 and $Sr(OH)_2 \cdot 8H_2O$ powders by a hydrothermal method. Under irradiation of a 150W xenon lamp, a degradation of rhodamine B (RhB) dye was obtained at 32% within 180 min. These researches showed that wide band gap limited the photocatalytic activity of pure $SrTiO_3$ photocatalyst.

2.3.3 Photocatalyst Modification Strategies

The heterojunction was defined as the interface between two different semiconductors with unequal band structure (Ranjit and Viswanathan 1997). It was well known that the low photocatalytic efficiency was the main limitation for photocatalysts (Meng et al., 2019; D. Huang et al., 2019). The rapid recombination of photo-inducted carriers was one of the reasons for the low photocatalytic efficiency. Besides, insufficient sunlight absorption and weak redox capacity were two other shortages for an ideal photocatalyst (Y. Xu et al., 2020; Lin et al., 2018). For a single photocatalyst, a large band gap with high CB and low VB values was beneficial when only considering the redox capacity. However, when taking broad light absorption into account, the narrow band gap of photocatalyst was more suitable. Afterwards, it was almost impossible for a single photocatalyst to satisfy these conditions at the same time. Hence, constructing heterojunction using two or more photocatalysts has been considered to be a promising way to form an ideal photocatalyst.

W. Zhang and co-workers (2022a) constructed the novel Z-scheme bismuth tungstate/strontium titanate ($Bi_2WO_6/SrTiO_3$) composite via a hydrothermal method towards the degradation of rhodamine B (RhB) dye observed under visible light irradiation. In their studies, the degradation efficiency of the composite could reach 71.1% in 100 min, which displayed better photocatalytic performance than pure photocatalyst. The authors

explained that Z-scheme heterojunction enhanced the redox capacity of Bi_2WO_6 and $SrTiO_3$. In other studies, Niu et al. (2022) successfully constructed a magnetic γ-Fe_2O_3/$SrTiO_3$ composite using a one-step microwave method towards the decomposition of methylene blue (MB) and tetracycline (TC) observed under visible light irradiation. The results of PL analysis proved that the prepared composite enhanced the separation of photogenerated electron-hole pairs. Table 2.1 depicts the various $SrTiO_3$-based catalysts with their synthesis methods associated with the photodegradation efficiency. It was found that many researchers have modified pure $SrTiO_3$ by constructing a heterojunction with another semiconductor to improve the photoactivity of pure $SrTiO_3$.

2.3.4 Fe_2WO_6 Photocatalyst

As aforementioned, the major drawbacks of utilizing wide band gap $SrTiO_3$ as single semiconductor photocatalyst in pollutants photodegradation was insufficient utilization of visible light due to wide band gap energy. Thus, it was almost impossible for a single photocatalyst to apply in real industrial wastewater treatment system. To overcome the limitation of single photocatalyst, constructing heterojunction using two or more photocatalysts was introduced (G. Zhao, et al., 2021). Therefore, the iron-based oxides photocatalyst were considered a suitable candidate. Iron tungstate (Fe_2WO_6) nanoparticle has great photoelectrochemical activity and transport properties with narrow bandgap between 1.5 to 1.7 eV which possessed strong visible light absorption, non-toxic, and environmentally benign character (Hassanpour et al., 2020; Caubergh et al., 2021; H. Lin et al., 2020). According to the literatures, the VB potential of Fe_2WO_6 photocatalyst was about 2.8 eV, suggesting that its VB potential was more positive in comparison to that of $SrTiO_3$ (2.1 eV) (Rawal et al., 2014; Qu et al., 2020). Due to its properties, it has been used for lithium-ion batteries and photoelectrode materials (Abdi et al., 2017; Espinosa-Angeles et al., 2021).

Table 2.1: The Synthesis of Various SrTiO$_3$-based Catalysts with Respective to Degradation Efficiency.

SrTiO$_3$-based composite	Synthesis method	Pollutant and concentration	Light source	SrTiO$_3$ loading	Removal efficiency	Reference
Bi$_2$WO$_6$/SrTiO$_3$	Hydrothermal	Rhodamine B, 8 mg/L	Xenon lamp, 300 W	Bi$_2$WO$_6$:SrTiO$_3$= 1:3	71.1% within 100 min	W. Zhang et al., 2022a
SrTiO$_3$/NiFe$_2$O$_4$	Sol-gel	Rhodamine B, 20 mg/L	Xenon lamp, 500 W	NiFe$_2$O$_4$:SrTiO$_3$ = 17:3	97.6% within 120 min	Y. Xia et al., 2018
SrTiO$_3$/Fe$_2$TiO$_5$	Co-precipitation	Methylene blue, 11 mg/L	Xenon lamp, 180 W	Fe$_2$TiO$_5$:SrTiO$_3$ = 1:9	100%	Alimohammadi et al., 2022
γ-Fe$_2$O$_3$/SrTiO$_3$	Sol-gel	Methylene blue, 10 mg/L	Xenon lamp, 150 W	γ-Fe$_2$O$_3$:SrTiO$_3$ = 3:997	84.9% within 150 min	Niu et al., 2022
SrTiO$_3$/CoAlMnO$_4$	Sol-gel	Methylene blue, 10 mg/L	Xenon lamp, 300 W	-	82.5% within 90 min	Valian et al., 2022
SrTiO$_3$/g-C$_3$N$_4$	Polymeric precursor method	Methylene blue, 10 mg/L	Visible light	g-C$_3$N$_4$:SrTiO$_3$ = 99:1	41%	Ferreira et al., 2020
BaTiO$_3$/SrTiO$_3$	Electrospinning	Rhodamine B, 8 mg/L	LED UV lamp, 30 W	BaTiO$_3$:SrTiO$_3$ = 1:10	97.4% within 30 min	X. Liu et al., 2021b

2.3.5 Type of Heterojunctions

Heterojunction photocatalysts were constructed by coupling two or more semiconductor photocatalysts. According to the band alignment between two semiconductors, the heterojunctions can be categorized as different types, as depicted in Figure 2.3 (X. Li et al., 2021a). In Type II heterojunctions, the photogenerated electrons and holes will flow to their respective low energy bands. Afterwards, the physical separation of electrons and holes will boost photocatalytic performance. However, due to the photogenerated charge carriers gather in the low energy bands, the redox capacities of the photogenerated charge carriers will be weakened. Conversely, when there exists a charge transfer from the conduction band of one semiconductor to the valence band of the other semiconductor, an effective Z-scheme heterojunction was constructed (Low et al., 2017; S. He et al., 2019). This heterojunction not only separate the electrons and holes, but also maintain the strongly oxidation and reduction abilities of the electrons and holes (Qiao et al., 2019; Dong et al., 2020).
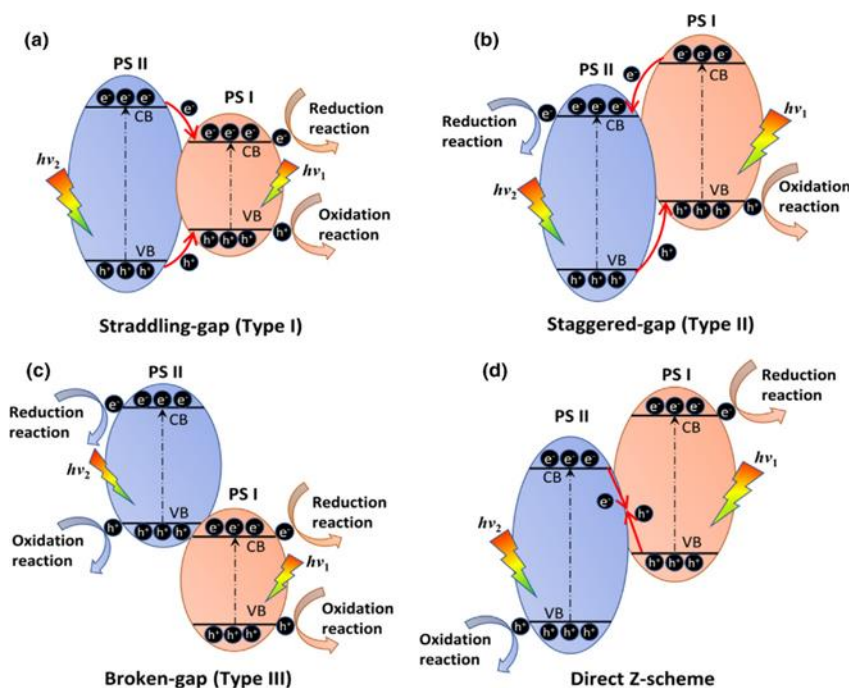
Figure 2.3: Band structures in (a) Type I, (b) Type II, (c) Type III, and (d) direct Z-scheme heterojunction (X. Li et al., 2021a)

Kokilavani and co-workers (2021) constructed the manganese sulfide/silver tungstate (MnS/Ag$_2$WO$_4$) heterojunction using a co-precipitation technique. In their studies, the photocatalyst efficiency of composite was superior with removal of 92.3% compared to bare components. The results showed that enhanced redox ability and effective separation of photo-inducted charge carriers owing to its heterojunction. X. Li et al. (2021b) synthesized a novel S-scheme heterojunction S-pCN/WO$_{2.72}$ via a solvent evaporation method towards the removal of tetracycline (TC) and rhodamine B (RhB) observed when exposed to visible light irradiation. In their studies, the composite has superior photocatalytic activity because its heterojunction can effectively separate the photogenerated charge carriers.

Among these type of heterojunctions, S-scheme was the more promising heterojunction due to various advantages. Effective separation of electron-hole (e^-- h^+) pairs and strong redox capacities were the advantages of S-scheme heterojunction (Y. Xu et al., 2020; X. Li et al., 2021b; X. Chen et al., 2022). In an S-scheme heterojunction, the powerful generated e^- in the conduction band (CB) of reduction photocatalysts (RP) and the h^+ in the valence band (VB) of oxidation photocatalysts (OP) were preserved to engage in photocatalytic reactions, while the useless e^- and h^+ recombine (F. He et al., 2020; Mu et al., 2020). In detail, the built-in electric field and energy band bending eliminated the relatively useless electrons and holes through recombination, which was regarded as the main driving forces for the charge migration.

W. Wang and co-workers (2020b) constructed the S-scheme heterojunction photocatalyst using sulfur-doped graphitic carbon nitride and titanium dioxide by an electrospinning technique. In their studies, they explained that the effects of electric field and band edge bending facilitated the recombination of relatively useless electrons and holes when the photocatalyst was exposed to simulated solar light. At the same time, the retained electrons and holes had a strong redox capacity, which making the photocatalyst have a strong redox ability. Chen et al. (2022) prepared the Bi$_7$O$_9$I$_3$/Cd$_{0.5}$Zn$_{0.5}$S QDs/WO$_{3-x}$ heterojunction photocatalyst via a simple hydrothermal method. The ternary heterojunction has good photoactivity, which was ascribed to the rapid separation of photogenerated carriers and broad light absorption range.

2.4 Process Parameter Studies

Photocatalytic wastewater treatment process was affected by several process parameters, like the initial pollutant concentration, solution pH, catalyst dosage, light intensity (Rafiq et al., 2021; S. Natarajan et al., 2018). In the present study, these parameters including photocatalyst loading, solution pH will be discussed.

2.4.1 Photocatalyst Dosage

One of the important process parameters that directly affects the photocatalytic performance was the photocatalyst dosage. Generally, with the increase of the photocatalyst loading, the photodegradation efficiency of pollutants by photocatalysis will increase (Mahendran et al., 2021; Vigneshwaran, et al., 2021). Numerous studies were conducted to examine how photocatalyst dosage affected photocatalytic performance. The photocatalyst dosage will affect the reactive oxygen species (ROS) generation and the light absorptivity in aqueous (Zhu et al., 2018; Xie et al., 2021). The active sites on the photocatalyst surface increased with photocatalyst dosage (Behzadifard, et al., 2018; Ghorai, et al., 2021a). However, the photocatalytic degradation performance might be deteriorated by excess photocatalyst dosage. The excessive amount of catalyst will intensify catalyst aggregation which leads to the reduction of active sites for the generation of ROS. Moreover, the solution will become turbid beyond a certain limit of photocatalyst dosage. Afterwards, the photoexcitation process for producing electron-hole pairs was hindered, which resulted in recombination of the charge carriers.

Kokilavani and co-workers (2021) have constructed the novel sanganese sulfide/silver tungstate (MnS/Ag$_2$WO$_4$) composites via a chemical co-precipitation method. In their studies, the increase in the composite amount from 1 mg to 4 mg in photodegradation of methylene blue, the degradation efficiency had enhanced from 42% to 92%. When the photocatalyst dosage was further increased to 5 mg, a slight reduction in photodegradation efficiency to 78%. Ghorai et al (2021b) synthesized copper

chromite/bismuth oxobromide ($CuCr_2O_4/BiOBr$) nanocomposite towards the removal of RhB were observed. The findings demonstrated that the removal efficiency increases from the photocatalyst dosage of 20 mg to 25 mg and then decreases with further increase of photocatalyst dosage. Therefore, in order to effectively degrade pollutants, the amount of photocatalyst needed to be limited. Otherwise, the degradation rate will decrease when the photocatalyst dosage exceeded a certain limit.

Some researchers also reported the photocatalyst dosage affects the photocatalytic activity in antimicrobial study. Janani and co-workers (2021) have synthesized (FeV_2O_4/Bi_2O_3) composites by ultra-sonication method to test its antimicrobial performance against *Escherichia coli* and *Bacillus subtilis*. Their studies showed increase in the photocatalyst dosage ranging from 0.1 to 50 mg L^{-1}, the bacteria growth inhibition also increased significantly. Kokilavani et al (2021) synthesized novel MnS/Ag_2WO_4 photocatalyst towards the *B. subtilis* and *E. coli* inhibition were observed. It was observed that antimicrobial activity increases from the photocatalyst dosage of 0.1 to 50 mg/L. The generation of more ROS and dense metal ions that cause the penetration of cations in bacteria cell membranes were two possible mechanisms explaining why antibacterial actions were boosted when the concentration of the catalyst was increased (Balasurya, et al., 2021). Table 2.2 depicts the various photocatalysts with their photocatalyst dosage associated with the photoactivity. It was discovered that many researchers conducted the parameter study of photocatalyst dosage to determine the optimum photocatalyst dosage and explore the effect of photocatalyst dosage on activity.

Table 2.2: The Photoactivity with Respective to the Photocatalyst Dosage.

Photocatalyst	Synthesis method	Pollutant (or bacteria)	Light source	Photocatalyst dosage	Removal efficiency	Reference
MnS/Ag_2WO_4	Chemical co-precipitation	Methylene blue, 10 mg/L	halogen-tungsten lamp, 800 W	1-5 mg	42-92% within 100 min	Kokilavani et al., 2021
$CuCr_2O_4/BiOBr$	Facile single pot precipitation	Rhodamine B, 10 mg/L	cool LED lamp, 50 W	20-50 mg	90-95%	Ghorai et al., 2021b
$CdO/CaFe_2O_4$	Sonochemical co-precipitation	Methylene blue, 25 mg/L	halogen-tungsten lamp, 800 W	5-20 mg	66-87%	Syed et al., 2021a
ZnO/Bi_2MoO_6	Solvothermal	Rhodamine B, 10 mg/L	Panasonic cool daylight lamp, 15W	25-75 mg	45-92%	Chankhanitta and Nanan, 2021
MnS/Ag_2WO_4	Chemical co-precipitation	*E. coli* and *B. subtilis*	halogen-tungsten lamp, 800 W	0.1-50 mg L^{-1}	66-99.9% and 64-99.9%	Kokilavani et al., 2021
FeV_2O_4/Bi_2O_3	Sonochemical co-precipitation	*E. coli* and *B. subtilis*	halogen lamp, 500 W	0.1-50 mg L^{-1}	27-99% and 15-99%	Janani et al., 2021
$AgFe_2O_4/BiFeO_3$	Hydrothermal method	*H. pylori* and *B. cereus*	Xenon lamp, 400 W	0.1-50 mg L^{-1}	56-92% and 20-82%	Mao et al., 2022

2.4.2 Solution pH

For the photodegradation of pollutants, pH was the most considerable process parameters as it can affect the rates of dye photodegradation in numerous ways. These properties including the band edge position, degree of dissociation, and the surface charges were significantly affected by pH of a given solution (Xue et al., 2020; Vigneshwaran et al., 2022). A literature study reported by Lin, et al (2018) in treating the malachite green (MG), the increase in the pH of solution from 2.98 to 11.01, the degradation efficiency was increased from 42% to 100%. This can be ascribed that in the acidic condition, the surface of the catalyst existed as positively charge. Therefore, H^+ ions competing with MG molecules for adsorption sites of photocatalysts result in an unsatisfactory photocatalytic performance in the acidic solution.

Furthermore, Shetty (2021) had studied the removal efficiency of reactive blue 220 (RB 220) using the titanium dioxide embedded silver oxide/silver(I) oxide (AgO/Ag$_2$O@TiO$_2$) photocatalyst. By varying the solution pH from 3 to 11, the photodegradation efficiency had declined 90% to 50% within 30 min. They explained that the better photocatalytic performance in an acidic environment was due to the adsorption of dye molecules to positively charged photocatalysts by electrostatic attraction. Another literature study reported by Dou, et al (2022) in treating the MB dye through the magnetic Fe$_2$O$_3$/g-C$_3$N$_4$. According to results, the increase in the pH value from 2 to 8, an increasing trend in the photodegradation of MB was obtained. The remarkable photodegradation performance appears at pH 8 (94.8 %). This revealed that MB molecules performed strong electrostatic repulsion from the photocatalyst with a positively charged surface at acidic condition.

2.5 Photocatalytic Antimicrobial Studies

Infectious diseases were mostly brought by polluted water because it contained a variety of microorganism species. Normally, the pathogenic microorganisms included bacteria, viruses, and fungi. Numerous illnesses were brought on by common gram-negative bacteria, including *E. coli* (food poisoning), *K. pneumonia* (pneumonia, meningitis, wound or surgical site infections), *P. Vulgaris* (wound infections and urinary tract infections) (Datta et al., 2021; Shafi, et al., 2021; Corzo-Ríos, et al., 2020). As the gram-negative bacteria species, *B. cereus* may cause gastroenteritis, vomiting, endophthalmitis, respiratory tract infections. Thus, the development of a potent technique to remove microorganisms from wastewater was imperative. Photocatalysis was safer technology for water disinfection, unlike other conventional water disinfection methods. Photocatalysis had the various advantages of low energy consumption, simple process and good stability (J. Gao et al., 2022). Therefore, photocatalysis has become a promising green method for the inactivation of pathogenic microorganisms. In current study, common bacteria *E. coli* and *B. cereus* which represented the gram-positive and gram-negative bacteria was selected.

The antimicrobial activities could be determined through the agar disk diffusion, well diffusion and plug diffusion methods (Balouiri et al., 2016; Vignesh et al., 2019). Figure 2.4 illustrates various agar diffusion methods. Agar well diffusion method can be used to test the antibacterial performance of photocatalysts. Madhukara Naik et al (2019) prepared the zinc ferrite ($ZnFe_2O_4$) nanoparticles and studied the photocatalytic antibacterial activity by Agar well diffusion assay. Vasantharaj, et al. (2021) synthesized zinc oxide (ZnO) photocatalyst towards the *E. coli* and *S. aureus* inhibition were was tested using the well diffusion method. Bhagat et al (2018) reported green synthesis of silver nanoparticles (AgNPs) and the antimicrobial activities of AgNPs were evaluated by agar well diffusion method. The zone of inhibition (ZOI) enables us to directly visualize the inhibitory potency of the photocatalysts.
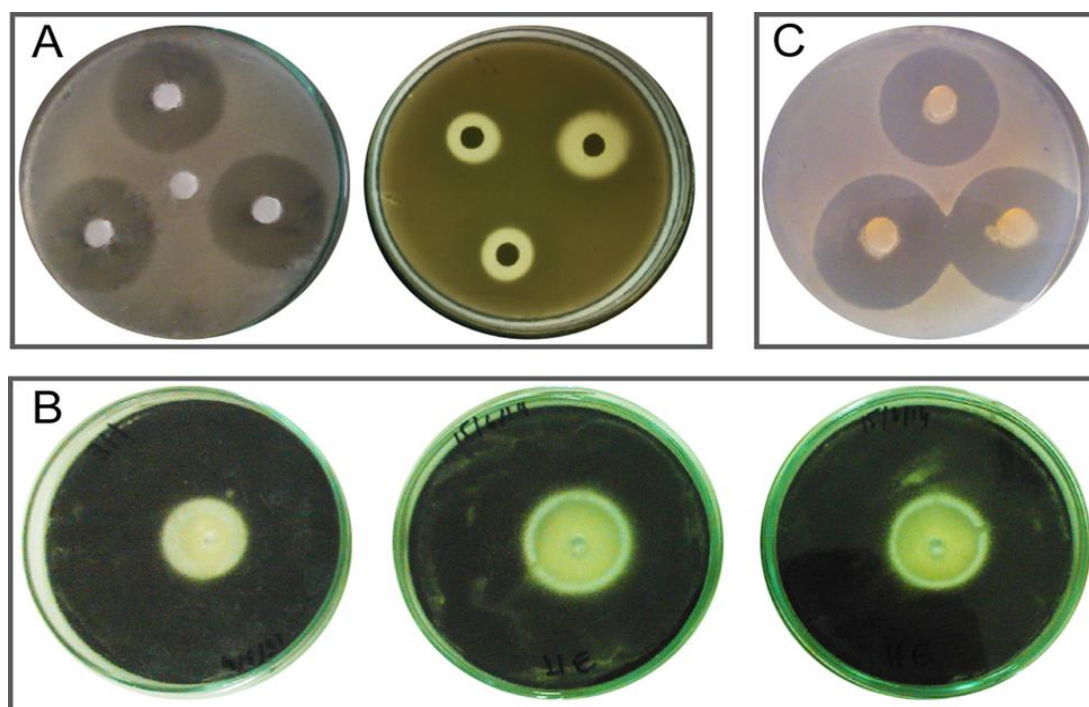
Figure. 2.4: Various agar diffusion methods (Balouiri et al., 2016).

Besides, Y. Zhang et al. (2022b) also determined the antimicrobial activities of photocatalysts using the colony counting method on plate which was observed under a fluorescence microscope. Y. Zhang and co-workers (2022b) conducted the photocatalytic inactivation of *E. coli* using the synthesized ternary C-dots/Cu$_2$O/SrTiO$_3$. The inactivation of bacteria can be observed through the photographs. Less bacteria stains were obtained for bacteria colonies when the ternary C-dots/Cu$_2$O/SrTiO$_3$ were used as compared to pure SrTiO$_3$ or Cu$_2$O. In another study, Tang et al. (2022) fabricated PE-TiO$_2$/Au towards the *S. aureus* and *E. coli* inhibition were determined by bacterial colony formation assay. To further evaluate the antimicrobial performance of as-synthesized photocatalysts, the researchers also used the scanning electron microscope and fluorescent microscopy to study the changes in morphology of bacteria (Tang et al., 2022). Table 2.3 depicts the various photocatalysts with their synthesis methods associated with the antibacterial efficiency. Comparatively, the composite had greater inhibition of growth than single photocatalyst, which indicated the enhanced antimicrobial performance of composite.

Table 2.3: The Synthesis of Photocatalyst with Respective to Antibacterial Efficiency.

Catalyst	Synthesis method	Microbe	Antibacterial efficiency	Reference
TiO_2/WO_3	Hydrothermal	*E. faecalis* and *M. luteus*	ZOI*: 13.4, 11.3 mm	Fakhri et al., 2018
ZnO/Fe_2O_3	Green synthesis	*K. pneumonia, E. coli and S. aureus*	ZOI*: 16.0, 14.0, 26.0 mm	Nachimuthu et al., 2022
TiO_2/SnO_2	Sol-gel and precipitation	*S. aureus*	ZOI*: 36 mm	Gnanasekaran et al., 2022
ZnO/CuO	Hydrothermal	*E. faecalis* and *M. luteus*	ZOI*: 14.2, 12.1 mm	Fakhri et al., 2018
$CuO/CuWO_4$	Hydrothermal	*E. coli and P. graminis*	ZOI*: 18.2, 15.2 mm	Cai et al., 2021
$ZnIn_2S_4/Ag_2MoO_4$	Electrospinning and in-situ precipitation	*S. aureus, B. subtilis, P. aeruginosa, and E. coli*	ZOI*: 14.8, 11.2, 11.6, 15.6 mm	S. Li et al., 2022
CMgF@rGO	Ultra-sonication	*K. pneumonia and S. aureus*	ZOI*: 7.0, 10.0 mm	Alhashmialameer et al., 2022

2.6 Summary

The characteristics of the dye-containing industrial wastewater has been firstly discussed in this chapter. It was then followed by numerous treatment technologies reported in treating the real dyestuff wastewater. Each of the treatment technologies had different advantages and disadvantages in eliminating the contaminants in wastewater. The basic mechanism of heterogeneous photocatalysis was also stated to understand the process. Pure $SrTiO_3$ photocatalyst was a promising candidate in photocatalysis due to unique physicochemical and optical properties. However, wide band gap restricted its photocatalytic activity under visible light. Thereupon, this catalyst can be also further improved its photoactivity through coupling with the small band gap Fe_2WO_6 photocatalyst. The effect of process parameters has also been described, especially the photocatalyst loading and initial solution pH as they were reported to significantly affect the photocatalytic activities. According to the existing literature reports, there were no report on the construction of $Fe_2WO_6/SrTiO_3$ photocatalyst. Therefore, for the first time, the $Fe_2WO_6/SrTiO_3$ composite will be synthesized and evaluated the photoactivity in dyestuff degradation and *E. coli* and *B. cereus* inactivation.

CHAPTER 3

RESEARCH METHODOLOGY

The research methodology and experimental apparatus were discussed in this chapter. An outline of this research was given by a flowchart as shown in Figure 3.1.

3.1 Chemicals and Materials

All the chemicals and experimental materials used in this research were under analytical grade with no further purification was performed before used. In this study, deionized water was utilized for the preparation of chemicals while ethanol was used as dispersing agent for the synthesis of composite materials. All chemicals are listed in Table 3.1.
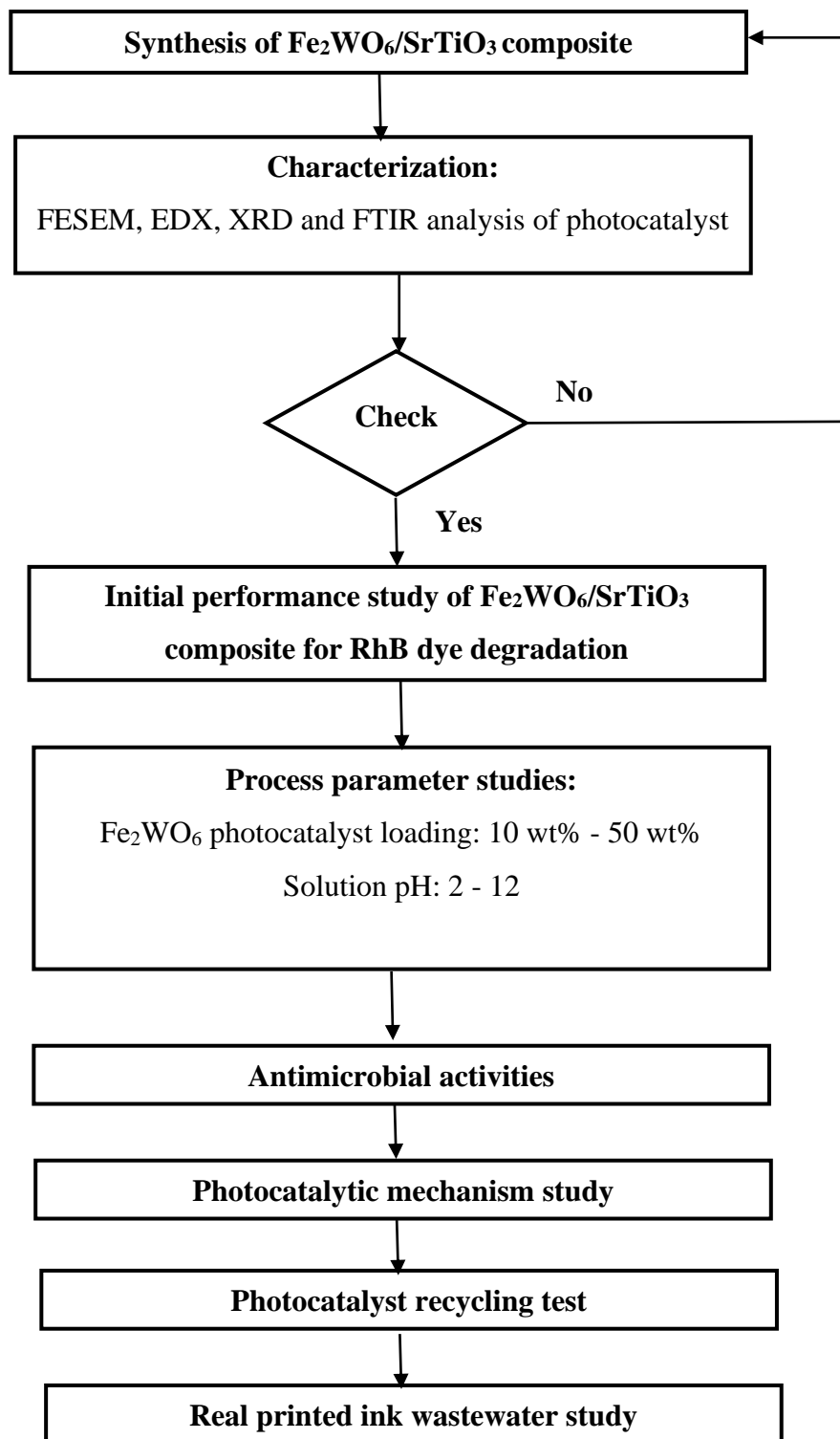
Figure 3.1: Flowchart of Current Research.

Table 3.1: Lists of Chemicals and Materials Utilized

Chemicals	Purity (%)	Supplier	Purpose of use
Strontium nitrate $(Sr(NO_3)_2)$	98	Sigma aldrich	To synthesis $SrTiO_3$ photocatalyst.
Titanium butoxide $(Ti(OBu)_4)$	97	HmbG Chemicals	To synthesis $SrTiO_3$ photocatalyst.
Iron (III) nitrate nonahydrate $(Fe(NO_3)_3 \cdot 9H_2O)$	>97	SYSTERM	To synthesis Fe_2WO_6 photocatalyst.
Sodium tungstate (Na_2WO_4)	99	Acros Organics	To synthesis Fe_2WO_6 photocatalyst.
Sodium Hydroxide (NaOH)	99	Gene Chemicals	To adjust solution pH.
Hydrochloric acid (HCl)	37	Merck	To adjust solution pH.
Ammonia solution (NH_4OH)	25	R & M Chemical	To adjust solution pH.
Ethanolamine (EA)	99.5	Emusure	To dissolve $Ti(OBu)_4$.
Ultrapure water		NEW HUMAN UP	To dissolve chemicals.
Ethanol (C_2H_5OH)	95	Medigene	To wash $SrTiO_3$ photocatalyst.
Sodium chloride (NaCl)	99.5	Gene Chemicals	To dilute culture solution.
Sodium sulphate (Na_2SO_4)	0.5M	R & M Chemical	To use as electrolyte for photoelectrochemical testing.
Silver nitrate $(AgNO_3)$	99.9	Gene Chemicals	To capture electrons.
Ethylenediamine tetraacetate (EDTA)	99	SYSTERM Chemicals	To capture holes.
Benzoquinone (BQ)	98	Acros Organics	To capture superoxide anion radicals.
Isopropanol (IPA)	-	Gene Chemicals	To capture hydroxyl radicals.
Escherichia coli (*E. coli*)	-	Himedia	To culture bacteria.
Bacillus cereus (*B. cereus*)	-	Himedia	To culture bacteria.
Nutrient Agar	-	Himedia	As the culture medium.
Nutrient Broth		Himedia	To provide nutrient.
Rhodamine B (RhB)	≥ 90	Merck	Acts as the synthetic dye wastewater.
Printed ink wastewater	-	Hasrat Meranti Sdn Bhd, Bercham, Ipoh	To use as real dyestuff wastewater effluent for photocatalytic degradation study.

3.2 Apparatus and Equipment

3.2.1 Photocatalysis Experimental Apparatus

The photodegradation of rhodamine B dye under visible LED light condition was carried out in the fume hood. The experimental setup was in this study was depicted in Figure 3.2. The experimental setup included a magnetic stirrer plate with a beaker, one unit of a 150 W visible LED light bulb and a flow meter. The LED bulb with warm white color (3000 K) and SMD-5730 emitter type was brand AARON. The magnetic stirring rate was kept at 300 rpm and the air flow rate was maintained at 2 min L^{-1}.
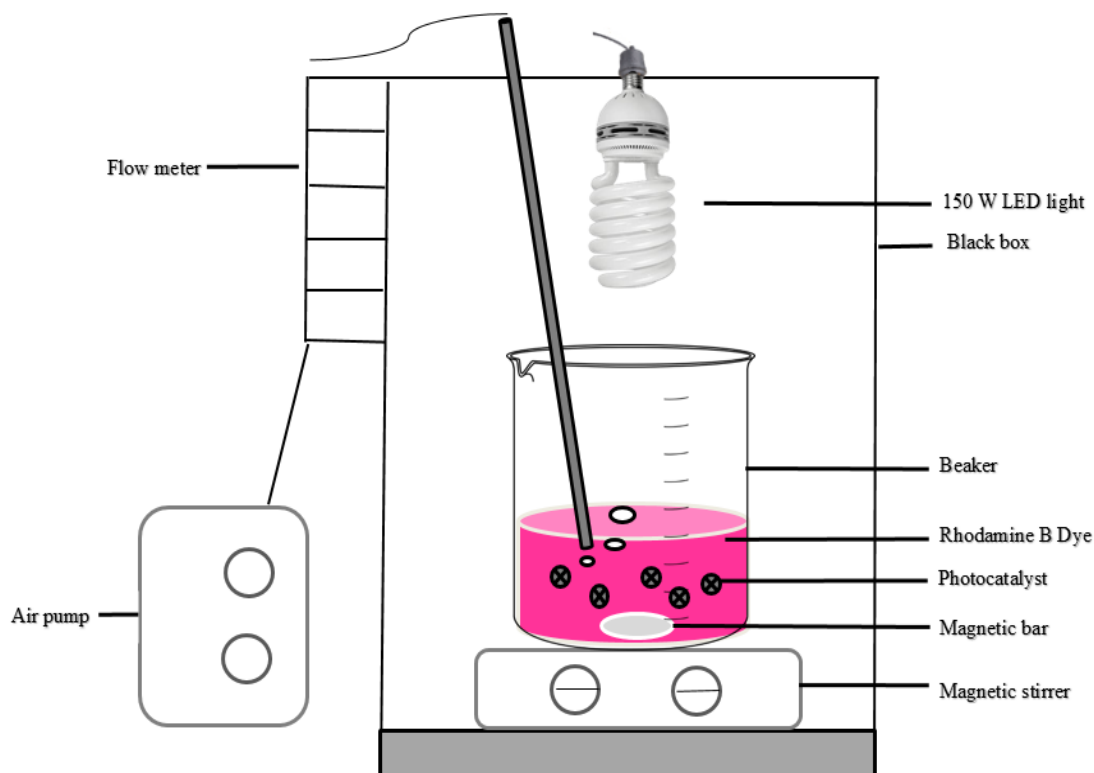
Figure 3.2: Schematic Diagram of Photocatalytic Degradation System.

3.2.2 UV-Vis Spectrophotometer

The RhB dye concentrations before and after the photodegradation were tested by a JASCO V-730 UV–vis spectrophotometer at the specific light wavelength (λ) of 553 nm. The sample solution was transferred into a quartz cuvette with specific light wavelength (λ) was set in the UV-Vis spectrophotometer for light absorption. The sample solution was poured into a quartz cuvette with specific light wavelength (λ) was set in the UV-Vis spectrophotometer for light absorption. When light passes through the sample, some light was absorbed by the molecules and some passes through directly. As a result, less light will pass through the sample, and the absorption degree of the molecules will be recorded by the spectrophotometer. The UV-Vis spectrophotometer can be then used to examine the pollutants concentration in solution by using the molar absorptivity or plotting a calibration curve (Yi et al., 2018). The Beer-Lambert Law presents the relationship between the absorbance and the concentration of pollutants as shown in Eq. (3.1) (Oh and Kim, 2021).

$$A = \varepsilon lc \tag{3.1}$$

Where A denotes the measure of absorbance at specific λ, ε was the coefficient of molar absorptivity in L mol^{-1} cm^{-1}, l was the length of path that light passed through in cm and c was the concentration of solution in mg L^{-1}.

3.3 Analytical procedures

3.3.1 Chemical Oxygen Demand (COD) Analysis

The mineralization efficiency of the real printed ink wastewater was evaluated using COD analysis to optimize the composite photocatalyst. The procedures in examining the COD were on the basis of the *HACH* Reactor Digestion Method 8000 in *HACH* Water Analysis Handbook (*HACH*, 2019). Typically, 2 mL of sample solution was

taken out and injected into COD High Range (HR) Digestion Reagent vials. The COD vials were then digested in a Hanna HI-839800 reactor at 150°C for 120 min. Then the vials were allowed to cool at ambient temperature prior to the determination of COD value. The COD value was determined with a *HACH* DR890 colorimeter which expressed in mg L^{-1}. These steps were duplicated three times to obtain average results for accuracy data.

3.3.2 pH Analysis

The pH was a quality parameter to determine the acidity or alkalinity of sample solution. At lower or higher pH value, most of the aquatic creatures could not survive (Palani, et al., 2020). The *Hanna HI-2211* pH meter was used to determine the solution pH. To analyze the solution pH, the probe of pH meter was cleaned by deionized water before and after every value taken, then it was put into the sample solution to read the value. The pH value was duplicated three times to obtain an average result for accuracy data.

3.4 Synthesis of Photocatalyst

In this study, the preparation of Fe_2WO_6, $SrTiO_3$ and $Fe_2WO_6/SrTiO_3$ composite were systematically synthesized in the subsequent sections.

3.4.1 Synthesis of SrTiO₃ Photocatalyst

The $SrTiO_3$ photocatalyst was prepared by a simple solvothermal method following literature procedures with modifications (Han et al., 2019; Qu et al., 2020). 10 mmol $Ti(OBu)_4$ was dissolved with 60 mL $(CH_3)_2CHOH$. 10 mL aqueous solution

containing 10 mmol $Sr(NO_3)_2$ was mixed with the above mixed solution, and then a certain amount of NaOH was added under magnetic stirring for 60 min. The mixture was transferred into a Teflon-lined stainless-steel autoclave and kept at 180 °C for 24 h. After natural cooling, the white precipitate was obtained and washed using deionized water and alcohol for three times and dried at 60 °C overnight. A flowchart of the synthesis process was illustrated in Figure 3.3.
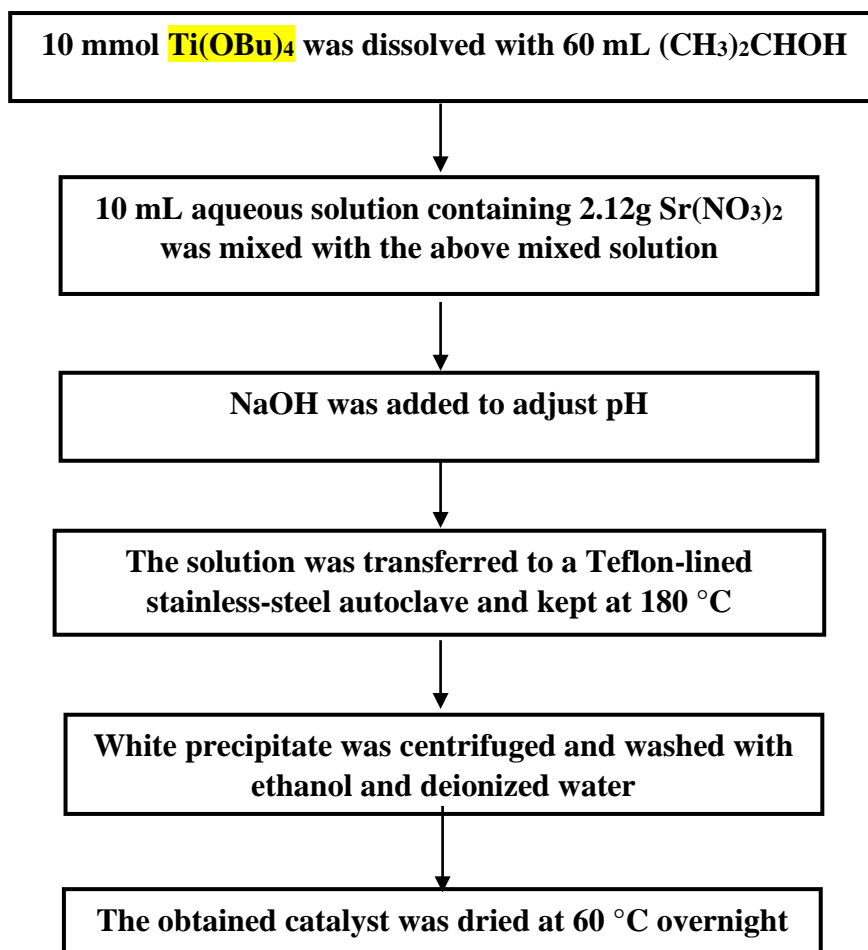
Figure 3.3: Flowchart of Preparation of SrTiO₃ photocatalyst.

3.4.2 Preparation of Fe₂WO₆/SrTiO₃ Composite

The Fe_2WO_6/$SrTiO_3$ composites were prepared via a simple hydrothermal process. In the process, 5 mmol $Fe(NO_3)_3 \cdot 9H_2O$ was mixed with deionized water under vigorous magnetic stirring. 2.5 mmol Na_2WO_4 was solute in deionized water and added dropwise to mixed solution, and then 95 mL ammonia water was dropped under magnetic stirring. 1 g $SrTiO_3$ was added under continuous stirring. Finally, the suspension was transferred to a Teflon stainless steel autoclave and heated at 200 °C for 18 h. The 50 wt% Fe_2WO_6/$SrTiO_3$ powder was obtained after washed using deionized water and alcohol. Meanwhile, other loadings Fe_2WO_6/$SrTiO_3$ composite including pure Fe_2WO_6 were obtained via the above process. The preparation process was depicted in Figure 3.4.
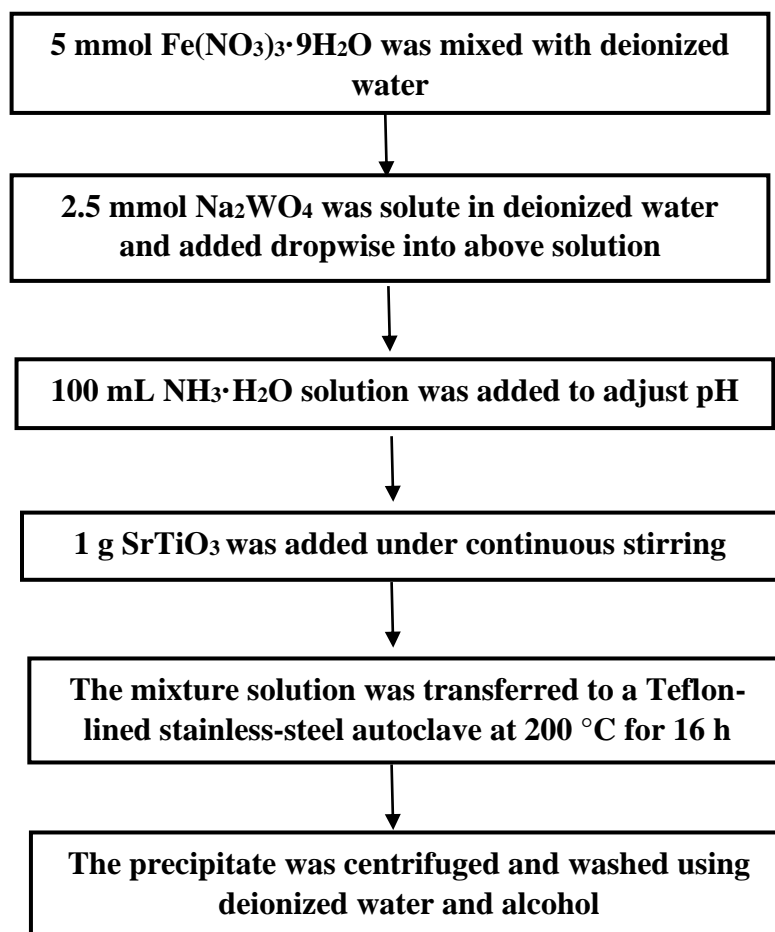
Figure 3.4: Flowchart of Synthesis Fe₂WO₆/SrTiO₃ Composite.

3.5 Characterization of Fe$_2$WO$_6$/SrTiO$_3$ Composite

3.5.1 Morphology and Composition Analysis

The morphology and elemental composition of the as-synthesized photocatalysts was determined through the Field-Emission Scanning Electronic Microscopy coupled with Energy Disperse X-Ray (FESEM-EDX). *Jeol JSM-6701F* FESEM-EDX instrument was used to analyze samples. Prior to the analysis, the samples were tap on aluminium tube with the carbon tape. The sample photocatalyst was coated on fine layer of platinum through *Jeol JSM-1600* auto fine coater and then vacuumed for 5 minutes for degassing. This morphological and elemental analysis were carried out in at the Faculty of Science at UTAR.

3.5.2 Crystallization Analysis

The crystalline properties of the as-synthesized photocatalysts can be tested through the X-ray Diffraction (XRD) analysis. The patterns were examined using a *Philips PW1820* diffractometer with Cu Kα incident radiation ($\lambda = 1.5406$ Å) within a 2θ ranging from 10° to 80°. This crystallization phase analysis was tested at the Faculty of Science at UTAR.

3.5.3 Surface Functional Group Analysis

The surface functional groups of as-synthesized samples were measured by the fourier transform infrared spectroscopy (FTIR) analysis. And the FTIR spectra were obtained with a Perkin Elmer *RX-1* fourier-transform infrared spectrometer with scanning range of 400 cm^{-1} to 4000 cm^{-1}. This surface functional group analysis was conducted at the Faculty of Science at UTAR.

3.5.4 UV-vis Diffuse Reflectance Spectroscopy

The optical properties of the as-synthesized photocatalysts were investigated using the UV-Vis diffuse reflectance spectroscopy (UV-Vis DRS). The UV-Vis DRS spectra were evaluated via a *JASCO V-730* UV-vis spectrophotometer with scanning range of 200 nm to 800 nm. This analysis was conducted at the Faculty of Science at UTAR.

3.5.5 Photoelectrochemical Analysis

The photoelectrochemical properties were carried out on an electrochemical potentiostat (Gamry Interface 1000) with a standard three-electrode cell. In this system, fluorine doped tin oxide (FTO) glass coated with photocatalysts, platinum and silver chloride served as the working electrode, counter electrode and reference electrode, respectively. 0.5 M sodium sulfate aqueous solution was selected as the electrolyte solution and 150 W LED lamp as the visible light source. In detail, 0.05 g synthesized photocatalyst was mixed with 5 mL ethanol, and then the mixtures were sonicated for 30 min in order to obtain a homogeneous suspension. The working electrodes were made by suspension onto FTO glass and following drying overnight. The electrochemical impedance spectroscopy (EIS) Nyquist plot was measured in the range of 0.1-10 kHz. The linear sweep voltammetry (LSV) was carried out at a scanning rate of 50 mV s^{-1}. The transient photocurrent response (TPR) was recorded with the light on and off every 30 s. The Mott-Schottky (M-S) plots were measured over the frequency of 1 kHz.

3.6 Photocatalytic Degradation of Dyestuff

The photodegradation of RhB dye was conducted for pure $SrTiO_3$, pure Fe_2WO_6, and $Fe_2WO_6/SrTiO_3$ composites. Initially, 35 mg photocatalyst power and 70 mL of 5 mg L^{-1} solution of RhB dye was transferred into a 100 mL quartz tube. The HCl and NaOH

solutions were used to adjust pH of these solutions. The mixtures were stirred under dark condition for 0.5 h prior to exposure to light in order to realize adsorption-desorption equilibrium. Then, a 150W LED lamp was switched on and the degradation of dyestuff was determined for a total 2 hours reaction time. 2 mL suspension was withdrawn at a given interval time. Afterwards, in order to remove the particles, the above suspension was centrifuged at 4000 rpm for 15 min. The residual RhB concentration was determined by a *JASCO V-730* UV-vis spectrophotometer at 553 nm. In order to eliminate errors, the similar photodegradation experiments were repeated three times.

3.7 Mineralization Study

The mineralization efficiency of actual wastewater was conducted through a COD analysis. After the visible LED lamp was switched on for the photocatalytic activities by the composites, the sample solution was extracted every 30 min. The solution extracted was centrifuged to remove the particles. Then, the mineralization efficiency can be calculated using Eq. (3.2).

$$Mineralization\ Efficiency\ (\%) = [(COD_i - COD_f)/COD_i] \times 100\% \qquad (3.2)$$

where COD_i was the initial COD value (mg L^{-1}) at $t = 0$ and $COD_{f\ was}$ the COD value (mg L^{-1}) at given time, t expressed in min.

3.8 Parameter Studies

3.8.1 Photocatalyst Loading

One of the important process parameters that directly affects the photocatalytic activity was the photocatalyst loading. The increase in the photocatalyst loading will

increase the photodegradation efficiency of pollutants (Mahendran et al., 2021; Vigneshwaran, et al., 2021). The catalyst loading of Fe_2WO_6 in the $Fe_2WO_6/SrTiO_3$ composite was studies at the range from 10 wt% to 50 wt%. The selection of the loading was based on the literatures conducted by W. Chen et al. (2019), G. Zhao et al. (2021) and Cao et al. (2021). The experiments will be performed at an initial RhB concentration of 5 mg L^{-1} under natural pH 5.

3.8.2 Solution pH

The solution pH has great influence on the photocatalytic degradation of different pollutants. The effect of solution pH on the photodegradation of dyestuff was measured with ranging from pH 2 to pH 12. 2 M NaOH and HCl solution were used to change the initial solution pH of the dye. The pH ranges selection was based on the literature carried out by M. Ahmad et al. (2021), El-Shamy et al. (2020) and Shetty (2020). The experiments were conducted at initial RhB concentration of 5 mg L^{-1} with optimized $Fe_2WO_6/SrTiO_3$ catalyst loading.

3.9 Antimicrobial Activity

Antimicrobial activities for prepared photocatalysts were confirmed by the disinfection of gram-negative (*E. coli*) and gram-positive bacteria (*B. cereus*). These two bacteria were selected because they are common type bacteria found in foods, natural water bodies and wastewater (Tuipulotu et al., 2021; Denamur et al., 2021). The photocatalytic antibacterial activities were carried out by the agar well diffusion method to observe zone of inhibition (ZOI) (Chai et al., 2019; J. Ma et al., 2022a). In a typical procedure, all the glassware used throughout in this procedure were sterilized in an autoclave at 120 °C for 20 min. 14.0 g nutrient agar was suspended in 500 ml DI water, and then the medium was heated to dissolve completely. The mixture was sterilized by

autoclaving at 15 lbs pressure (120 ℃) for 20 min. Afterwards, the above mixture was cooled to 45-50 ℃ and poured into plates. Moreover, 6.5 g nutrient broth was suspended in 500 ml DI water. The medium was stirred to dissolve completely and sterilized at 120 ℃ for 20 min. Then, culture the bacteria in nutrient broth to obtain the bacterial solution at 37 ℃ for 16 h. Then diluted the bacterial solution to yield a cell count of 10^7 CFU/mL using saline water. Hence, took 0.5 mL of the above saline water and spread it on agar plates, and then a filter paper filled with prepared samples was fixed on the plate. After hatched at 37℃ for 24 h, the ZOI was determined and recorded.

3.10 The Role of Reactive Oxygen Species (ROS) for Degradation of Dyestuff

Under the visible light irradiation, the photocatalysis process can generate various ROSs, including electrons (e^-), holes (h^+), superoxide radicals ($\bullet O_2^-$) and hydroxyl radicals ($\bullet OH$). The scavenger tests were performed for investigating the radical species. 5 mM of $AgNO_3$, EDTA, BQ, or IPA was added to the photocatalytic experiments for detecting reactive radicals including e^-, h^+, $\bullet O_2^-$ and $\bullet OH$, respectively (F. Zhao et al., 2020; Kuila et al., 2021; Y. Zhang et al., 2022b; Munawar et al., 2020).

3.11 Recycling Test

To evaluate the stability of $Fe_2WO_6/SrTiO_3$ composite after photocatalytic reaction, the recycling test was conducted. In general, after one cycle of photocatalytic process, the composite was collected and used for another set of experiments under the same conditions (X. Zhang et al., 2021a; X. Wu et al., 2022). In the typical procedure, the used composite was collected by centrifugation. The collected sample was dried in a vacuum oven at 60 ℃ overnight. The obtained sample was then run for several times to test the durability of the photocatalyst.

3.12 Real Printed Ink Wastewater Effluent Study

The photocatalytic degradation of real printed ink wastewater was conducted using the optimized composite and process parameters. The real printed ink wastewater was collected at Hasrat Meranti Sdn Bhd, Bercham, Ipoh on April 2022. After collected from the paper printing industry, the wastewater was first filtered with 38 μm stainless steel mesh sieve to remove large particles in wastewater. The wastewater was stored in a plastic drum at 5 °C in a refrigerator. Afterwards, a 150W LED lamp was switched on and the degradation of real wastewater was determined for a total 4 hours reaction time. 2 mL suspension was withdrawn at a given interval time. Afterwards, in order to remove the particles, the above suspension was centrifuged at 4000 rpm for 15 min. The efficiency of mineralization of the real wastewater was determined through the COD analysis.

3.13 Electrical Energy per Order (E_{EO}) Study

The major cost of photocatalytic process was primarily related with E_{EO} and it can be defined as the number of kWhr of electrical energy required to reduce the concentration of a pollutant by the pseudo first order rate constant in 1 m³ of wastewater (Asaithambi et al., 2017). The E_{EO} can be estamited using the Eq. (3.3).

$$Electrical\ energy\ per\ order\ (\%) = (38.4 \times P_{el}/V \times k) \times 100\% \qquad (3.3)$$

Where $P_{el\ was}$ the rated power (kW), V denotes the volume of effluent taken (L), k was the pseudo first order rate constant for the decay of the effluent concentration (min^{-1}).

CHAPTER 4

RESULTS AND DISCUSSION

This chapter explained the experimental findings of the current study. The first part of the chapter demonstrated the characterization results on the synthesized $Fe_2WO_6/SrTiO_3$ composite utilized in the photocatalytic degradation of dyestuff. In the second part of this chapter, the preliminary performance of the developed $Fe_2WO_6/SrTiO_3$ composite in photocatalytic degradation of the synthetic dyestuff wastewater was depicted. In the next part of this chapter, several process parameters including the Fe_2WO_6 catalyst loading and the solution pH were conducted to evaluate the photocatalytic degradation performance. Subsequently, the antibacterial activities using the optimized $Fe_2WO_6/SrTiO_3$ photocatalyst towards *Escherichia coli* (*E. coli*) and *Bacillus cereus* (*B. cereus*) via a agar well diffusion method. In the fifth part of this chapter, the radical scavenging test was conducted to determine the major reactive oxygen species (ROS) responsive in degradation of dyestuff wastewater. This was followed by the reusability study of the optimized $Fe_2WO_6/SrTiO_3$ photocatalyst. What's more, the photocatalytic degradation of real printed ink wastewater utilizing the best composite at the optimum condition was also studied. Lastly, the electrical energy per order (E_{EO}) in the photodegradation process was also calculated.

4.1 Characterization of the Synthesized Photocatalysts

Characterization of the synthesized photocatalysts, including pure Fe_2WO_6, pure $SrTiO_3$ and $Fe_2WO_6/SrTiO_3$ composites were conducted. The characterization techniques including the surface morphology, elemental composition, crystallization phase, band gap, surface functional group and photoelectrochemical test were used to evaluate the physical, chemical and photoelectrochemical properties of the photocatalysts. The morphology of the synthesized photocatalysts was investigated through field emission scanning electron microscope (FESEM) images while the elemental composition was examined by the energy dispersive X-ray (EDX) technique. The X-ray diffraction (XRD) analysis was conducted to determine the crystallization phase while Fourier-transform infrared spectroscopy (FTIR) analysis was used to examine the surface functional group of the synthesized photocatalyst. Next, the optical property of the photocatalysts was identified using the UV-vis diffuse reflectance spectroscopy (UV-vis DRS) technique. Lastly, the photoelectrochemical tests, such as the transient photocurrent response (TPR), electrochemical impedance spectroscopy (EIS), and Mott-Schottky (M-S) were conducted to study the electronic properties of the catalysts.

4.1.1 Morphological Analysis

The morphology of prepared samples including pure Fe_2WO_6, pure $SrTiO_3$ and $Fe_2WO_6/SrTiO_3$ composite were examined through FESEM images. Figures 1a and b portray that pure Fe_2WO_6 was mainly composed of tiny nanoparticles. The measured particle diameters of Fe_2WO_6 were varied from 50 nm to 70 nm. In addition, some Fe_2WO_6 nanoparticles gathered together. It could be observed that the image of pure $SrTiO_3$ revealed its morphology existed as a cube-like morphologies (Figures 1c and d). Pure $SrTiO_3$ has been found to have average particle diameters of about 320 nm.

Based on the FESEM images of the $Fe_2WO_6/SrTiO_3$ composite, the composite surface turned out to be rough which was owing to Fe_2WO_6 being added on $SrTiO_3$

(Figures 1e and f). In addition, the diameter of the $Fe_2WO_6/SrTiO_3$ composite was larger than pure $SrTiO_3$, suggesting that cube-like structures of $SrTiO_3$ particles were surrounded
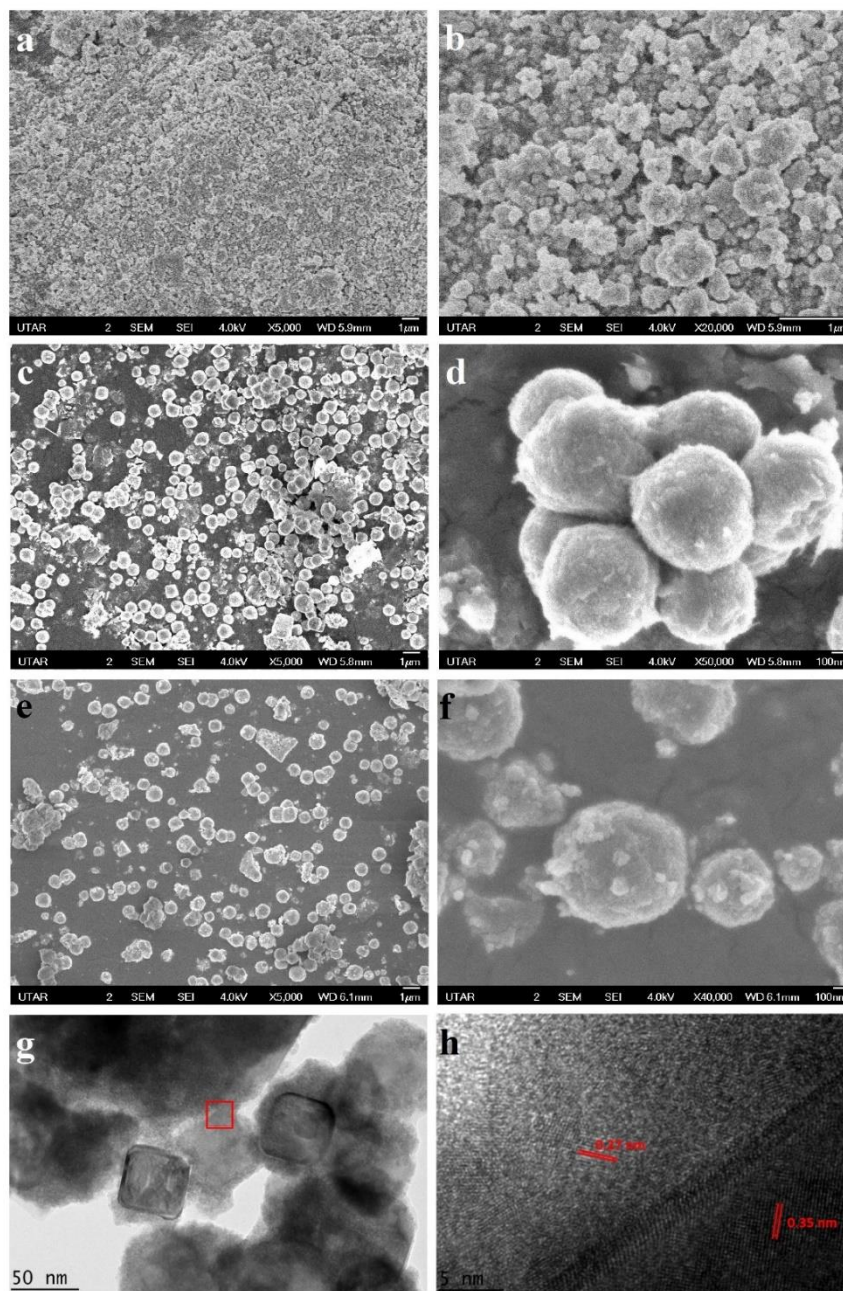
Figure 4.1: FESEM Images of (a-b) pure Fe₂WO₆ and (c-d) pure SrTiO₃. (e-f) FESEM Images, (g) TEM Image and (h) HRTEM Image of Fe₂WO₆/SrTiO₃ Composite.

with Fe_2WO_6 nanoparticles and the added Fe_2WO_6 was tiny particles. Besides, the morphological structures of composite were further examined using TEM images. It was obvious that Fe_2WO_6 particles seemed to be uniformly attached to $SrTiO_3$ particles (Figure. 1g). In Figure 4.1(h), the lattice spacings of 0.27 and 0.35 nm were observed, which can be associated with the $SrTiO_3$ (110) and Fe_2WO_6 (130) planes, respectively. The lattice spacings of $SrTiO_3$ and Fe_2WO_6 in current study were in consistent with the literatures reported by Rawal et al. (2014), Hassanpour et al. (2020) and Yue et al. (2018). Hence, theintimate interface between Fe_2WO_6 and $SrTiO_3$ confirmed the formation of heterojunctionin the composite, which was useful for charge transfer and separation of photogeneratedcharge carriers in photocatalysis process (Figure 4.1(h)). The results demonstrated theFe_2WO_6/$SrTiO_3$ composite was prepared successfully by the hydrothermal method.

4.1.2 Elemental Composition Analysis

The analysis of elemental composition of the prepared photocatalyst was conducted through the energy disperse X-ray (EDX) technique. The results obtained for each catalyst are displayed in Figure 4.2. The EDX spectrum of the Fe_2WO_6/$SrTiO_3$ composite was composed of Fe, W, Sr, Ti and O elements, indicating that the Fe_2WO_6 had successfully incorporated to the $SrTiO_3$ photocatalyst and resulted in the Fe_2WO_6/$SrTiO_3$ composite materials. Moreover, the EDX mapping of the synthesized Fe_2WO_6/$SrTiO_3$ composite in Figure 4.3 showed that anticipated elements evenly dispersed in the composite. This result together with the EDX spectrum (Figure 4.2) clearly demonstrated that the Fe_2WO_6 was successful deposited onto the surface of pure $SrTiO_3$.
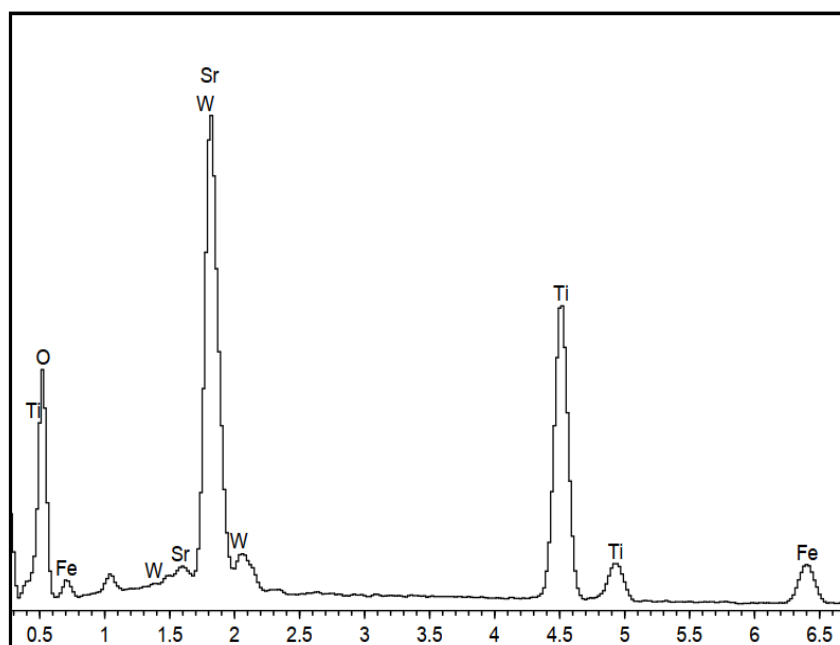
Figure 4.2: EDX Spectra of Fe$_2$WO$_6$/SrTiO$_3$ Composite.
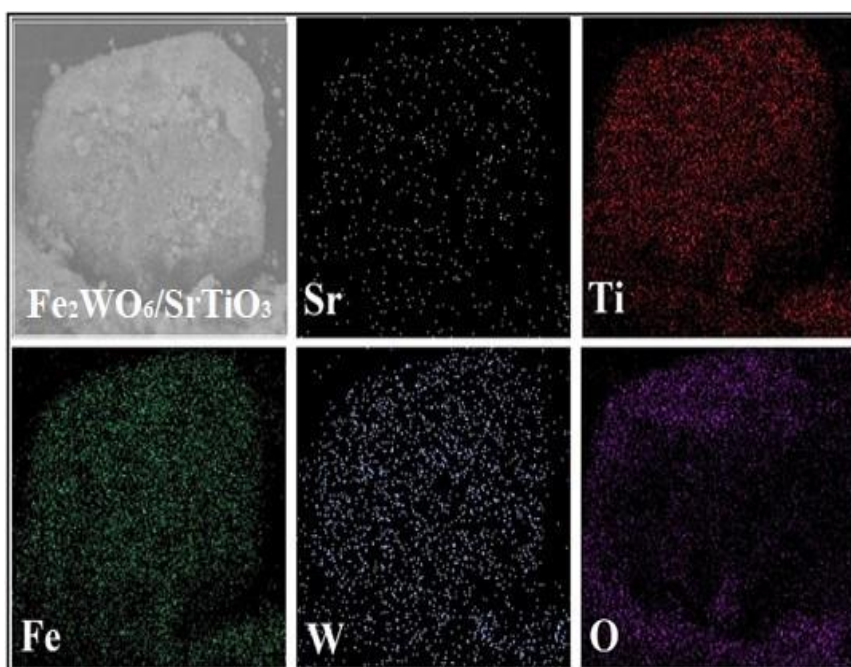
Figure 4.3: EDX Mapping of Fe$_2$WO$_6$/SrTiO$_3$ Composite.

4.1.3 Crystallization Phase Analysis

The crystallization phases of the prepared photocatalysts were examined through the XRD analyses and the patterns of each photocatalyst are depicted in Figure 4.4. As shown in figure, the pure $SrTiO_3$ photocatalyst exhibited the diffraction peaks existed at $2\theta = 32.37°, 39.93°, 46.45°, 57.75°, 67.77°$ and $77.11°$, which can be corresponded to the (110), (111), (200), (211), (220) and (310) crystal planes, respectively. This result demonstrated that the pure $SrTiO_3$ existed as a cubic perovskite phase and consistent with the standard card JCPDS No. 35-0734 (Y. Zhang et al., 2022b; X. Yu et al., 2020; Qiao et al., 2019; H. Shen et al., 2017). As for pure Fe_2WO_6, the characteristic peaks appeared at $2\theta = 25.11°, 31.00°, 31.96°, 41.92°, 44.64°, 52.96°$ and $57.23°$, which can be associated with (110), (111), (020), (102), (112), (220) and (221) planes, respectively. The results reflected that the pure Fe_2WO_6 existed as an orthorhombic phase and matched with the standard JCPDS No. 70-0495 (Caubergh et al., 2021; Espinosa-Angeles et al., 2021; Hassanpour et al., 2020).
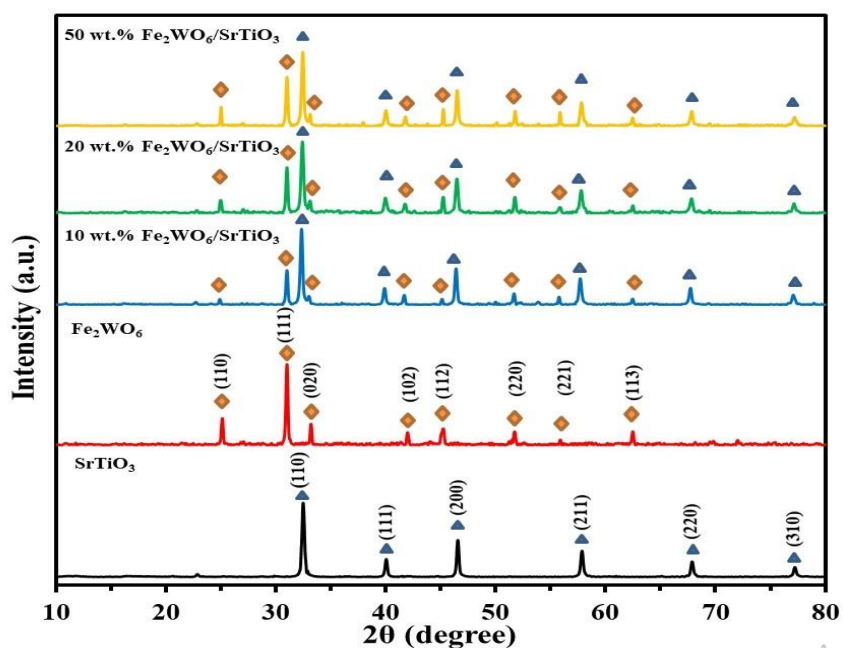
Figure 4.4: XRD Patterns of Various Synthesized Photocatalysts.

Meanwhile, the XRD patterns for the $Fe_2WO_6/SrTiO_3$ composites materials depicted the characteristic peaks for pure Fe_2WO_6 and pure $SrTiO_3$, indicating $Fe_2WO_6/SrTiO_3$ composites were constituted by pure Fe_2WO_6 and pure $SrTiO_3$. In addition, the characteristic diffraction peaks of the prepared composites were analogous to those of pure $SrTiO_3$ and pure Fe_2WO_6, suggesting that the crystalline phase of Fe_2WO_6 and $SrTiO_3$was preserved in the composites (Zhao, et al., 2020). Moreover, it can be observed that the intensity of Fe_2WO_6 peaks were increased as weight percent of Fe_2WO_6 in $Fe_2WO_6/SrTiO_3$ composites rose. The XRD patterns revealed that the $Fe_2WO_6/SrTiO_3$ composites were synthesized favorably. This XRD results were consistent with the FESEM and EDX outcomes.

4.1.4 Surface Functional Group Analysis

FTIR spectroscopy was a useful technique to determine surface functional groups of the obtained photocatalysts. The FTIR spectra of obtained photocatalysts are shown in Figure 4.5. For pure $SrTiO_3$, the typical peak of 535 cm^{-1} was attributed to the vibration of Ti-O bond, while Sr-O bond was anticipated by the characteristic peak found at 763 cm^{-1} (Qu et al., 2020; Y. Zhang et al., 2022b). In addition, the absorption peak at 1460 cm^{-1} correspond to stretching vibration of Ti-O-Ti of $SrTiO_3$ (X. Wang et al., 2020c; Guo et al., 2018). When increasing the Fe_2WO_6, the corresponding reduction of $SrTiO_3$ in the composite weakens the typical peak at 1460 cm^{-1}. The spectra of pure Fe_2WO_6 demonstrated the band at 453 cm^{-1} corresponds to bending vibration of O-Fe-O bond (Hassanpour et al., 2020). The peak at 939 cm^{-1} was ascribed to the vibration of W-O bond belonging to Fe_2WO_6 (Kokilavani et al., 2021). Furthermore, the increasing the Fe_2WO_6 weight percent in the composite has intensified the typical peaks at 453 cm^{-1} and 939 cm^{-1}. The characteristic peak at 1380 cm^{-1} was related to the symmetric vibration of NO_3^- group, which was from the raw material used for the synthesis of as-prepared photocatalyst (X. Wang et al., 2020c; Ashwini et al., 2017). All samples exhibited two typical peaks at 3380 cm^{-1} and 1633 cm^{-1}, which could be ascribed to O-H stretching in crystallization water

and H-O-H bending vibration of adsorbed water, respectively (Z. Xia and Hu, 2019; Janani et al., 2021; J. Wang et al., 2021a). Besides, the O-H peaks intensities of composites were extremely higher than those of pure components, revealing that the composite possessed a more hydroxyl-rich surface after the construction of heterojunction. The hydroxyl groups facilitated the production of hydroxyl radicals, which were responsible for the ameliorated photocatalytic activity.
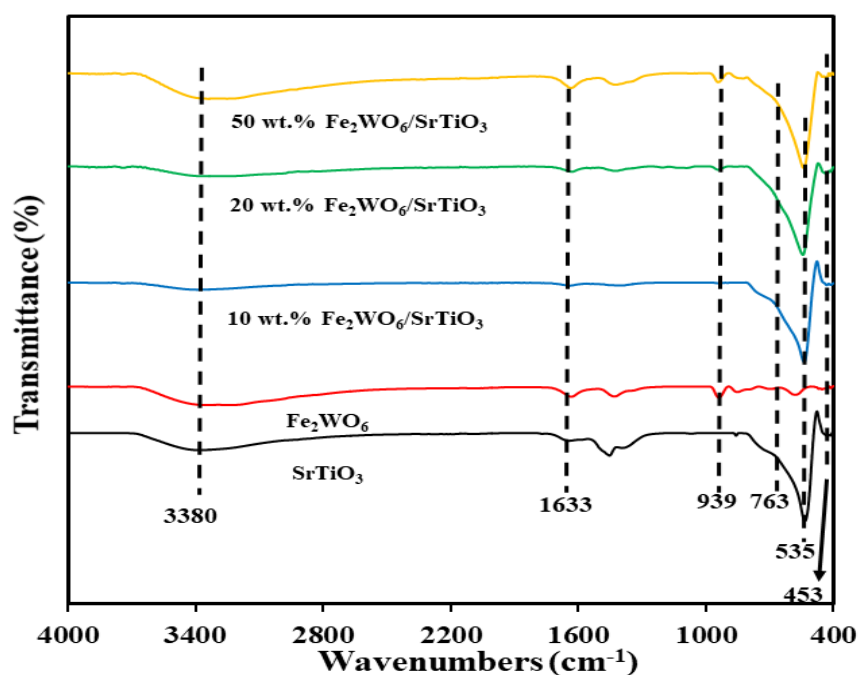
Figure 4.5: FTIR spectra of the Synthesized Photocatalysts.

In addition, the function group of fresh and recovered composite also was checked to access the stability property. Figure 4.6 demonstrates no changes on the FTIR spectra of recovered $Fe_2WO_6/SrTiO_3$ composite compared to that of fresh composite. The results showed the important functional groups still remained, confirming its stability and recyclability properties. Consistent results were reported in the literature studies (Y. Xu et al., 2022; Nallapureddy et al., 2023). Y. Xu and co-workers (2022) conducted the FTIR analysis to examine the stability of photocatalyst. The FTIR spectra revealed that the functional groups of photocatalyst after five cycles was also kept well. They justified that

the photocatalyst displayed the outstanding stability in the degradation wastewater. Another report by Nallapureddy et al. (2023) also tested the FTIR spectra of photocatalyst before and after reusability for dye degradation.
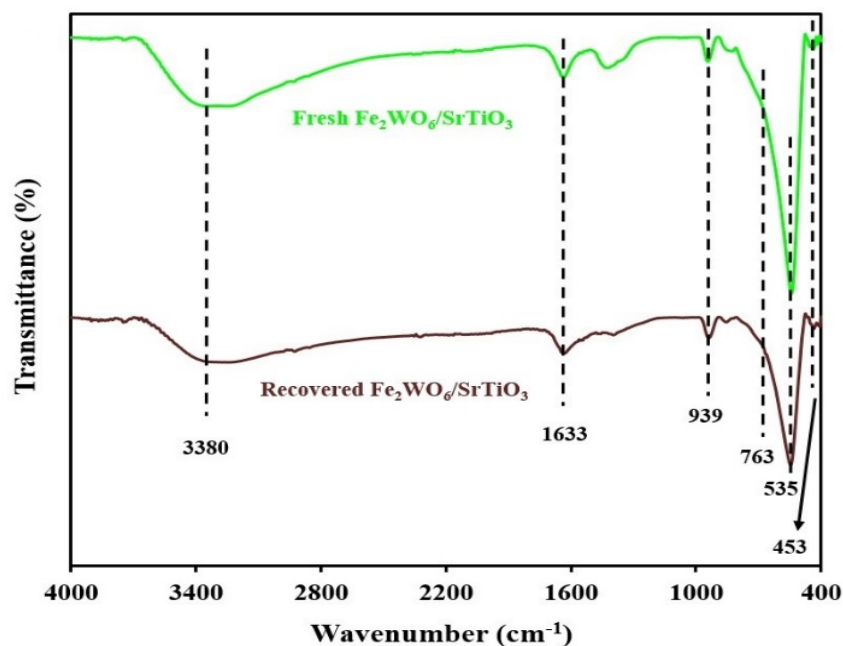
Figure 4.6: FTIR spectra of the Fresh and Reused Photocatalysts.

4.1.5 Band Gap Energy Analysis

The optical properties of the synthesized photocatalysts including pure $SrTiO_3$, pure Fe_2WO_6 and $Fe_2WO_6/SrTiO_3$ composite were determined via the UV-vis Diffuse Reflectance Spectroscopy (DRS) technique. As shown in Figure 4.6, pure Fe_2WO_6 showed an admirable visible light response and pure $SrTiO_3$ can only absorb the light in ultraviolet region. As observed from the figure, the $Fe_2WO_6/SrTiO_3$ composite exhibited red shift as compared to pure $SrTiO_3$. This can be attributed to the interaction between Fe_2WO_6 and $SrTiO_3$ forming the heterojunction structure (Chen, et al., 2021; Kong et al., 2021). Besides, the absorption of visible light increased with the Fe_2WO_6 loadings in

$Fe_2WO_6/SrTiO_3$. Therefore, $Fe_2WO_6/SrTiO_3$ composite was expected to improve light utilization capacity for visible light in the photocatalysis process (Janani et al., 2021).
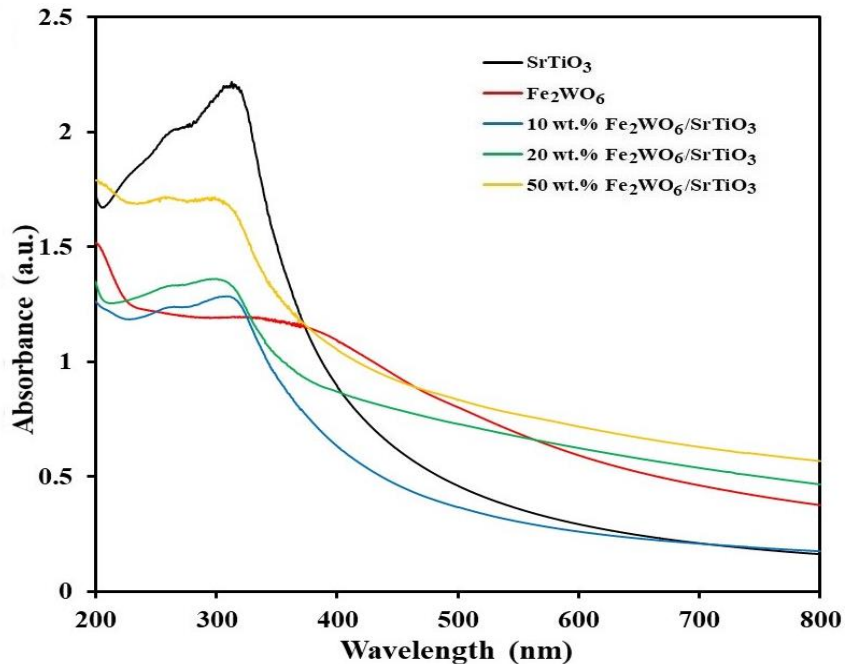
Figure 4.7: UV-vis DRS Spectra of Different Synthesized Photocatalysts.

Furthermore, the band gap energies of the synthesized photocatalysts were estimated by the extrapolating of $(F(R)hv)^2$ versus the photon energy (hv) expressed in eV through the Kubelka-Munk function as depicted in Eq. (4.2) and the photon energy was given by the Eq. (4.3) (Chachvalvutikul et al., 2019; Tan, et al., 2019).

$$F(R) = (1 - R)^2/2R \qquad (4.2)$$

$$E_g = hc / \lambda \qquad (4.3)$$

Where $F(R)$ was the Kubelka-Munk function, R *was* the reflectance (%) of the material, Eg is the optical band gap energy (eV), c *was* light speed in vacuum (m s^{-1}) and λ denotes as the wavelength (nm). The linear expression of the $(F(R)hv)^2$ versus hv for determining

band gap energies for each photocatalyst was plotted and depicted in Figure 4.7. From the figure, a tangent line was drawn to obtain the optical band gap energy. The attained band gap energies for pure Fe_2WO_6, pure $SrTiO_3$ and $Fe_2WO_6/SrTiO_3$ were 2.05 eV, 3.40 eV and 2.80 eV, respectively. The wide band gap of pure $SrTiO_3$ was constricted with the addition of Fe_2WO_6 forming narrower band gap of $Fe_2WO_6/SrTiO_3$ composite materials. Similar findings were reported in other literatures (Ahmadi et al., 2021; Han et al., 2019; Stelo et al., 2020). In their reports, the addition of narrow band gap material to that of wide band could reduce the band gap energy with enhanced visible light absorption for the improved photocatalytic activities.
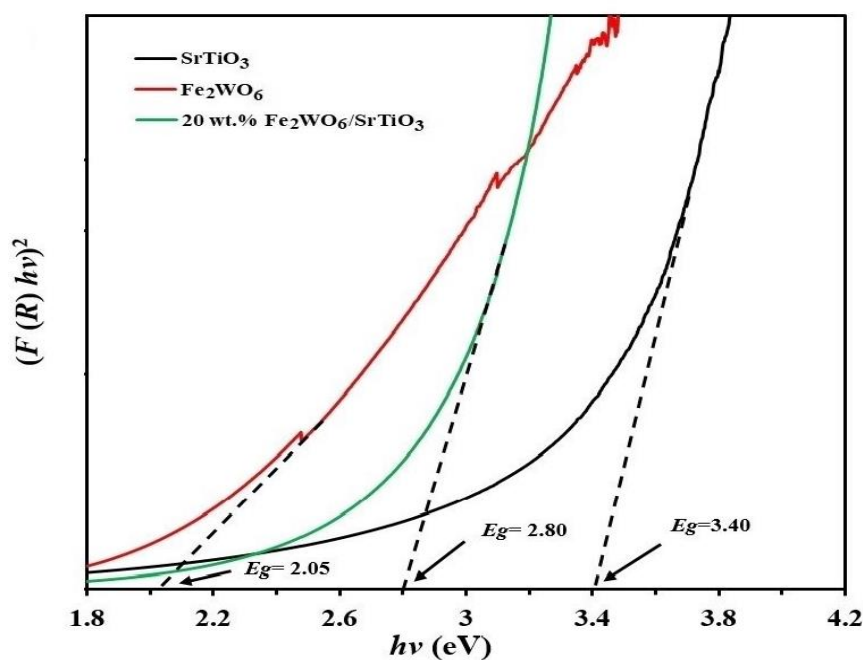
Figure 4.8: Kubelka-Munk Function Plot of $(F(R)hv)^2$ versus hv of pure $SrTiO_3$, pure Fe_2WO_6 and 20 wt.% $Fe_2WO_6/SrTiO_3$ photocatalysts.

4.1.6 Photoelectrochemical Test

4.1.6.1 Transient Photocurrent Response Study

The transient photocurrent response (TPR) measurement was conducted to examine the separation efficiency of carriers of pure Fe_2WO_6, pure $SrTiO_3$ and $Fe_2WO_6/SrTiO_3$ composites. As depicted in Figure 4.8, the photocurrent responses increased in all the samples instantly when the LED light was switched on and dropped immediately when the light was turned off. The photocurrent intensities of $Fe_2WO_6/SrTiO_3$ composites were higher than pure $SrTiO_3$ and pure Fe_2WO_6, revealing that these heterojunction composites displayed faster separation of photogenerated carriers (Sin et al., 2021; Q. Liu et al., 2020; D. Sun et al., 2021). In details, the photocurrent intensities of 20 wt.% $Fe_2WO_6/SrTiO_3$, pure Fe_2WO_6 and pure $SrTiO_3$ were ~0.27 µA cm^{-2}, ~0.09 µA cm^{-2} and ~0.11 µA cm^{-2}, respectively. The 20 wt.% $Fe_2WO_6/SrTiO_3$ showed the best photocurrent intensities, indicating it exhibited the most admirable charge separation. Moreover, the photocurrent intensities reduced slightly at different intermittent light-on and off, which was caused by the sample coated on the FTO glass falling off the electrode (Yuan et al., 2020; Mazzanti et al., 2021). Consistent results were reported in the literature studies (J. Wu et al., 2021; Mazzanti et al., 2021; Yuan et al., 2020).
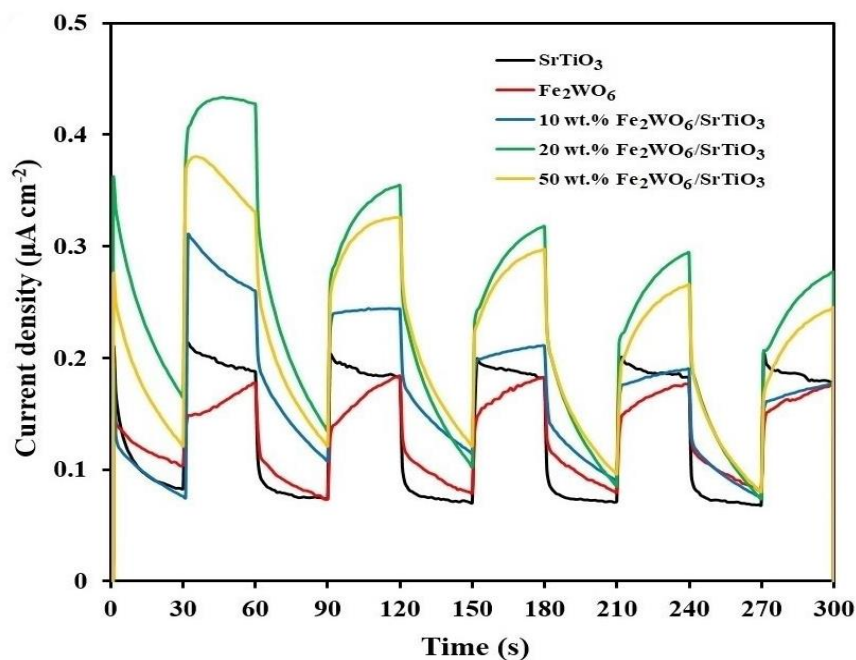
Figure 4.9: TPR Plot of pure Fe₂WO₆, pure SrTiO₃ and Fe₂WO₆/SrTiO₃ composites.

4.1.6.2 Electrochemical Impedance Spectroscopy Study

Furthermore, electrochemical impedance spectra (EIS) was used to investigate the charge carriers transport kinetics of pure Fe_2WO_6, pure $SrTiO_3$ and $Fe_2WO_6/SrTiO_3$ composite. In EIS, the smaller the arc radius is, the higher the separation efficiency was (Qu et al., 2020; H. Sun et al., 2022a; X. Hu et al., 2022). The order of the reduction in semicircle arc size was as followed: $SrTiO_3 > Fe_2WO_6 > 10$ wt.% $Fe_2WO_6/SrTiO_3 > 50$ wt.% $Fe_2WO_6/SrTiO_3 > 20$ wt.% $Fe_2WO_6/SrTiO_3$. As presented in Figure 4.9, the arc radius of $Fe_2WO_6/SrTiO_3$ composites were smaller than pure components, indicating that the $Fe_2WO_6/SrTiO_3$ composites have the faster interfacial electron transfer. Hence, the heterojunction constructed by pure Fe_2WO_6 and pure $SrTiO_3$ was highly beneficial for the improvement of its photoactivity. This EIS result was consistent with the TPR outcomes.
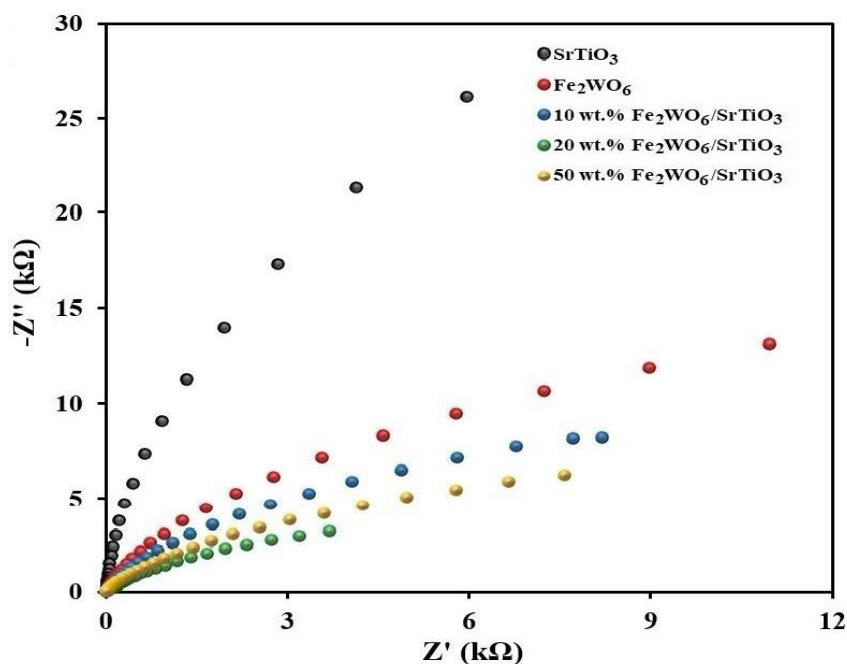
Figure 4.10: EIS Nyquist Plot of the pure Fe₂WO₆, pure SrTiO₃ and Fe₂WO₆/SrTiO₃ composites.

4.1.6.3 Flat band potential Study (Mott-Schottky Plot)

The Mott-Schottky (M-S) plots determined the type and band position of pure Fe_2WO_6 and pure $SrTiO_3$. As illustrated in Figures 4 e and f, both pure Fe_2WO_6 and pure $SrTiO_3$ have the positive slopes, indicating they were *N*-type semiconductors (Fang et al., 2020; W. Zhang et al., 2022a). As shown in Figure 4.10, the flat band potential (E_{fb}) of the pure Fe_2WO_6 and pure $SrTiO_3$ can be determined by drawing a tangent line to the *x*-axes of the graph. The E_{fb} of Fe_2WO_6 were estimated to be +1.05 eV, while the E_{fb} of $SrTiO_3$ was -1.32 eV. As for *N*-type semiconductors, the E_{fb} were more positive by about 0.2 eV than its conduction band potential (E_{CB}) (Y. Zhang et al., 2022b; Fang et al., 2020). Ergo, the E_{CB} of pure Fe_2WO_6 and pure $SrTiO_3$ were calculated to be +0.85 and -1.52 eV, respectively. By integrating the UV-vis DRS and the M-S analyses, the valence band potential (E_{VB}) of these two photocatalysts can be estimated by the formula in Eq. (4.4) (Duan et al., 2021; Feizpoor et al., 2021).
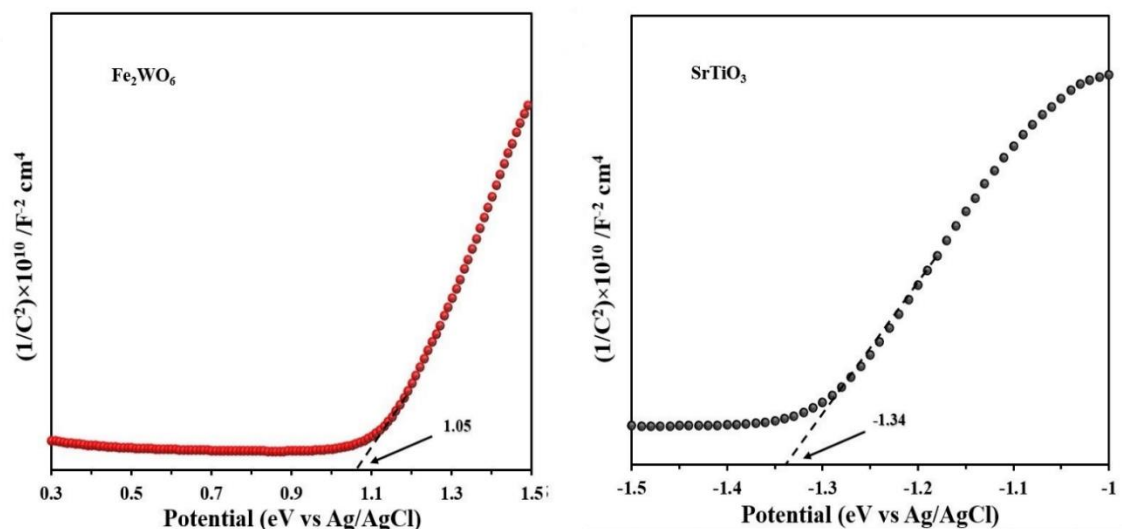
Figure 4.11: Mott-Schottky Plot for (a) Pure Fe₂WO₆ and (b) Pure SrTiO₃.

Therefore, the E_{VB} of each photocatalyst was calculated and illustrated in Table 4.1 (Y. Zhang et al., 2022b; Fang et al., 2020).

Table 4.1: The Band Potential of the Synthesized Photocatalysts.

Photocatalyst	E_g (eV)	E_{CB} (eV)	E_{VB} (eV)
SrTiO₃	3.40	-1.52	1.88
Fe₂WO₆	2.05	0.85	2.90

4.2 Preliminary Study of Photocatalytic Degradation of RhB Dye

In the preliminary study, the removal efficiency of RhB dye was measured under visible LED light. UV-vis spectroscopy was carried out at the wavelength (λ) of 553 nm to test the concentration of RhB. The photocatalytic degradation of RhB without adding of photocatalyst were tested. The results showed little dye was found to be removed under

photolysis condition. In addition, the solution consisting of 5 mg L^{-1} RhB dye solution and 50 mg prepared samples was exposed to 150 W LED light for 120 min. The results were recorded every 30 min, which depicted the gradual reduction in the intensity of typical peak (Figure 4.12). The results showed the RhB dye absorbance decreased with the time, which was attributed the reduction of the RhB chromosphere (Janani et al., 2021; Lops et al., 2019).
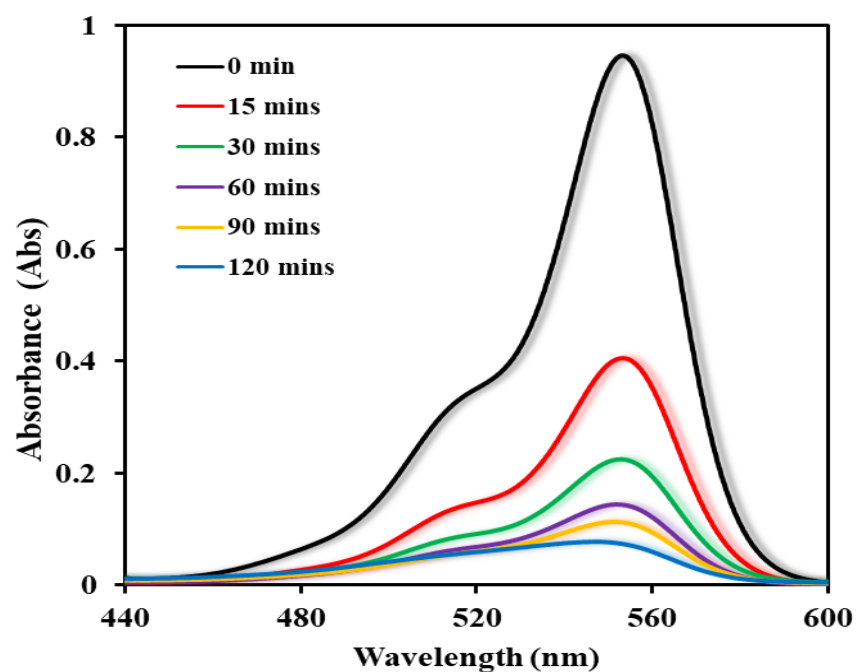
Figure 4.12: UV-vis Absorption Spectrum of RhB at λ = 553 nm Against Time.
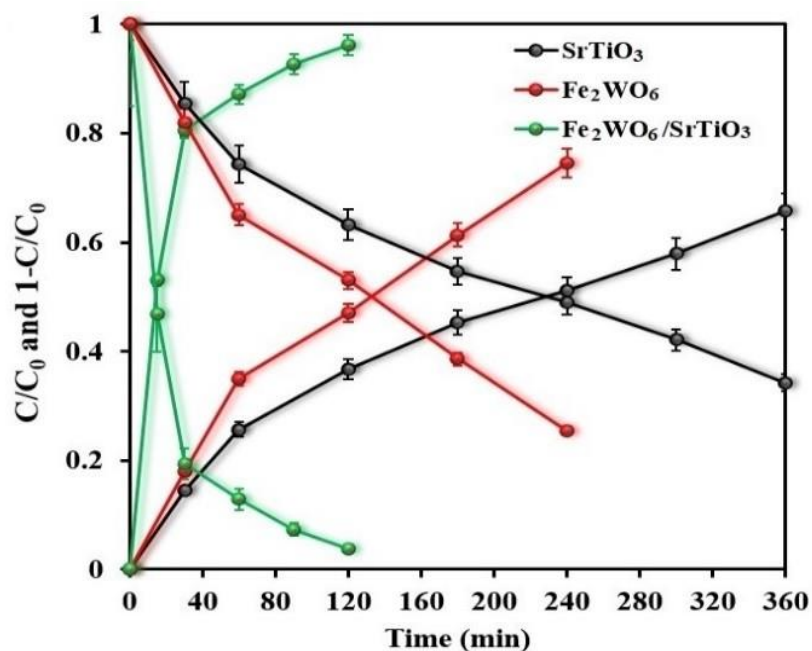
Figure 4.13: The plot of C/C_0 and 1-(C/C_0) versus time in presence of Fe₂WO₆/SrTiO₃, Fe₂WO₆ and SrTiO₃.

Half-life ($t_{1/2}$) period of RhB dye denotes the time required for RhB dye to reduce to half of its initial concentration. The $t_{1/2}$ period of RhB in the presence of pure Fe_2WO_6, pure $SrTiO_3$ and $Fe_2WO_6/SrTiO_3$ composite were determined (Figure 4.13). 20 min was found to be the $t_{1/2}$ periods of RhB in the presence of $Fe_2WO_6/SrTiO_3$ composite as portrayed in Figure 4.13. Nevertheless, 130 min and 230 min were the $t_{1/2}$ periods of pure Fe_2WO_6 and pure $SrTiO_3$, respectively. The $t_{1/2}$ period of RhB in the presence of $Fe_2WO_6/SrTiO_3$ composite was faster compared to that of pure photocatalysts. Enhanced photoactivity of the $Fe_2WO_6/SrTiO_3$ composite can be determined from the reduced $t_{1/2}$ period of RhB than pure Fe_2WO_6 and pure $SrTiO_3$ (Janani et al., 2021; Kokilavani et al., 2021). The $Fe_2WO_6/SrTiO_3$ composite with band gap energy of 2.80 eV was activated by accepting the photon energy from the LED light source. The outstanding removal efficiency was obtained due to higher photocurrent density and smaller arc radius, indicating excellent charge separation efficiency (Sajid, et al., 2020; Zhao, et al., 2021).

4.3 Effect of Process Parameter Studies

The effect of process parameter studies was evaluated to optimize the photodegradation of dyestuff wastewater using the prepared $Fe_2WO_6/SrTiO_3$ composite. The operational parameters to be studied including the Fe_2WO_6 loading in $Fe_2WO_6/SrTiO_3$ composite and solution pH of RhB dye.

4.3.1 Effect of Fe$_2$WO$_6$ Loading
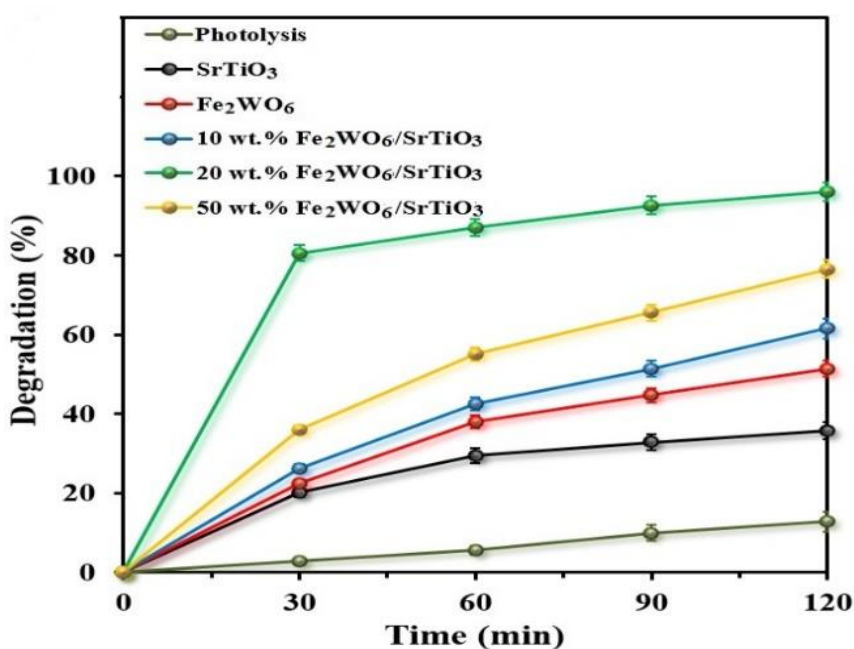
Figure 4.14: The photocatalytic activities of pure Fe$_2$WO$_6$, pure SrTiO$_3$ and Fe$_2$WO$_6$/SrTiO$_3$ composites, for RhB degradation ([RhB] = 5 mg/L; catalyst amount = 0.5 g/L).

In the $Fe_2WO_6/SrTiO_3$ composite, the appropriate ratio of Fe_2WO_6 weight percentage was highly affected the photocatalytic activities. In current study, the Fe_2WO_6 weight percentage was ranging from 10wt.% to 50wt.%. The experiments were carried out in the same conditions of 0.5 g L^{-1} photocatalyst dosage, RhB concentration at 5 mg L^{-1} and solution pH of 12.0. Figure 4.14 displays the removal efficiency of the RhB dye

solution using pure Fe_2WO_6, pure $SrTiO_3$ and $Fe_2WO_6/SrTiO_3$ composites under the LED light irradiation for 120 min. The photodegradation of RhB for pure Fe_2WO_6 and pure $SrTiO_3$ were 51.5% and 35.8%, respectively. When the pure Fe_2WO_6 was added onto the $SrTiO_3$ photocatalyst, the photocatalytic degradation efficacy exhibited significant enhancement. The removal efficiency was increased from 61.6% to 96.1% when increasing Fe_2WO_6 loading from 10 wt% to 20 wt%. However, further increase in the Fe_2WO_6 loading, the photodegradation efficiency of composite was reduced to 76.6%.

The $Fe_2WO_6/SrTiO_3$ composite displayed remarkable removal efficiency as compared to pure Fe_2WO_6 and pure $SrTiO_3$, indicating the addition of Fe_2WO_6 enhanced its photocatalytic performance. Furthermore, as the Fe_2WO_6 loading in the composite increased, the photodegradation efficiency increased. The findings were ascribed to the rapid charge separation of $Fe_2WO_6/SrTiO_3$ composite (G. Zhao et al., 2021; Ferreira et al., 2020). As the loadings of Fe_2WO_6 were added excessively, the degradation efficiency of composite decreased. This result was due to excess Fe_2WO_6 became the recombination center of photogenerated charge carriers, leading to a decrease in photoactivity (W. Chen et al., 2019; Cao et al., 2021). Additionally, the excessive Fe_2WO_6 might increase the opacity, resulting in the decrease of photocatalytic performance (Dou et al., 2022).

Similar finds were reported by Dou et al. (2022). Molybdenum disulfide/cobalt ferrite ($MoS_2/CoFe_2O_4$) sample can reach the best removal efficiency 91.9 % when the molar ratio of MoS_2 to $CoFe_2O_4$ was 2:1. When further increase the molar ratio to 4:1, the degradation efficiency reduced to 82.9%. These results revealed that the excessive amount of MoS_2 became the recombination center of photogenerated charge carriers, resulting in low photoactivity. On the other hand, Chachvalvutikul and colleagues (2019) studied the effect of $FeVO_4$ loading in composite. The addition of the $FeVO_4$ contents from 3 wt% to 6.25 wt%, the photocatalytic degradation efficiency improved from 75.4% to 81.3%. Hence, the excess $FeVO_4$ inhibited the photoactivity of the composite. They explained that the excessive amount of $FeVO_4$ covered the active sites and shaded the composite surface, leading to reduced light absorption and the production of photogenerated charges.

4.3.2 Effect of Solution pH

The solution pH was another important factor in the photocatalytic system, which could affect the ROS generation. In current experiment, the effect of the initial RhB solution pH in the photodegradation performance was performed with pH ranging from 2 to 12, while the other process parameters were remained constant. 2 M NaOH and HCl solution were used to adjust the initial RhB solution pH. Figure 4.15 displays the photocatalytic activities of $Fe_2WO_6/SrTiO_3$ composite at different solution pH conditions under the LED light irradiation for 120 min. In the neutral pH, the photodegradation rate of RhB was low with removal efficiency of 20.7%. Increasing the solution pH to pH 12, the photodegradation efficiencies were 96.1%, respectively. When the solution pH was altered to 2, the photocatalysis efficiency was suppressed to 64.9%.
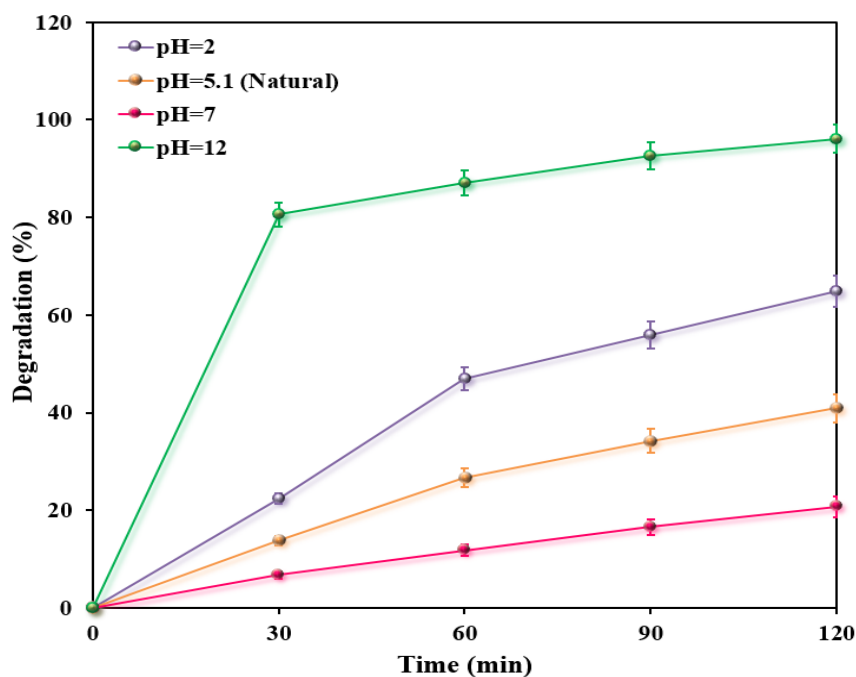
Figure 4.15: The photocatalytic activities by varying the initial solution pH (2-12).

Rhodamine B was a cationic dye which will ionize into positively charged ions in aqueous solution. In addition, the point of zero charge (pZC) value for the $Fe_2WO_6/SrTiO_3$ composite was about pH 8.5. If solution pH > pZC, the surface of composite was negative.

As shown in figure, the outstanding removal efficiency of cationic RhB was obtained at pH 12. This was ascribed to the surface of the Fe_2WO_6/$SrTiO_3$ composite had become negatively charged and attracted to the positively charged RhB molecule by strong electrostatic forces. Moreover, the higher concentration of OH^- ions at higher pH contributed to the production of abundant of •OH radicals, which was responsible for the photodegradation process (El-Shamy, et al., 2020; Janani, et al., 2022). Furthermore, the composite surface and RhB molecules would be positively charged in an acidic environment, which decreased the degradation efficiency because of electrostatic repulsion. Therefore, the outstanding photodegradation performance can be expected under alkaline condition.

Janani and co-workers (2022) examined the effect of pH on the photodegradation of rhodamine B dye using $CaFe_2O_4$-ZnO photocatalyst. The optimum pH in photodegradation of dye was obtained at pH 10. They explained that the excellent photocatalytic performance obtained at higher pH was due to h^+ could generate more •OH radicals under strongly alkaline condition. Another report by M. Ahmad et al. (2021) demonstrated that the highest removal efficiency of rhodamine B was obtained at the alkaline environment. They justified that the remarkable high degradation efficiency was due to the generation of •OH in alkaline environment superior to that in acidic environment.

4.4 Antimicrobial Activities

Antibacterial property of composite was evaluated against *Bacillus cereus* (*B. cereus*) and *Escherichia coli* (*E. coli*). This bacteria selection was owing to their presence in natural water bodies and real industry wastewater. In current study, the photocatalytic disinfection of *B. cereus* (gram-positive) and *E. coli* (gram-negative) were conducted under the visible LED light irradiation. Figure 4.16 displays the zone of inhibition (ZOI) of pure Fe_2WO_6, pure $SrTiO_3$ and Fe_2WO_6/$SrTiO_3$ composite towards *E. coli* and *B. cereus*,

respectively. In details, the ZOI values of pure Fe_2WO_6, pure $SrTiO_3$ and $Fe_2WO_6/SrTiO_3$ composite against *E. coli* were 8 mm, 10 mm and 16 mm, respectively. The results demonstrated that the $Fe_2WO_6/SrTiO_3$ composite exhibited better antibacterial activity than pure $SrTiO_3$ and pure Fe_2WO_6. In addition, the ZOI values of composite against *E. coli* and *B. cereus* were 16 mm and 13mm, respectively. The larger ZOI values of *E. coli* than *B. cereus* can be attributed to the thinner cell wall of *E. coli* cell, which facilitated the penetration of the composite. Table 4.2 depicts the comparison of photocatalytic and antibacterial activities of various composite catalysts relative to the literatures. It was found that the photoactivities of $Fe_2WO_6/SrTiO_3$ composite was satisfactory in degrading organic pollutant and inactivating microorganisms from wastewater.

Table 4.2 Comparison of photocatalytic and antibacterial activities of various composite catalysts.

Catalyst	Light source	Pollutant and concentration	Removal efficiency	Microbe	Antibacterial efficiency	Ref.
TiO_2/WO_3	Xenon lamp, 300 W	TeNT, 1 mg/L	93% within 60 min	*E. faecalis* and *M. luteus*	ZOI*: 13.4, 11.3 mm	(Fakhri et al., 2018)
Ag/ZnO	Mercury lamp, 120 W	Methylene blue, 10 mg/L	98% within 180 min	*E. coli, S. aureus*	ZOI*: 8.8, 14.6 mm	(Nagaraju et al., 2017)
ZnS-CuO/PVA/ Chitosan	tungsten halogen-lamp, 500W	Tetracycline, 25 mg/L	95% within 180min	*E. coli and B. subtilis*	99%	(Janani et al., 2022)
C-dots/Cu_2O/ $SrTiO_3$	Xenon lamp, 500 W	CTC·HCl, 15 mg/L	92% within 90 min	*E. coli*	91.58%	(Zhang et al., 2022)
CeO_2/Ag-$AgVO_3$	Xenon lamp, 300 W	Enrofloxacin, 10 mg/L	100% within 120 min	*E. coli, S. aureus, B. subtilis, and P. aeruginosa*	80%	(Q. Wang et al., 2021b)
FeV_2O_4-Bi_2O_3	Halogen lamp, 500 W	Methylene blue, 10 mg/L	91% within 160 min	*E. coli and B. subtilis*	99%	(Janani et al., 2021)
$Fe_2WO_6/SrTiO_3$	Visible light, 150 W	Rhodamine B, 5 mg/L	96% within 120 min	*E. coli and B. cereus*	ZOI*: 16, 13 mm	Current study
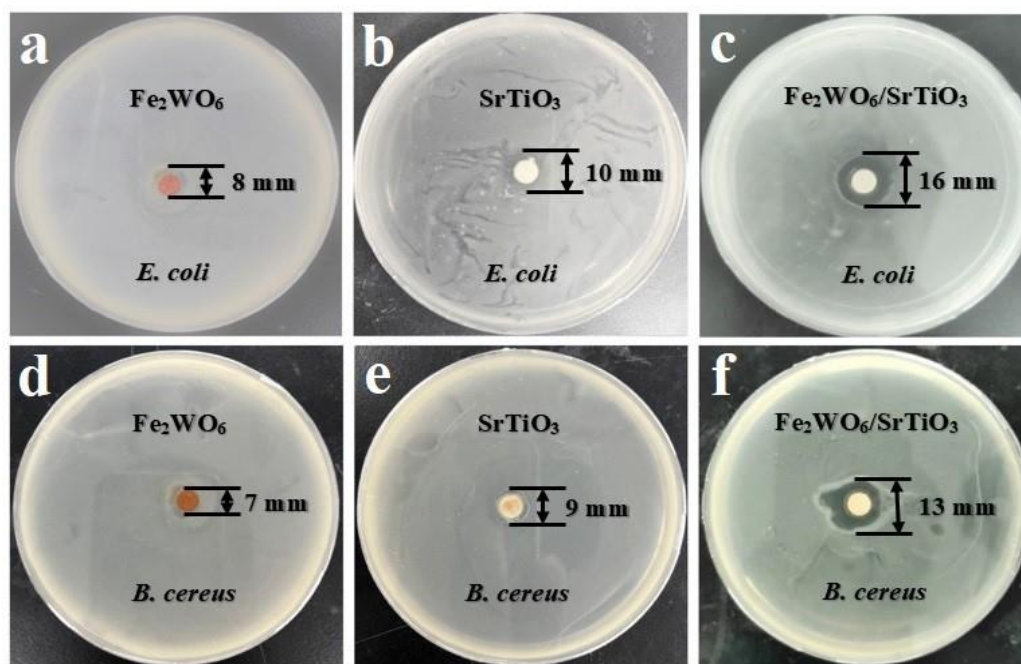
Figure 4.16: Zone of inhibition (ZOI) of pure Fe₂WO₆, pure SrTiO₃ and Fe₂WO₆/SrTiO₃ composites towards disinfection of *E. coli* and *B. cereus*.

The photocatalytic inactivation of bacteria was influenced by various factors, including generation of ROS and metal ions. The generation of metal ions (Sr, Ti, Fe, W) by the photocatalysts that posed a toxicity effect to the bacteria through the denaturing of bacteria DNA (Wang et al., 2020b; Cai et al., 2021a). Under visible LED light conditions, the photocatalyst can generate the ROS. The generated ROS can destroy cell wall or enter the bacteria, leading to cell wall disruption, physiology modification and cell lysis (Vignesh et al., 2019; M. Zhou et al., 2020). The enhanced antibacterial performance of composite can be ascribed to the generation of higher amount ROS can react with the bacterial membrane and result in the death of bacteria. Furthermore, the different antibacterial activities of *B. cereus* cells and *E. coli* cells might be explained as the different structures of the two bacteria (J. Ma et al., 2022a; Cai et al., 2021b). Greater inhibition of growth observed in *E. coli* than *B. cereus*. This may be ascribed to the thinner peptidoglycan layer of gram-negative bacteria, which facilitated the penetration of the

composite (Q. Wang et al., 2021b; Syed et al., 2021b; Janani et al., 2022a). In addition, the membrane of gram-negative bacterial was negatively charged, so *E. coli* was more susceptible to the positively charged metal ions of the composite (Nachimuthu et al., 2022; Munawar et al., 2022; Cai et al., 2021b).

The antibacterial study outcomes in this study also consistent with literature studies. Gnanasekaran and co-works (2022) conducted the photocatalytic antibacterial study against *S. aureus*. The enhanced antibacterial activities were observed on TiO_2/SnO_2 composite compared to pure catalysts (TiO_2 and SnO_2). They explained that the generation of ROS was the key reason for disrupting the bacteria cell wall. Another study carried out by Y. Yang et al. (2021), the photocatalytic disinfection of *Klebsiella pneumonia* (gram-negative) and *Streptococcus pneumonia* (gram-positive) using Au-Ag/CuS nanoparticles material. The results showed the antibacterial activity of prepared samples against *Klebsiella pneumoniae* (*K. pneumoniae*) was better than that of *Streptococcus pneumonia* (*S. pneumonia*). They explained that the thin cell wall of *K. pneumonia* can be easily penetrated by prepared samples.

4.5 Photocatalytic Mechanism Study

4.5.1 Reactive Oxygen Species Responsible for RhB Removal

In the photocatalysis, the reactive oxygen species (ROS) played the considerable roles toward the degradation of RhB molecules. The radical scavenging test was used to check the role of each ROS. The added scavenger would inhibit the photoactivity if this scavenger participated in the photocatalytic process. The trapping experiment were performed using various agents, such as $AgNO_3$ (electron (e^-) trapping agent), EDTA disodium salt (hole (h^+) rapping agent), benzoquinone (superoxide anion radical ($\bullet O_2^-$) trapping agent), or isopropanol (hydroxyl radical ($\bullet OH$) trapping agent) (Kuila et al., 2021; M. Zhang et al., 2020a; Munawar et al., 2020). Figure 4.17 demonstrates the photocatalytic degradation of RhB using composite with and without adding of radical

scavengers. The RhB dye removal efficiency was achieved 96.1% under visible LED light irradiation for 120 min without adding any scavenger. Meanwhile, with the addition of the respective scavenger, the photodegradation rate was deteriorated to 30.4%, 54.4%, 75.5% and 89.9% for $•O_2^-$, h^+, $•OH$ and e^-, respectively. The results revealed the $•O_2^-$ and h^+ were mostly important radicals and followed by $•OH$ and e^-.
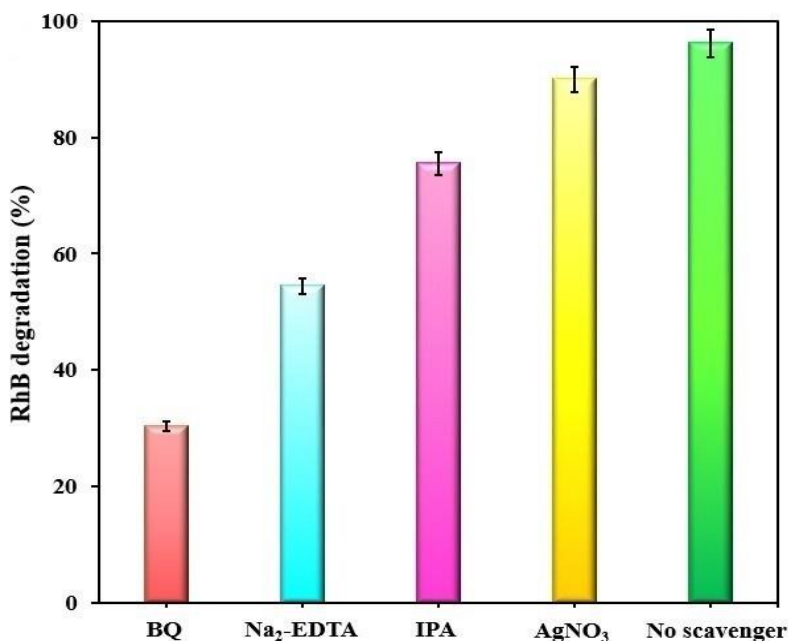
Figure 4.17: Radical scavenger test of Fe₂WO₆/SrTiO₃ composite.

4.5.2 Proposed band structure of S-scheme composite

The mechanism of generation of the ROS can be further inferred by combining the radical scavenging test results together with the band edge potential of the prepared composite. The band edge potential of composite which capable to generate more $•O_2^-$ and $•OH$ species for degradation process when exposed to LED light (Qu et al., 2020; Shao et al., 2019). As described in Sections 4.1.5 and 4.1.6, the band gap energy of SrTiO₃ photocatalyst was 3.40 eV with CB and VB potential of -1.52 eV and 1.88 eV, respectively. The CB potential of SrTiO₃ was more negative than $O_2/•O_2^-$ (-0.33 eV) (L. Jiang et al., 2018a; Y. Yu et al., 2022; Xue et al., 2022). Therefore, the SrTiO₃ was able to reduce O₂

to form $\bullet O_2^-$ radicals for the photocatalytic process (X. Yu et al., 2020; Qiao et al., 2019; Stelo et al., 2020). However, the VB potential of $SrTiO_3$ was less positive in comparison to those of $H_2O/\bullet OH$ (+2.68 eV) and $OH^-/\bullet OH$ (+2.29 eV) (Ye et al., 2019; T. Xu et al., 2019; Y. Yu et al., 20222). Additionally, the photogenerated h^+ on the VB of $SrTiO_3$ could not react with OH^- or H_2O to product $\bullet OH$. As a result, no $\bullet OH$ radicals can be generated for the photocatalysis. The result of this experiment was well-aligned with the published papers (Shao et al., 2019; G. Jiang et al., 2018b; H. Sun et al., 2022b). In the papers, the holes on the VB of photocatalyst could not react with OH^- or H_2O to product $\bullet OH$ owing to the VB potential of photocatalyst was less positive as compared to the $OH^-/\bullet OH$ potential (+2.29 eV).

In addition, the composite coupled by Fe_2WO_6 and $SrTiO_3$ can generate ROS such as $\bullet O_2^-$ and $\bullet OH$ species for the photodegradation process. The band gap energy of Fe_2WO_6 was 2.05 eV with VB position at 2.90 eV. These characteristics were contributed to the generation of $\bullet OH$ as the VB potential of Fe_2WO_6 was more positive than the redox potential of $H_2O/\bullet OH$ (+2.68 eV) and $OH^-/\bullet OH$ (+2.29 eV) (X. Wu et al., 2022; F. Zhao et al., 2020; Kuila et al., 2021). Moreover, the photodegradation rate was deteriorated with the addition of the scavenger of h^+. The results can be explained as photogenerated h^+ can directly participate the oxidation of organic pollutants (X. Wu et al., 2022; F. Zhao et al., 2020; Y. Zhang et al., 2022b). When the e^- was scavenged in the aqueous solution, the degradation rate exhibited minor decrease. This could be assigned to the S-scheme heterostructure constructed by Fe_2WO_6 and $SrTiO_3$ photocatalyst trapped the e^- which boosting the separation and transport of photo-inducted charge carriers between the interface of two photocatalysts (P. Xia et al., 2020; X. Chen et al., 2022). The possible mechanism for RhB photodegradation over $Fe_2WO_6/SrTiO_3$ composite under the visible LED light irradiation was depicted in Figure 4.18.
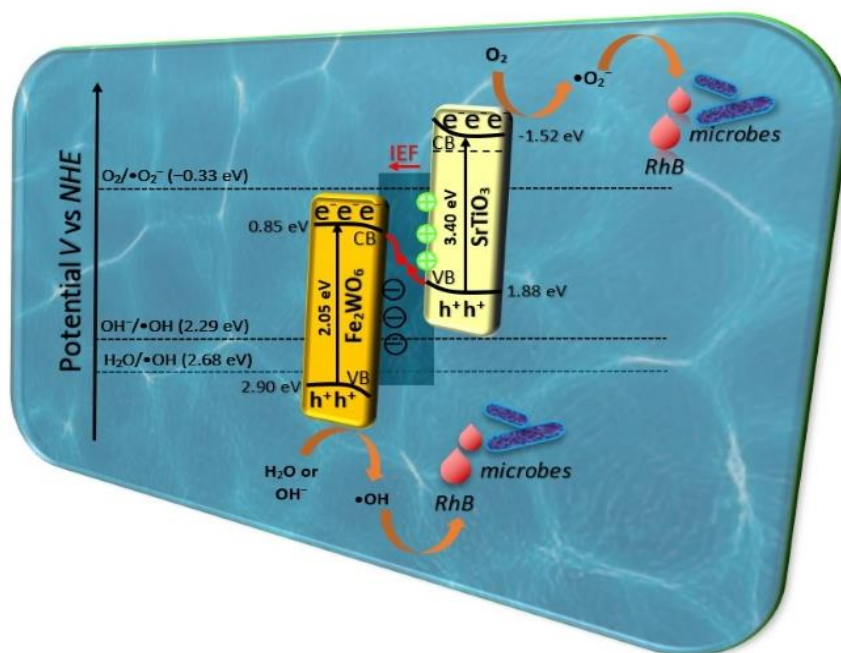
Figure 4.18: Schematic diagram for mechanism of RhB degradation over Fe₂WO₆/SrTiO₃ composite.

4.6 Photocatalyst Recycling Test

The reusability of pure $SrTiO_3$ and $Fe_2WO_6/SrTiO_3$ composite were evaluated through the recycling test. Generally, five cycle tests were conducted on the degradation of RhB. After each cycle, the photocatalyst was washed by deionized water and alcohol for three times followed by drying overnight (Chang et al., 2021; Shao et al., 2019). Figure 4.19 demonstrates the recycling test of the optimized catalyst with five consecutive runs under visible LED light irradiation for 120 min. With the increase of cycle times, the degradation percentage of RhB decreased slightly. The results indicated that the photodegradation of RhB using the fresh $Fe_2WO_6/SrTiO_3$ composite reached 96.1% in the first experiment. In the fifth cycle, the dye removal efficiency remained notably high at 93.9%. In addition, the removal efficiency for pure $SrTiO_3$ reduced from 35.8% to 28.5%.
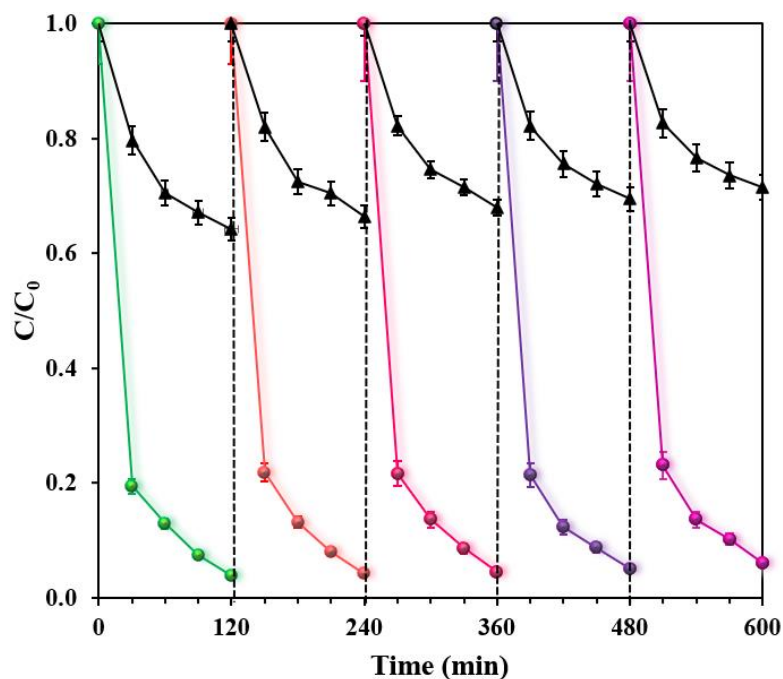
Figure 4.19: The Recycling Experiment for the Photocatalytic Degradation of RhB over pure SrTiO$_3$ and Fe$_2$WO$_6$/SrTiO$_3$ composite.

The photocatalytic performance of Fe$_2$WO$_6$/SrTiO$_3$ composite remained at high dye removal efficiency after five cycles indicated the highly stable of the synthesized Fe$_2$WO$_6$/SrTiO$_3$ composite (Y. Ma et al., 2022b; G. Zhou et al., 2022; X. Li et al., 2021d). Moreover, the degradation efficiency for pure SrTiO$_3$ was significantly reduced after five cycles, which indicated that the introduction of Fe$_2$WO$_6$ could improve the reusability of SrTiO$_3$ (Y. Lin et al., 2018). The high stability of the composite revealed that it still had higher capability to generate more radicals after several cycle experiments. However, the slightly deterioration in the dye removal efficiency after the five cycles could be assigned to the loss of a certain amount of photocatalyst in the collection process (Cheng et al., 2022; Veisi et al., 2021). At the same time, the available active sites of the photocatalyst decreased after several cycle experiments due to the adsorbed RhB molecules or intermediate products, thus leading to the insignificant declination in dye removal (Shao et al., 2019; Chachvalvutikul, Luangwanta and Kaowphong, 2021).

The results of the current recycling experiment were agreed to several literature reports. Chinnathambi (2022) tested the reusability of FeV_2O_4-ZnO for the MB dye photodegradation under 200 min. The result displayed that the degradation level retained almost same for 5 consecutive cycles that revealed high stability and reusability of FeV_2O_4-ZnO sample. Furthermore, another catalyst feasibility test conducted by Q. Wang and colleagues (2021b) also illustrated high photocatalytic activities toward enrofloxacin using CeO_2/Ag-AgVO$_3$ composite. The photoactivity of composite remained high after four cycles and could achieve 90% of the photoactivity of fresh composite. The results revealed that the synthesized composite possessed outstanding stability and reusability.

4.7 Actual Printed Ink Wastewater Study

The optimized Fe_2WO_6/SrTiO$_3$ composite was also tested using actual wastewater to reveal its potential application in wastewater treatment. RhB was used as the synthetic dyestuff wastewater as it was widely adopted in various industries including textile, paper and printing factories. As shown in the Figure 4.20, the initial COD of RhB dye was 81 mg L^{-1} and the COD value of the wastewater after 4 hours photocatalytic treatment was 11 mg L^{-1}, which corresponding to the COD removal efficiency of 86.4 %. The outstanding mineralization efficiency showed that the optimized Fe_2WO_6/SrTiO$_3$ composite can degrade RhB dye. Besides, the printed ink wastewater was selected in this study as the actual wastewater due to it contained various organic contaminants including dyestuffs. The COD values of the actual wastewater before and after photocatalytic reaction was 181 mg L^{-1} and 40 mg L^{-1}, respectively. The above results indicated the COD removal of actual wastewater was 78%. The high mineralization efficiency demonstrated that the photogenerated ROS can degrade the organic pollutants in the actual printed ink wastewater. Overall, the optimized Fe_2WO_6/SrTiO$_3$ photocatalyst show its promising prospects in the real wastewater purification.
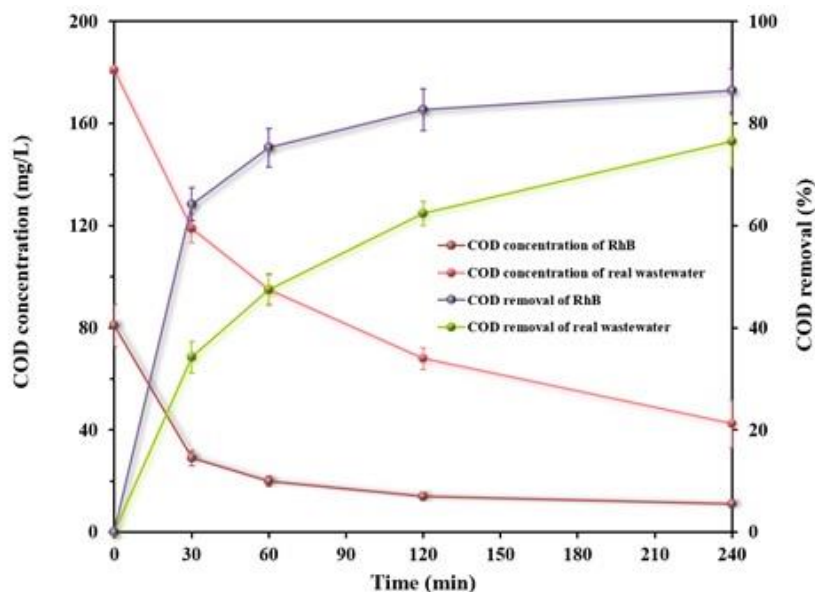
Figure 4.20: COD removal of RhB dye and real printed ink wastewater.

4.8 Electrical Energy per Order Study

The experiments were executed using the similar solution pH and initial concentration of RhB dye for pure Fe_2WO_6, pure $SrTiO_3$ and $Fe_2WO_6/SrTiO_3$ composites under the irradiation of visible light. The estimated E_{EO} values of photocatalysts were tabulated in Table 4.3. These values exhibited that the $Fe_2WO_6/SrTiO_3$ nanocomposite decreased the E_{EO} values for the photodegradation of RhB dye compared with pure Fe_2WO_6 as well as pure $SrTiO_3$, indicated that the composites were highly efficient and utilized the less input energy to degrade per unit volume of organic pollutant. Some reports in the literature had also applied this useful value to make a cost comparison. For instance, Vaiano and colleagues (2017) investigated the degradation of crystal violet dye using N-$TiO_2/SrSiP$, where the E_{EO} value in this research was 103.87 kWhm^{-3}order^{-1} for the photodegradation of crystal violet dye. According to the study conducted by Ferreira et al. (2020), the E_{EO} value of 1777 kWhm^{-3}order^{-1} was obtained with the UV LEDs system that was used for the photocatalytic removal of p-hydroxybenzoic acid (pHBA).

Table 4.3: E_{EO} values of RhB dye degradation systems using various photocatalysts.

System	K (min^{-1})	E_{EO} (kWhm^{-3}order^{-1})
SrTiO$_3$	0.0043	8930.23
Fe$_2$WO$_6$	0.0065	5907.69
10 wt.% Fe$_2$WO$_6$/SrTiO$_3$	0.0082	4682.93
20 wt.% Fe$_2$WO$_6$/SrTiO$_3$	0.0297	1292.93
50 wt.% Fe$_2$WO$_6$/SrTiO$_3$	0.0123	3121.95

CHAPTER 5

CONCLUSION AND RECOMMENDATIONS

5.1 Conclusion

In current study, the composite was successfully prepared using a simple hydrothermal method and applied in the dyestuff treatment and antimicrobial activity under visible LED light irradiation. The as synthesized photocatalysts were characterized through FESEM, HRTEM, EDX, XRD, FTIR, UV-vis DRS and photoelectrochemical analyses. The irregular structure Fe_2WO_6 and cubic-like particle $SrTiO_3$ were witnessed in the microscopic images. Fe_2WO_6 photocatalyst were found to disperse on the surface of cube-like structures of $SrTiO_3$ particles. The HRTEM images of $Fe_2WO_6/SrTiO_3$ composite demonstrated that the intimate interface between Fe_2WO_6 and $SrTiO_3$ confirmed the formation of heterojunction in the composite, which was useful for charge transfer and separation in photocatalytic degradation. The EDX analysis for $Fe_2WO_6/SrTiO_3$ composite illustrated Sr, Ti, Fe, W and O elements were clearly observed in the composite.

Moreover, the XRD analysis revealed that the pure Fe_2WO_6 existed as an orthorhombic phase and the pure $SrTiO_3$ existed as a cubic perovskite phase. The FTIR analysis demonstrated that the typical peaks from both pure $SrTiO_3$ and pure Fe_2WO_6 can be found in the FTIR spectra of composite. The FTIR analysis demonstrated the intensities of O-H peak in the composites were much stronger than pure $SrTiO_3$ and pure Fe_2WO_6, reveling that the hydroxyl-rich surface of composite ameliorated the photocatalytic performance. Moreover, the UV-Vis DRS analysis displayed the $Fe_2WO_6/SrTiO_3$

composite possessed smaller band gap energy (2.80 eV) than pure $SrTiO_3$. The findings were attributed to the fact that pure $SrTiO_3$ with wide band gap was constricted with the addition of Fe_2WO_6 forming narrower band gap of $Fe_2WO_6/SrTiO_3$ composite materials. The photoelectrochemical experiments demonstrated that $Fe_2WO_6/SrTiO_3$ exhibited the improved the electron-hole pairs separation, which was beneficial for the photoactivity.

Using the RhB as the model pollutant, the $Fe_2WO_6/SrTiO_3$ composite demonstrated better visible light photoactivity in comparison with those of pure Fe_2WO_6 and pure $SrTiO_3$, respectively. The outstanding photoactivity was due to the excellent charge separation efficiency favoring the production of ROS. Furthermore, the effect of several process parameter studies including Fe_2WO_6 loadings in composite, photocatalyst dosage and the initial solution pH were investigated. The optimum process parameters for dye removal were found out to be 20 wt.% Fe_2WO_6 content, 0.5 g L^{-1} photocatalyst dosage and pH 12. A notable photodegradation efficiency of RhB was achieved at 96.1% using the $Fe_2WO_6/SrTiO_3$ composite when exposed to visible LED light irradiation for 120 min.

Additionally, the antimicrobial activity of the synthesized photocatalysts were determined against the disinfection activities of *E. coli* and *B. cereus* under visible LED light exposure. The order of the antibacterial performance for synthesized photocatalysts was as followed: $Fe_2WO_6/SrTiO_3$ composite > pure $SrTiO_3$ > pure Fe_2WO_6. The ameliorated photocatalytic inactivation of bacteria can be ascribed to the following reasons: (1) The generation of metal ions (Sr, Ti, Fe, W) by the photocatalysts that posed a toxicity effect to the bacteria through the denaturing of bacteria DNA; (2) The generated ROS can damage the cell wall or enter the bacteria, leading to cell wall disruption, physiology modification and cell lysis. Moreover, $Fe_2WO_6/SrTiO_3$ composites was more toxic to *E. coli* and *B. cereus* due to the thinner layer of gram-negative bacteria.

Moreover, the roles of reactive oxygen species (ROS) during the photoreaction were also studied. The findings revealed the $•O_2^-$ and h^+ were mostly important radicals, following by $•OH$ and e^-. This can be attributed to the band edge potential of the synthesized composite, which was capable to generate more $•O_2^-$ and $•OH$ species for

degradation process under visible LED light exposure. A probable mechanism for RhB degradation over $Fe_2WO_6/SrTiO_3$ composite under the visible LED light irradiation was also brought forward.

Additionally, the recyclability of the optimized composite was evaluated through the recycling test. The $Fe_2WO_6/SrTiO_3$ composite displayed outstanding recyclability which attained high removal efficiency of 93.9% after five successive runs. A slight deterioration in the dye removal efficiency of the reused sample over the five cycles was observed, which could be assigned to the loss of active sites of the photocatalyst in several cycle experiments. Furthermore, the printed ink wastewater was selected as actual wastewater in order to reveal the potential application of the optimized composite for COD removal. The mineralization efficiency of actual wastewater can reach 78% after 4 hours. Overall, this study revealed that the synthesized $Fe_2WO_6/SrTiO_3$ composite had satisfactory performance in degrading the organic contaminants and disinfecting the bacteria in the actual dye-containing wastewater.

5.2 Recommendations

Following the completion of the current study, photocatalysis principle, some semiconductor materials properties and various engineering basics were learned and should be considered in the future study.

1. The XPS analyses could be studied to further analyze the chemical composition and surface chemical state of photocatalyst.
2. The HPLC and LC-MS analyses could be carried out to further evaluate the intermediates that may be produced in the photodegradation process and further study the possible mechanism of photodegradation.
3. The effect of other operation parameters including the rate of air flow and light intensity could be investigated to further ameliorate the removal efficiency.
4. The protein leakage and K^+ leakage assays could be conducted to further study the antibacterial efficiency of photocatalyst.

REFERENCES

Abdi, F.F., Chemseddine, A., Berglund, S.P. and van de Krol, R., 2017. Assessing the suitability of iron tungstate (Fe_2WO_6) as a photoelectrode material for water oxidation. *The Journal of Physical Chemistry C*, 121, pp.153-160.

Adegoke, K.A., Adegoke, O.R., Araoye, A.O., Ogunmodede, J., Agboola, O.S. and Bello, O.S., 2022. Engineered raw, carbonaceous, and modified biomass-based adsorbents for Rhodamine B dye removal from water and wastewater. *Bioresource Technology Reports*, 18, pp. 101082.

Ahmad, M., Rehman, W., Khan, M. M., Qureshi, M. T., Gul, A., Haq, S., Ullah, R., Rab, A. and Menaa, F., 2021. Phytogenic fabrication of ZnO and gold decorated ZnO nanoparticles for photocatalytic degradation of Rhodamine B. *Journal of Environmental Chemical Engineering*, 9, pp. 104725.

Ahmad, I., Shukrullah, S., Naz, M. Y., Ullah, S. and Assiri, M. A., 2022. Designing and modification of bismuth oxyhalides BiOX (X= Cl, Br and I) photocatalysts for improved photocatalytic performance. *Journal of Industrial and Engineering Chemistry*, 105, pp. 1-33.

Ahmadi, M., Dorraji, M. S., Hajimiri, I. and Rasoulifard, M. H., 2021. The main role of CuO loading against electron-hole recombination of $SrTiO_3$: Improvement and investigation of photocatalytic activity, modeling and optimization by response surface methodology. *Journal of Photochemistry and Photobiology A: Chemistry*, 404, pp. 112886.

Ajibade,T.F., Tian, H., Lasisi, K.H., Xue, Q., Yao, W. and Zhang, K., 2021. Multifunctional PAN UF membrane modified with 3D-MXene/O-MWCNT nanostructures for the removal of complex oil and dyes from industrial wastewater. *Separation and Purification Technology*, 275, pp. 119135.

Alimohammadi, E., Mahdikhah, V. and Sheibani, S., 2022. Type-II band alignment in CNT-modified $SrTiO_3$-Fe_2TiO_5 heterostructure nanocomposite for photocatalytic degradation of organic dyes. *Applied Surface Science*, 598, pp. 153816.

Al-Mamun, M.R., Kader, S., Islam, M.S. and Khan, M.Z.H., 2019. Photocatalytic activity improvement and application of UV-TiO_2 photocatalysis in textile wastewater treatment: A review. *Journal of Environmental Chemical Engineering*, 7, pp.103248.

Anantha, M. S., Jayanth, V., Olivera, S., Anarghya, D., Venkatesh, K., Jayanna, B. K., Sachin, H. P. and Muralidhara, H. B., 2021. Microwave treated Bermuda grass as a novel photocatalyst for the treatment of methylene blue dye from wastewater. *Environmental Nanotechnology, Monitoring and Management*, 15, pp. 100447.

Antonopoulou, M., Kosma, C., Albanis, T. and Konstantinou, I., 2021. An overview of homogeneous and heterogeneous photocatalysis applications for the removal of pharmaceutical compounds from real or synthetic hospital wastewaters under lab or pilot scale. *Science of The Total Environment*, 765, pp. 144163.

Asaithambi, P., Alemayehu, E., Sajjadi, B. and Aziz, A.R.A., 2017. Electrical energy per order determination for the removal pollutant from industrial wastewater using $UV/Fe^{2+}/H_2O_2$ process: optimization by response surface methodology. *Water Resources and Industry*, 18, pp. 17-32.

Ashwini, K., Rajanaika, H., Anantharaju, K.S., Nagabhushanad, H., Reddy, P.A., Shetty, K. and Mahesh, K.V., 2017. Synthesis and characterization of as-formed and calcined $MnFe_2O_4$ nanoparticles: a comparative study of their antibacterial activities. *Materials Today: Proceedings*, 4, pp.11902-11909.

Awfa, D., Ateia, M., Fujii, M. and Yoshimura, C., 2019. Novel magnetic carbon nanotube-TiO_2 composites for solar light photocatalytic degradation of pharmaceuticals in the presence of natural organic matter. *Journal of Water Process Engineering*, 31, pp. 100836.

Agboola, P. O. and Shakir, I., 2022. Facile fabrication of $SnO_2/MoS_2/rGO$ ternary composite for solar light-mediated photocatalysis for water remediation. *Journal of Materials Research and Technology*, 18, pp. 4303-4313.

Baaloudj, O., Assadi, I., Nasrallah, N., El Jery, A., Khezami, L. and Assadi, A. A., 2021. Simultaneous removal of antibiotics and inactivation of antibiotic-resistant bacteria by photocatalysis: A review. *Journal of Water Process Engineering*, 42, pp. 102089.

Balasurya, S., Alfarraj, S., Raju, L. L., Chinnathambi, A., Alharbi, S. A., Thomas, A. M. and Khan, S. S., 2021. Novel $CoWO_4-Ag_2MoO_4$ NCs: Synthesis, enhanced photocatalytic activity under visible-light irradiation and its antimicrobial activity. *Surfaces and Interfaces*, 25, pp. 101237.

Balouiri, M., Sadiki, M. and Ibnsouda, S. K., 2016. Methods for *in vitro* evaluating antimicrobial activity: A review. *Journal of pharmaceutical analysis*, 6, pp. 71-79.

Behzadifard, Z., Shariatinia, Z. and Jourshabani, M., 2018. Novel visible light driven $CuO/SmFeO_3$ nanocomposite photocatalysts with enhanced photocatalytic activities for degradation of organic pollutants. *Journal of Molecular Liquids*, 262, pp. 533-548.

Bello, O. S., Adegoke, K. A., Fagbenro, S. O. and Lameed, O. S., 2019. Functionalized coconut husks for rhodamine-B dye sequestration. *Applied Water Science*, 9, pp. 189.

Bhat, A. P. and Gogate, P. R.,2021. Degradation of nitrogen-containing hazardous compounds using advanced oxidation processes: A review on aliphatic and aromatic amines, dyes, and pesticides. *Journal of Hazardous Materials*, 403, pp. 123657.

Bhagat, M., Anand, R., Datt, R., Gupta, V. and Arya, S., 2019. Green synthesis of silver nanoparticles using aqueous extract of *Rosa brunonii Lindl* and their morphological, biological and photocatalytic characterizations. *Journal of Inorganic and Organometallic Polymers and Materials*, 29, pp. 1039-1047.

Cai, Y., Yang, F., Wu, L., Shu, Y., Qu, G., Fakhri, A. and Gupta, V. K., 2021a. Hydrothermal-ultrasonic synthesis of CuO nanorods and $CuWO_4$ nanoparticles for catalytic reduction, photocatalysis activity, and antibacterial properties. *Materials Chemistry and Physics*, 258, pp. 123919.

Cai, Y., Cheng, W., Ji, C., Su, Z. and Yin, M., 2021b. Perylenediimide/silver nanohybrids with visible-light photocatalysis enhanced antibacterial effect. *Dyes and Pigments*, 195, pp. 109698.

Cao, J., Jing, Y., Du, Z., Chu, W., Li, J. and Cen, W., 2021. WC/BiOCl binary composite photocatalyst for accelerating interfacial charge separation and sulfamethoxazole degradation. *Applied Surface Science*, 570, pp. 151201-151212.

Chachvalvutikul, A., Jakmunee, J., Thongtem, S., Kittiwachana, S. and Kaowphong, S., 2019. Novel $FeVO_4/Bi_7O_9I_3$ nanocomposite with enhanced photocatalytic dye degradation and photoelectrochemical properties. *Applied Surface Science*, 475, pp. 175-184.

Chachvalvutikul, A., Luangwanta, T. and Kaowphong, S., 2021. Double Z-scheme $FeVO_4/Bi_4O_5Br_2/BiOBr$ ternary heterojunction photocatalyst for simultaneous photocatalytic removal of hexavalent chromium and rhodamine B. *Journal of Colloid and Interface Science*, 603, pp. 738-757.

Chai, H. Y., Lam, S. M. and Sin, J. C., 2019. Green synthesis of magnetic Fe-doped ZnO nanoparticles via *Hibiscus rosa-sinensis* leaf extracts for boosted photocatalytic, antibacterial and antifungal activities. *Materials Letters*, 242, pp. 103-106.

Chang, N., Chen, Y. R., Xie, F., Liu, Y. P. and Wang, H.T., 2021. Facile construction of Z-scheme AgCl/Ag-doped-ZIF-8 heterojunction with narrow band gaps for efficient visible-light photocatalysis. *Colloids and Surfaces A: Physicochemical and Engineering Aspects*, 616, pp. 126351.

Chen, P., Cai, Y., Wang, J., Wang, K., Tao, Y., Xue, J. and Wang, H.,2018. Preparation of protonized titanate nanotubes/Fe_3O_4/TiO_2 ternary composites and dye self-sensitization for visible-light-driven photodegradation of Rhodamine B. *Powder Technology*, 326, pp. 272-280.

Chen, W., Mo, J., Du, X., Zhang, Z. and Zhang, W., 2019. Biomimetic dynamic

membrane for aquatic dye removal. *Water research*, 151, pp. 243-251.

Chen, Y., Jiang, Z., Xu, L., Liu, C., Cheng, Y., Zou, Y. and Zhang, Q., 2021. Composite magnetic photocatalyst $Bi_{24}O_{31}Br_{10}/NiFe_2O_4$: Hydrothermal preparation, characterization and photocatalytic mechanism. *Materials Science in Semiconductor Processing*, 126, pp. 105669-105680.

Chen, X., Guo, R.T., Pan, W.G., Yuan, Y., Hu, X., Bi, Z.X. and Wang, J., 2022. A novel double S-scheme photocatalyst $Bi_7O_9I_3/Cd_{0.5}Zn_{0.5}S$ QDs/$WO_{3-x}$with efficient full-spectrum-induced phenol photodegradation. *Applied Catalysis B: Environmental*, 318, pp. 121839.

Cheng, L., Zhang, Y., Fan, W. and Ji, Y., 2022. Synergistic adsorption-photocatalysis for dyes removal by a novel biochar-based Z-scheme heterojunction $BC/2ZIS/WO_3$: Mechanistic investigation and degradation pathways. *Chemical Engineering Journal*, 445, pp. 136677.

Chinnathambi, A., 2022. Synthesis and characterization of spinel FeV_2O_4 coupled ZnO nanoplates for boosted white light photocatalysis and antibacterial applications. *Journal of Alloys and Compounds*, 890, pp. 161742.

Corzo-Ríos, L. J., Sánchez-Chino, X. M., Cardador-Martínez, A., Martínez-Herrera, J. and Jiménez-Martínez, C., 2020. Effect of cooking on nutritional and non-nutritional compounds in two species of Phaseolus (*P. vulgaris* and *P. coccineus*) cultivated in Mexico. *International Journal of Gastronomy and Food Science*, 20, pp. 100206.

Dey, P., Mahapatra, B.S., Juyal, V.K., Pramanick, B., Negi, M.S., Paul, J. and Singh, S.P., 2021. Flax processing waste – A low-cost, potential biosorbent for treatment of heavy metal, dye and organic matter contaminated industrial wastewater, *Industrial Crops and Products*, 174, pp. 114195.

Denamur, E., Clermont, O., Bonacorsi, S. and Gordon, D., 2021. The population genetics of pathogenic *Escherichia coli*. *Nature Reviews Microbiology*, 19, pp. 37-54.

Ding, X., Gutierrez, L., Croue, J. P., Li, M., Wang, L. and Wang, Y., 2020. Hydroxyl and sulfate radical-based oxidation of RhB dye in UV/H_2O_2 and UV/persulfate systems: Kinetics, mechanisms, and comparison. *Chemosphere*, 253, pp. 126655.

Dong, S., Cui, L., Tian, Y., Xia, L., Wu, Y., Yu, J., Bagley, D.M., Sun, J. and Fan, M., 2020. A novel and high-performance double Z-scheme photocatalyst $ZnO-SnO_2$-Zn_2SnO_4 for effective removal of the biological toxicity of antibiotics. *Journal of Hazardous Materials*, 399, pp. 123017.

Dou, K., Lu, Y., Wang, R., Cao, H., Yao, C., Liu, J., Tsidaeva, N. and Wang, W., 2022. $(1T/2H)-MoS_2/CoFe_2O_4$ heterojunctions with a unique grape bunch structure for photocatalysis of organic dyes driven by visible light. *Applied Surface Science*, 605, pp. 154751.

Duan, X., Yang, J., Hu, G., Yang, C., Chen, Y., Liu, Q., Ren, S. and Li, J., 2021. Optimization of TiO_2/ZSM-5 photocatalysts: Energy band engineering by solid state diffusion method with calcination. *Journal of Environmental Chemical Engineering*, 9, pp. 105563-105574.

Dutta, V., Sharma, S., Raizada, P., Thakur, V. K., Khan, A. A. P., Saini, V., Asiri, A. M. and Singh, P., 2021. An overview on WO_3 based photocatalyst for environmental remediation. *Journal of Environmental Chemical Engineering*, 9, pp. 105018.

Egbuikwem, P.N., Mierzwa, J.C. and Saroj, D.P., 2020. Evaluation of aerobic biological process with post-ozonation for treatment of mixed industrial and domestic wastewater for potential reuse in agriculture. *Bioresource Technology*, 318, pp. 124200.

El-Shamy, A., 2020. Synthesis of new magnesium peroxide (MgO_2) nano-rods for pollutant dye removal and antibacterial applications. *Materials Chemistry and Physics*, 243, pp. 122640.

Eskandari, N., Nabiyouni, G., Masoumi, S. and Ghanbari, D., 2019. Preparation of a new magnetic and photo-catalyst $CoFe_2O_4$-$SrTiO_3$ perovskite nanocomposite for photo-degradation of toxic dyes under short time visible irradiation. *Composites Part B: Engineering*, 176, pp. 107343.

Espinosa-Angeles, J.C., Goubard-Bretesché, N., Quarez, E., Payen, C., Sougrati, M.T., Crosnier, O. and Brousse, T., 2021. Investigating the cycling stability of Fe_2WO_6 pseudocapacitive electrode materials. *Nanomaterials*, 11, pp. 1405.

Fakhri, A., Azad, M., Fatolahi, L. and Tahami, S., 2018. Microwave-assisted photocatalysis of neurotoxin compounds using metal oxides quantum dots/nanosheets composites: Photocorrosion inhibition, reusability and antibacterial activity studies. *Journal of Photochemistry & Photobiology B: Biology*, 178, pp. 108-114.

Faraji, A., Mehrdadi, N., Mahmoodi, N.M., Baghdadi, M. and Pardakhti, A., 2021. Enhanced photocatalytic activity by synergic action of ZIF-8 and $NiFe_2O_4$ under visible light irradiation. *Journal of Molecular Structure*, 1223, pp. 129028-129037.

Feizpoor, S., Habibi-Yangjeh, A., Chand, H. and Krishnan, V., 2021. Integration of Bi_5O_7I with TiO_2: Binary photocatalysts with boosted visible-light photocatalysis in removal of organic contaminants. *Journal of Photochemistry and Photobiology A: Chemistry*, 410, pp. 113190-113203.

Ferreira, M.A., da Silva, G.T., Lopes, O.F., Mastelaro, V.R., Ribeiro, C., Pires, M.J., Malagutti, A.R., Jr., W.A. and Mourao, H.A., 2020. Fabrication of $SrTiO_3$/g-C_3N_4 heterostructures for visible light-induced photocatalysis. *Materials Science in Semiconductor Processing*, 108, pp. 104887.

Gao, X., Zhang, Y., Dai, Y. and Fu, F., 2016. High-performance magnetic carbon materials in dye removal from aqueous solutions. *Journal of Solid State Chemistry*,

239, pp. 265-273.

Gao, H., Yang, H. and Wang, S., 2018. Hydrothermal synthesis, growth mechanism, optical properties and photocatalytic activity of cubic $SrTiO_3$ particles for the degradation of cationic and anionic dyes, *Optik*, 175, pp. 237-249.

Gao, J., Shen, J., Maouche, C., Ali, R.N., Yang, J. and Liu, Q., 2022. Enhanced antibacterial performance in water over the nanostructured heterojunction photocatalysts: A review. *Journal of Cleaner Production*, 372, pp.133770.

Ghorai, K., Panda, A., Bhattacharjee, M., Mandal, D., Hossain, A., Bera, P., Seikh, M.M. and Gayen, A., 2021a. Facile synthesis of $CuCr_2O_4/CeO_2$ nanocomposite: A new Fenton like catalyst with domestic LED light assisted improved photocatalytic activity for the degradation of RhB, MB and MO dyes. *Applied Surface Science*, 536, pp. 147604.

Ghorai, K., Bhattacharjee, M., Mandal, D., Hossain, A., Bhunia, T., Das, M., Ray, p., Show, B., Bera, P., Mandal, T.K., Seikh, M.M. and Gayen, A., 2021b. Facile synthesis of $CuCr_2O_4/BiOBr$ nanocomposite and its photocatalytic activity towards RhB and tetracycline hydrochloride degradation under household visible LED light irradiation. *Journal of Alloys and Compounds*, 867, pp. 157947.

Gnanasekaran, L., Rajendran, S., Kumar, P. S., Priya, A. K., Gracia, F., Habila, M. A. and Saravanakumar, K., 2022. Visible light stimulated binary nanostructure and defect enriched TiO_2-SnO_2 for photocatalysis and antibacterial activity. *Materials Letters*, 316, pp. 131998.

Gomes, D.S., Gando-Ferreira, L.M., Quinta-Ferreira, R.M. and Martins, R.C., 2018. Removal of sulfamethoxazole and diclofenac from water: Strategies involving O_3 and H_2O_2. *Environmental technology*, 39, pp. 1658-1669.

Grabowska, E., 2015. Selected perovskite oxides: Characterization, preparation and photocatalytic properties-a review. *Applied Catalysis B: Environmental*, 186, pp. 97-126.

Gusain, R., Kumar, N. and Sinha, S., 2020. Recent advances in carbon nanomaterial-based adsorbents for water purification. *Coordination Chemistry Reviews*, 405, pp. 213111.

Guo, M., Liu, Q., Wu, M., Lv, T. and Jia, L., 2018. Novel reduced graphene oxide wrapped-$SrTiO_3$ flower-like nanostructure with Ti-C bond for free noble metal decomposition of formic acid to hydrogen. *Chemical Engineering Journal*, 334, pp.1886-1896.

Han, J., Dai, F., Liu, Y., Zhao, R., Wang, L. and Feng, S., 2019. Synthesis of $CdSe/SrTiO_3$ nanocomposites with enhanced photocatalytic hydrogen production activity. *Applied Surface Science*, 467, pp. 1033-1039.

Hassanpour, M., Hosseini Tafreshi, S.A., Amiri, O., Hamadanian, M. and Salavati-Niasari, M., 2020. Toxic effects of Fe_2WO_6 nanoparticles towards microalga *Dunaliella salina*: Sonochemical synthesis nanoparticles and investigate its impact on the growth. *Chemosphere*, 258, pp. 127348.

He, S., Rong, Q., Niu, H. and Cai, Y., 2019. Platform for molecular-material dual regulation: A direct Z-scheme MOF/COF heterojunction with enhanced visible-light photocatalytic activity. *Applied Catalysis B: Environmental*, 247, pp. 49-56.

He, F., Meng, A., Cheng, B., Ho, W. and Yu, J., 2020. Enhanced photocatalytic H_2-production activity of WO_3/TiO_2 step-scheme heterojunction by graphene modification. *Chinese Journal of Catalysis*, 41, pp. 9-20.

Heidarpour, H., Padervand, M., Soltanieh, M. and Vossoughi, M., 2020. Enhanced decolorization of rhodamine B solution through simultaneous photocatalysis and persulfate activation over Fe/C_3N_4 photocatalyst. *Chemical Engineering Research and Design*, 153, pp. 709-720.

Hu, Y., Wang, X. C., Ngo, H. H., Sun, Q. and Yang, Y., 2018. Anaerobic dynamic membrane bioreactor (AnDMBR) for wastewater treatment: A review. *Bioresource technology*, 247, pp. 1107-1118.

Hu, X., Yu, Y., Chen, D., Xu, W., Fang, J., Liu, Z., Li, R., Yao, L., Qin, J. and Fang, Z., 2022. Anatase/Rutile homojunction quantum dots anchored on $g-C_3N_4$ nanosheets for antibiotics degradation in seawater matrice via coupled adsorption-photocatalysis: Mechanism insight and toxicity evaluation. *Chemical Engineering Journal*, 432, pp. 134375.

Huang, S.T., Lee, W.W., Chang, J.L., Huang, W.S., Chou, S.Y. and Chen, C.C., 2014. Hydrothermal synthesis of $SrTiO_3$ nanocubes: Characterization, photocatalytic activities, and degradation pathway. *Journal of the Taiwan Institute of Chemical Engineers*, 45, pp. 1927-1936.

Huang, C., Luo, M.T., Chen, X.F., Xiong, L., Li, X, M. and Chen, X.D., 2017. Recent advances and industrial viewpoint for biological treatment of wastewaters by oleaginous microorganisms. *Bioresource Technology*, 232, pp. 398-407.

Huang, D., Li, Z., Zeng, G., Zhou, C., Xue, W., Gong, X., Yan, X., Chen, S., Wang, W. and Cheng, M., 2019. Megamerger in photocatalytic field: 2D $g-C_3N_4$ nanosheets serve as support of 0D nanomaterials for improving photocatalytic performance. *Applied Catalysis B: Environmental*, 240, pp. 153-173.

Janani, B., Swetha, S., Syed, A., Elgorban, A. M., Zaghloul, N. S., Thomas, A. M., Raju, L.L. and Khan, S. S., 2021. Spinel FeV_2O_4 coupling on nanocube-like Bi_2O_3 for high performance white light photocatalysis and antibacterial applications. *Journal of Alloys and Compounds*, 887, pp. 161432.

Janani, B., Okla, M. K., Abdel-Maksoud, M. A., AbdElgawad, H., Thomas, A. M., Raju, L. L., Al-Qahtani, W.H. and Khan, S. S., 2022a. CuO loaded ZnS nanoflower entrapped on PVA-chitosan matrix for boosted visible light photocatalysis for tetracycline degradation and anti-bacterial application. *Journal of Environmental Management*, 306, pp. 114396.

Janani, B., Al-amri, S. S., Okla, M. K., Mohebaldin, A., Soufan, W., Almunqedhi, B., Abdel-Maksoud, M.A., AbdElgawad, H., Thomas, A.M., Raju, L.L. and Khan, S.S., 2022b. High performing pn system of $CaFe_2O_4$ coupled ZnO for synergetic degradation of Rhodamine B with white-light photocatalysis and bactericidal action. *Journal of the Taiwan Institute of Chemical Engineers*, 133, pp. 104271.

Jiang, L., Yuan, X., Zeng, G., Liang, J., Chen, X., Yu, H., Wang, H., Wu, Z., Zhang, J. and Xiong, T., 2018a. In-situ synthesis of direct solid-state dual Z-scheme WO_3/g-C_3N_4/Bi_2O_3 photocatalyst for the degradation of refractory pollutant. *Applied Catalysis B: Environmental*, 227, pp. 376-385.

Jiang, G., Cao, J., Chen, M., Zhang, X. and Dong, F., 2018b. Photocatalytic NO oxidation on N-doped TiO_2/g-C_3N_4 heterojunction: Enhanced efficiency, mechanism and reaction pathway. *Applied Surface Science*, 458, pp. 77-85.

Kishor, R., Purchase, D., Saratale, G. D., Saratale, R. G., Ferreira, L. F. R., Bilal, M., Chandra, R. and Bharagava, R. N., 2021. Ecotoxicological and health concerns of persistent coloring pollutants of textile industry wastewater and treatment approaches for environmental safety. *Journal of Environmental Chemical Engineering*, 9, pp. 105012.

Khajouei, G., O. Finklea, H. and Lin, L., 2022. UV/chlorine advanced oxidation processes for degradation of contaminants in water and wastewater: A comprehensive review. *Journal of Environmental Chemical Engineering*, 10, pp. 107508.

Khouni, I., Louhichi, G. and Ghrabi, A., 2020. Assessing the performances of an aerobic membrane bioreactor for textile wastewater treatment: Influence of dye mass loading rate and biomass concentration. *Process Safety and Environmental Protection*, 135, pp. 364-382.

Kokilavani, S., Syed, A., Rajeshwari, M. R., Subhiksha, V., Elgorban, A. M., Bahkali, A. H., Zaghloul, N.S.S., Das, A. and Khan, S. S., 2021. Decoration of Ag_2WO_4 on plate-like MnS for mitigating the charge recombination and tuned bandgap for enhanced white light photocatalysis and antibacterial applications. *Journal of Alloys and Compounds*, 889, pp. 161662.

Kong, D., Ruan, X., Geng, J., Zhao, Y., Zhang, D., Pu, X., Yao, S. and Su, C., 2021. 0D/3D $ZnIn_2S_4$/$Ag_6Si_2O_7$ nanocomposite with direct Z-scheme heterojunction for efficient photocatalytic H_2 evolution under visible light. *International Journal of Hydrogen Energy*, 46, pp. 28043-28052.

Kuila, A., Saravanan, P., Bahnemann, D. and Wang, C., 2021. Novel Ag decorated, BiOCl surface doped $AgVO_3$ nanobelt ternary composite with Z-scheme homojunction-heterojunction interface for high prolific photo switching, quantum efficiency and hole mediated photocatalysis. *Applied Catalysis B: Environmental*, 293, pp. 120224.

Kumar, R., Raizada, P., Khan, A. A. P., Nguyen, V. H., Van Le, Q., Ghotekar, S., Selvasembian, R., Gandhi, V., Singh, A. and Singh, P., 2022. Recent progress in emerging $BiPO_4$-based photocatalysts: Synthesis, properties, modification strategies, and photocatalytic applications. *Journal of Materials Science & Technology*, 108, pp. 208-225.

Li, W., Mu, B. and Yang, Y., 2019a. Feasibility of industrial-scale treatment of dye wastewater via bio-adsorption technology. *Bioresource Technology*, 277, pp. 157-170.

Li, P., Li, J., Feng, X., Li, J., Hao, Y., Zhang, J., Wang, H., Yin, A., Zhou, J., Ma, X. and Wang, B., 2019b. Metal-organic frameworks with photocatalytic bactericidal activity for integrated air cleaning. *Nature Communications*, 10, pp. 1-10.

Li, X., Garlisi, C., Guan, Q., Anwer, S., Al-Ali, K., Palmisano, G. and Zheng, L., 2021a. A review of material aspects in developing direct Z-scheme photocatalysts. *Materials Today*, 47, pp. 75-107.

Li, X., Kang, B., Dong, F., Zhang, Z., Luo, X., Han, L., Huang, J., Feng, Z., Chen, Z., Xu, J., Peng, B. and Wang, Z.L., 2021b. Enhanced photocatalytic degradation and H_2/H_2O_2 production performance of S-pCN/WO$_{2.72}$ S-scheme heterojunction with appropriate surface oxygen vacancies. *Nano Energy*, 81, pp. 105671.

Li, C.Q., Yi, S.S., Liu, Y., Niu, Z.L., Yue, X.Z. and Liu, Z.Y., 2021c. In-situ constructing S-scheme/Schottky junction and oxygen vacancy on $SrTiO_3$ to steer charge transfer for boosted photocatalytic H_2 evolution. *Chemical Engineering Journal*, 417, pp. 129231.

Li, X., Jin, Y., Dou, Z., Zhou, S., Zhang, Q. and Bao, N., 2021d. Rational design of Z-scheme $Bi_{12}O_{17}Cl_2$/plasmonic Ag/anoxic TiO_2 composites for efficient visible light photocatalysis. *Powder Technology*, 384, pp. 342-352.

Li, S., Dong, Z., Wang, Q., Zhou, X., Shen, L., Li, H. and Shi, W., 2022. Antibacterial Z-scheme $ZnIn_2S_4$/Ag_2MoO_4 composite photocatalytic nanofibers with enhanced photocatalytic performance under visible light. *Chemosphere*, 308, pp.136386.

Lin, Y., Wu, S., Li, X., Wu, X., Yang, C., Zeng, G., Peng, Y., Zhou, Q. and Lu, L., 2018. Microstructure and performance of Z-scheme photocatalyst of silver phosphate modified by MWCNTs and Cr-doped $SrTiO_3$ for malachite green degradation. *Applied Catalysis B: Environmental*, 227, pp. 557-570.

Lin, H., Long, X., An, Y. and Yang, S., 2020. In situ growth of Fe_2WO_6 on WO_3 nanosheets to fabricate heterojunction arrays for boosting solar water splitting. *The Journal of Chemical Physics*, 152, pp. 214704.

Liu, Q., Huang, J., Tang, H., Yu, X. and Shen, J., 2020. Construction 0D TiO_2 nanoparticles/2D CoP nanosheets heterojunctions for enhanced photocatalytic H_2 evolution activity. *Journal of Materials Science & Technology*, 56, pp. 196-205.

Liu, L., Chen, Z., Zhang, J., Shan, D., Wu, Y., Bai, L. and Wang, B., 2021a. Treatment of industrial dye wastewater and pharmaceutical residue wastewater by advanced oxidation processes and its combination with nanocatalysts: A review. *Journal of Water Process Engineering*, 42, pp. 102122.

Liu, X., Shen, X., Sa, B., Zhang, Y., Li, X. and Xue, H., 2021b. Piezotronic-enhanced photocatalytic performance of heterostructured $BaTiO_3$/$SrTiO_3$ nanofibers. *Nano Energy*, 89, pp. 106391.

Lops, C., Ancona, A., Di Cesare, K., Dumontel, B., Garino, N., Canavese, G., Hérnandez, S. and Cauda, V., 2019. Sonophotocatalytic degradation mechanisms of Rhodamine B dye via radicals generation by micro-and nano-particles of ZnO. *Applied Catalysis B: Environmental*, 243, pp. 629-640.

Low, J., Jiang, C., Cheng, B., Wageh, S., Al-Ghamdi, A. A. and Yu, J., 2017. A review of direct Z-scheme photocatalysts. *Small Methods*, 1, pp. 1700080.

Ma, D., Yi, H., Lai, C., Liu, X., Huo, X. and An, Z., 2021. Critical review of advanced oxidation processes in organic wastewater treatment. *Chemosphere*, 275, pp. 130104.

Ma, J., Liu, C. and Yan, K., 2022a. CQDs-MoS_2 QDs loaded on dendritic fibrous nanosilica/hydrophobic waterborne polyurethane acrylate for antibacterial coatings. *Chemical Engineering Journal*, 429, pp. 132170.

Ma, Y., Li, J., Cai, J., Zhong, L., Lang, Y. and Ma, Q., 2022b. Z-scheme g-C_3N_4/ZnS heterojunction photocatalyst: One-pot synthesis, interfacial structure regulation, and improved photocatalysis activity for bisphenol A. *Colloids and Surfaces A: Physicochemical and Engineering Aspects*, 653, pp. 130027.

Mahmoudi, F., Saravanakumar, K., Maheskumar, V., Njaramba, L.K., Yoon, Y. and Park, C.M., 2022. Application of perovskite oxides and their composites for degrading organic pollutants from wastewater using advanced oxidation processes: Review of the recent progress. *Journal of Hazardous Materials*, 436, pp. 129074.

Manikandan, S., Karmegam, N., Subbaiya, R., Devi, G.K., Arulvel, R., Ravindran, B. and Awasthi, M.K., 2020. Emerging nano-structured innovative materials as adsorbents in wastewater treatment. *Bioresource Technology*, 320, pp. 124394-124405.

Mazzanti, S., Cao, S., ten Brummelhuis, K., Völkel, A., Khamrai, J., Sharapa, D.I., Youk, S., Heil, T., Tarakina, N.V., Strauss, V. and Ghosh, I., 2021. All-organic Z-scheme photoreduction of CO_2 with water as the donor of electrons and protons. *Applied Catalysis B: Environmental*, 285, pp.119773.

Meng, A., Zhang, L., Cheng, B. and Yu, J., 2019. Dual cocatalysts in TiO_2 photocatalysis. *Advanced Materials*, 31, pp. 1807660.

Miklos, D.B., Remy, C., Jekel, M., Linden, K.G., Drewes, J.E. and Hübner, U., 2018. Evaluation of advanced oxidation processes for water and wastewater treatment-A critical review. *Water Research*, 139, pp. 118-131.

Mu, J., Teng, F., Miao, H., Wang, Y. and Hu, X., 2020. In-situ oxidation fabrication of 0D/2D SnO_2/SnS_2 novel step-scheme heterojunctions with enhanced photoelectrochemical activity for water splitting. *Applied Surface Science*, 501, pp. 143974.

Mukhtar, F., Munawar, T., Nadeem, M.S., ur Rehman, M.N., Riaz, M. and Iqbal, F., 2021. Dual S-scheme heterojunction $ZnO-V_2O_5-WO_3$ nanocomposite with enhanced photocatalytic and antimicrobial activity. *Materials Chemistry and Physics*, 263, pp. 124372-124385.

Munawar, T., Mukhtar, F., Nadeem, M.S., Mahmood, K., Hussain, A., Ali, A., Arshad, M.I., Nabi, M.A. and Iqbal, F., 2020. Structural, optical, electrical, and morphological studies of rGO anchored direct dual-Z-scheme $ZnO-Sm_2O_3-Y_2O_3$ heterostructured nanocomposite: an efficient photocatalyst under sunlight. *Solid State Sciences*, 106, pp. 106307.

Munawar, T., Mukhtar, F., Nadeem, M. S., Manzoor, S., Ashiq, M. N., Mahmood, K., Batool, S., Hasan, M. and Iqbal, F., 2022. Fabrication of dual Z-scheme $TiO_2-WO_3-CeO_2$ heterostructured nanocomposite with enhanced photocatalysis, antibacterial, and electrochemical performance. *Journal of Alloys and Compounds*, 898, pp. 162779.

Nachimuthu, S., Thangavel, S., Kannan, K., Selvakumar, V., Muthusamy, K., Siddiqui, M.R., Wabaidur, S.M. and Parvathiraja, C., 2022. *Lawsonia inermis* mediated synthesis of ZnO/Fe_2O_3 nanorods for photocatalysis – Biological treatment for the enhanced effluent treatment, antibacterial and antioxidant activities. *Chemical Physics Letters*, 804, pp. 139907.

Nagaraju, G., Udayabhanu, Shivaraj, Prashanth, S.A., Shastri, M., Yathish, K.V., Anupama, C. and Rangappa, D., 2017. Electrochemical heavy metal detection, photocatalytic, photoluminescence, biodiesel production and antibacterial activities of Ag-ZnO nanomaterial. *Materials Research Bulletin*, 94, pp. 54-63.

Naik, M.M., Naik, H.B., Nagaraju, G., Vinuth, M., Naika, H.R. and Vinu, K., 2019. Green synthesis of zinc ferrite nanoparticles in *Limonia acidissima juice*: characterization and their application as photocatalytic and antibacterial activities. *Microchemical Journal*, 146, pp. 1227-1235.

Nallapureddy, R.R., Pallavolu, M.R., Nallapureddy, J., Yedluri, A.K. and Joo, S.W., 2023. Z-scheme photocatalysis and photoelectrochemical platform with a Co_3O_4-CuO heterogeneous catalyst for the removal of water pollutants and generation of

energy. *Journal of Cleaner Production*, 382, pp. 135302.

Natarajan, T. S., Lee, J. Y., Bajaj, H. C., Jo, W.K. and Tayade, R. J., 2017. Synthesis of multiwall carbon nanotubes/TiO$_2$ nanotube composites with enhanced photocatalytic decomposition efficiency. *Catalysis Today*, 282, pp. 13-23.

Natarajan, S., Bajaj, H.C. and Tayade, R.J., 2018. Recent advances based on the synergetic effect of adsorption for removal of dyes from waste water using photocatalytic process. *Journal of Environmental Sciences*, 65, pp. 201-222.

Niu, J., Zhang, Y., Shi, J., Zhang, Z., Ma, Z., Yao, B., Yu, X. and Wang, X., 2022. Microwave-based preparation of γ-Fe$_2$O$_3$/SrTiO$_3$ photocatalyst for efficient degradation of organic pollutants in water. *Materials Chemistry and Physics*, 288, pp. 126357.

Obotey Ezugbe, E. and Rathilal, S., 2020. Membrane technologies in wastewater treatment: A review. *Membranes*, 10, pp. 89.

Pan, L., Mei, H., Zhu, G., Li, S., Xie, X., Gong, S., Liu, H., Jin, Z., Gao, J., Cheng, L. and Zhang, L., 2022. Bi selectively doped SrTiO$_3$-x nanosheets enhance photocatalytic CO$_2$ reduction under visible light. *Journal of Colloid and Interface Science*, 611, pp. 137-148.

Pang, Y., Kong, L., Chen, D. and Yuvaraja, G., 2019. Rapid Cr(VI) reduction in aqueous solution using a novel microwave-based treatment with MoS$_2$-MnFe$_2$O$_4$ composite. *Applied Surface Science*, 471, pp. 408-416.

Perreault, F., Jaramillo, H., Xie, M., Ude, M., Nghiem, L. D. and Elimelech, M., 2016. Biofouling mitigation in forward osmosis using graphene oxide functionalized thin-film composite membranes. *Environmental Science & Technology*, 50, pp. 5840-5848.

Prasannamedha, G., Senthil Kumar, P., Mehala, R., Sharumitha, T.J. and Surendhar, D., 2021. Enhanced adsorptive removal of sulfamethoxazole from water using biochar derived from hydrothermal carbonization of sugarcane bagasse. *Journal of Hazardous Materials*, 407, pp. 124825.

Priyadharsan, A., Shanavas, S., Vasanthakumar, V., Balamuralikrishnan, B. and Anbarasan, P. M., 2018. Synthesis and investigation on synergetic effect of rGO-ZnO decorated MoS$_2$ microflowers with enhanced photocatalytic and antibacterial activity. *Colloids and Surfaces A: Physicochemical and Engineering Aspects*, 559, pp. 43-53.

Priyanka, K., Remya, N. and Behera, M., 2020. Greywater treatment using modified solar photocatalyst- degradation, kinetics, pathway and toxicity analysis. *Separation and Purification Technology*, 251, pp. 117319.

Puangpetch，T., Sreethawong, T., Yoshikawa, S. and Chavadej, S., 2008. Synthesis and photocatalytic activity in methyl orange degradation of mesoporous-assembled SrTiO$_3$

nanocrystals prepared by sol-gel method with the aid of structure-directing surfactant. *Journal of Molecular Catalysis A: Chemical*, 287, pp. 70-79.

Qiao, J., Zhang, H., Li, G., Li, S., Qu, Z., Zhang, M., Wang, J. and Song, Y., 2019. Fabrication of a novel Z-scheme $SrTiO_3/Ag_2S/CoWO_4$ composite and its application in sonocatalytic degradation of tetracyclines. *Separation and Purification Technology*, 211, pp. 843-856.

Qu, Z., Liu, Z., Wu, A., Piao, C., Li, S., Wang, J. and Song, Y., 2020. Preparation of a coated Z-scheme and H-type $SrTiO_3/(BiFeO_3@ZnS)$ composite photocatalyst and application in degradation of 2, 4-dichlorophenol with simultaneous conversion of Cr (VI). *Separation and Purification Technology*, 240, pp. 116653.

Rafiq, A., Ikram, M., Ali, S., Niaz, F., Khan, M., Khan, Q. and Maqbool, M., 2021. Photocatalytic degradation of dyes using semiconductor photocatalysts to clean industrial water pollution. *Journal of Industrial and Engineering Chemistry*, 97, pp. 111-128.

Ranjit, K.T. and Viswanathan, B., 1997. Synthesis, characterization and photocatalytic properties of iron-doped TiO_2 catalysts. *Journal of Photochemistry and Photobiology A: Chemistry*, 108, pp. 79-84.

Rawal, S.B., Ojha, D.P., Do Sung, S. and Lee, W.I., 2014. Fe_2WO_6/TiO_2, an efficient visible-light photocatalyst driven by hole-transport mechanism. *Catalysis Communications*, 56, pp. 55-59.

Rehman, F., Sayed, M., Khan, J.A., Shah, N.S., Khan, H.M. and Dionysiou, D.D., 2018. Oxidative removal of brilliant green by $UV/S_2O_8^{2-}$, UV/HSO^{5-} and UV/H_2O_2 processes in aqueous media: A comparative study. *Journal of Hazardous Materials*, 357, pp. 506-514.

Sajid, M.M., Shad, N.A., Javed, Y., Khan, S.B., Zhang, Z., Amin, N. and Zhai, H., 2020. Preparation and characterization of Vanadium pentoxide (V_2O_5) for photocatalytic degradation of monoazo and diazo dyes. *Surfaces and Interfaces*, 19, pp. 100502-100511.

Şahin, Ö., Kaya, M. and Saka, C., 2015. Plasma-surface modification on bentonite clay to improve the performance of adsorption of methylene blue. *Applied Clay Science*, 116-117, pp. 46-53.

Sgroi, M., Snyder, S.A. and Roccaro, P., 2021. Comparison of AOPs at pilot scale: Energy costs for micro-pollutants oxidation, disinfection by-products formation and pathogens inactivation. *Chemosphere*, 273, pp. 128527.

Shaban, M., Ashraf, A.M. and Abukhadra, M.R., 2018. TiO_2 nanoribbons/carbon nanotubes composite with enhanced photocatalytic activity; fabrication, characterization, and application. *Scientific reports*, 8, pp. 1-17.

Shabir, M., Yasin, M., Hussain, M., Shafiq, I., Akhter, Parveen., Nizami, A., Jeon, B. and Park Y., 2022. A review on recent advances in the treatment of dye-polluted wastewater. *Journal of Industrial and Engineering Chemistry*, 112, pp. 1-19.

Shafi, Q.I., Ihsan, H., Hao, Y.F., Wu, X., Ullah, N., Younas, M., He, B.Q. and Rezakazemi, M., 2021. Multi-ionic electrolytes and *E.coli* removal from wastewater using chitosan-based in-situ mediated thin film composite nanofiltration membrane. *Journal of Environmental Management*, 294, pp.112996.

Shaheen, S., Iqbal, A., Ikram, M., Imran, M., Naz, S., Ul-Hamid, A., Shahzadi, A., Haider, J. and Haider, A., 2022. Graphene oxide-ZnO nanorods for efficient dye degradation, antibacterial and in-silico analysis. *Applied Nanoscience*, 12, pp. 165-177.

Shao, B., Liu, X., Liu, Z., Zeng, G., Liang, Q., Liang, C., Cheng, Y., Zhang, W., Liu, Y. and Gong, S., 2019. A novel double Z-scheme photocatalyst $Ag_3PO_4/Bi_2S_3/Bi_2O_3$ with enhanced visible-light photocatalytic performance for antibiotic degradation. *Chemical Engineering Journal*, 368, pp. 730-745.

Shen, H., Wei, H., Pan, Z., Lu, Y. and Wang, Y., 2017. Preparation and characterization of $SrTiO_3$-Ag/AgCl hybrid composite with promoted plasmonic visible light excited photocatalysis. *Applied Surface Science*, 423, pp. 403-416.

Shen, J., Chiang, T., Tsai, C., Jiang, Z. and Horng, J., 2022. Mechanistic insights into hydroxyl radical formation of Cu-doped ZnO/g-C_3N_4 composite photocatalysis for enhanced degradation of ciprofloxacin under visible light: Efficiency, kinetics, products identification and toxicity evaluation. *Journal of Environmental Chemical Engineering*, 10, pp. 107352.

Shetty, V., 2021. Solar light active biogenic titanium dioxide embedded silver oxide $(AgO/Ag_2O@TiO_2)$ nanocomposite structures for dye degradation by photocatalysis. *Materials Science in Semiconductor Processing*, 132, pp. 105923.

Shi, L., Zhang, Z., Wang, R., Zhou, C. and Sun, C., 2020. Synthesis and post-annealing of Ag nanoparticles decorated urchin-like $SrTiO_3$ particles for enhanced electron/hole separation and photocatalytic activity. *Ceramics International*, 46, pp. 19460-19468.

Siddiqui, M.F., Singh, L. and Wahid, Z.A., 2017. Treatment of dye wastewater for water reuse wsing membrane bioreactor and biofouling control. *Waste Biomass Management – A Holistic Approach*, 8, pp. 121-136.

Sin, J.C., Lam, S.M., Zeng, H., Lin, H., Li, H., Tham, K.O., Mohamed, A.R., Lim, J.W. and Qin, Z., 2021. Magnetic $NiFe_2O_4$ nanoparticles decorated on N-doped BiOBr nanosheets for expeditious visible light photocatalytic phenol degradation and hexavalent chromium reduction via a Z-scheme heterojunction mechanism. *Applied Surface Science*, 559, pp. 149966-149981.

Singh, N.B., Nagpal, G. and Agrawal, S., 2018. Water purification by using adsorbents:

A review. *Environmental Technology & Innovation*, 11, pp. 187-240.

Stelo, F., Kublik, N., Ullah, S. and Wender, H., 2020. Recent advances in Bi_2MoO_6 based Z-scheme heterojunctions for photocatalytic degradation of pollutants. *Journal of Alloys and Compounds*, 829, pp. 154591.

Sun, D., Mao, J., Cheng, L., Yang, X., Li, H., Zhang, L., Zhang, W., Zhang, Q. and Li, P., 2021. Magnetic g-C_3N_4/$NiFe_2O_4$ composite with enhanced activity on photocatalytic disinfection of *Aspergillus flavus*. *Chemical Engineering Journal*, 418, pp. 129417.

Sun, H., Zou, C. and Liang, H., 2022a. Designing dual-defective photocatalyst of Z-scheme H-$BiVO_4$/D-NG composite with hollow structures for efficient visible-light photocatalysis of organic pollutants. *Separation and Purification Technology*, 297, pp. 121476.

Sun, H., Zou, C. and Tang, W., 2022b. Designing double Z-scheme heterojunction of g-C_3N_4/Bi_2MoO_6/Bi_2WO_6 for efficient visible-light photocatalysis of organic pollutants. *Colloids and Surfaces A: Physicochemical and Engineering Aspects*, 654, pp. 130105.

Syed, A., Bahkali, A. H. and Elgorban, A. M., 2021a. Enhanced antibacterial and visible light driven photocatalytic activity of $CaFe_2O_4$ doped CdO heterojunction nanohybrid particles prepared by sono-chemical method. *Optical Materials*, 113, pp. 110595.

Syed, A., Elgorban, A.M. and Al Kheraif, A.A., 2021b. High performance nanohybrid CeO2@2D CdO plates with suppressed charge recombination: Insights of photoluminescence, visible-light photocatalysis, intrinsic mechanism and antibacterial activity. *Optical Materials*, 121, pp. 111510.

Tan, H.L., Abdi, F.F. and Ng, Y.H., 2019. Heterogeneous photocatalysts: an overview of classic and modern approaches for optical, electronic, and charge dynamics evaluation. *Chemical Society Reviews*, 48, pp. 1255-1271.

Tang, Y., Qin, Z., Zhong, Y., Yin, S., Liang, S. and Sun, H., 2022. Three-phase interface photocatalysis for the enhanced degradation and antibacterial property. *Journal of Colloid and Interface Science*, 612, pp. 194-202.

Thambiliyagodage, C., 2022. Efficient photocatalysis of carbon coupled TiO_2 to degrade pollutants in wastewater-A review. *Environmental Nanotechnology, Monitoring & Management*, 18, pp. 100737.

Tshangana, C., Chabalala, M., Muleja, A., Nxumalo, E. and Mamba, B., 2020. Shape-dependant photocatalytic and antimicrobial activity of ZnO nanostructures when conjugated to graphene quantum dots. *Journal of Environmental Chemical Engineering*, 8, pp.103930.

Tuipulotu, D.E., Mathur, A., Ngo, C. and Man, S.M., 2021. *Bacillus cereus*: epidemiology,

virulence factors, and host–pathogen interactions. *Trends in Microbiology*, 29, pp. 458-471.

Valian, M., Soofivand, F., Yusupov, M. M. and Salavati-Niasari, M., 2022. Facile synthesis of $SrTiO_3$/$CoAlMnO_4$ nanocomposite: A rechargeable heterojunction photocatalyst with superior hydrogen storage capability. *International Journal of Hydrogen Energy*, 47, pp. 31624-31637.

Vasantharaj, S., Sathiyavimal, S., Senthilkumar, P., Kalpana, V.N., Rajalakshmi, G., Alsehli, M., Elfasakhany, A. and Pugazhendhi, A., 2021. Enhanced photocatalytic degradation of water pollutants using bio-green synthesis of zinc oxide nanoparticles (ZnO NPs). *Journal of Environmental Chemical Engineering*, 9, pp. 105772.

Veisi, P., Dorraji, M.S.S., Rasoulifard, M.H., Ghaffari, S. and Choobar, A.K., 2021. Synergistic photocatalytic-adsorption removal effect of $NiFe_2O_4$-Zn-Al mixed metal oxide composite under visible-light irradiation. *Journal of Photochemistry and Photobiology A: Chemistry*, 414, pp.113268-113283.

Venieri, D., Gounaki, I., Bikouvaraki, M., Binas, V., Zachopoulos, A., Kiriakidis, G. and Mantzavinos, D., 2017. Solar photocatalysis as disinfection technique: Inactivation of Klebsiella pneumoniae in sewage and investigation of changes in antibiotic resistance profile. *Journal of environmental management*, 195, pp. 140-147.

Vieira, W.T., de Farias, M.B., Spaolonzi, M.P., da Silva, M.G.C. and Vieira, M.G.A., 2020. Removal of endocrine disruptors in waters by adsorption, membrane filtration and biodegradation. A review. *Environmental Chemistry Letters*, 18, pp. 1113-1143.

Vignesh, S., Suganthi, S., Sundar, J.K., Raj, V. and Devi, P.R.I., 2019. Highly efficient visible light photocatalytic and antibacterial performance of PVP capped Cd: Ag: ZnO photocatalyst nanocomposites. *Applied Surface Science*, 479, pp. 914-929.

Vigneshwaran, S., Sirajudheen, P., Nabeena, C.P., Sajna, V.P. and Meenakshi, S., 2021. Photocatalytic performance of chitosan tethered magnetic Fe_2O_3-like (3D/2D) hybrid for the dynamic removal of anionic dyes: Degradation and mechanistic pathways. *International Journal of Biological Macromolecules*, 183, pp. 2088-2099.

Vigneshwaran, S., Sirajudheen, P. and Meenakshi, S., 2022. Surface activated mesoporous Ag-Fe_3O_4 tethered chitosan nanomatrix heterojunction photocatalyst for organic dyes degradation: Performance, recycling, and mechanism. *Environmental Nanotechnology, Monitoring & Management*, 17, pp. 100654.

Wang, W., Wang, H., Li, G., An, T., Zhao, H. and Wong, P. K., 2019. Catalyst-free activation of persulfate by visible light for water disinfection: efficiency and mechanisms. *Water research*, 157, pp. 106-118.

Wang, J., Wang, G., Cheng, B., Yu, J. and Fan, J., 2020a. Sulfur-doped g-C_3N_4/TiO_2 S-scheme heterojunction photocatalyst for Congo Red photodegradation. *Chinese*

Journal of Catalysis, 42, pp. 56-68.

Wang, W., Feng, H., Liu, J., Zhang, M., Liu, S., Feng, C. and Chen, S., 2020b. A photo catalyst of cuprous oxide anchored MXene nanosheet for dramatic enhancement of synergistic antibacterial ability. *Chemical Engineering Journal*, 386, pp. 124116-124128.

Wang, X., Jiang, L., Li, K., Wang, J., Fang, D., Zhang, Y., Tian, D., Zhang, Z. and Dionysiou, D.D., 2020c. Fabrication of novel Z-scheme $SrTiO_3/MnFe_2O_4$ system with double-response activity for simultaneous microwave-induced and photocatalytic degradation of tetracycline and mechanism insight. *Chemical Engineering Journal*, 400, pp.125981.

Wang, J., Wang, G., Cheng, B., Yu, J. and Fan, J., 2021a. Sulfur-doped g-C_3N_4/TiO_2 S-scheme heterojunction photocatalyst for Congo Red photodegradation. *Chinese Journal of Catalysis*, 42, pp. 56-68.

Wang, Q., Zhou, X., Ji, S., Li, S., Gu, J., Shen, L., Liu, P., Yin, J., Xu, G. and Shi, W., 2021b. Synthesis and photocatalysis of novel Z-scheme CeO_2/Ag-$AgVO_3$ heterojunction nanofibers and their efficient antibacterial properties. *Journal of Environmental Chemical Engineering*, 9, pp. 106498.

Wang, H., Li, Xin., Zhao, X., Li, C., Song, X., Zhang, P., Huo, P. and Li, X., 2022. A review on heterogeneous photocatalysis for environmental remediation: From semiconductors to modification strategies. *Chinese Journal of Catalysis*, 43, pp. 178-214.

Wen, X. J., Niu, C. G., Zhang, L., Liang, C. and Zeng, G. M., 2017. An in depth mechanism insight of the degradation of multiple refractory pollutants via a novel $SrTiO_3$/BiOI heterojunction photocatalysts. *Journal of Catalysis*, 356, pp. 283-299.

Wu, J., Xiong, L., Hu, Y., Yang, Y., Zhang, X., Wang, T., Tang, Z., Sun, A., Zhou, Y., Shen, J. and Zou, Z., 2021. Organic half-metal derived erythroid-like $BiVO_4$/hm-C_4N_3 Z-scheme photocatalyst: Reduction sites upgrading and rate-determining step modulation for overall CO_2 and H_2O conversion. *Applied Catalysis B: Environmental*, 295, pp.120277.

Wu, X., Wang, X., Xie, Y., Ren, N., Ma, J., Ning, P., 2022. Facile in-situ construction of highly dispersed nano zero-valent iron modified black TiO_2 Z-scheme recyclable heterojunction with highly efficient visible-light-driven photocatalytic activity. *Applied Catalysis B: Environmental*, 310, pp. 121325.

Xia, Y., He, Z., Lu, Y., Tang, B., Sun, S., Su, J. and Li, X., 2018. Fabrication and photocatalytic property of magnetic $SrTiO_3/NiFe_2O_4$ heterojunction nanocomposites. *RSC advances*, 8, pp. 5441-5450.

Xia, Z. and Hu, L., 2019. Treatment of organics contaminated wastewater by ozone micro-

nano-bubbles. *Water*, 11, pp. 55.

Xia, P., Cao, S., Zhu, B., Liu, M., Shi, M., Yu, J. and Zhang, Y., 2020. Designing a 0D/2D S-scheme heterojunction over polymeric carbon nitride for visible-Light photocatalytic inactivation of bacteria. *Angewandte Chemie-International Edition*, 59, pp. 5218-5225.

Xie, L., Ren, Z., Zhu, P., Xu, J., Luo, D. and Lin, J., 2021. A novel CeO_2-TiO_2/PANI/$NiFe_2O_4$ magnetic photocatalyst: Preparation, characterization and photodegradation of tetracycline hydrochloride under visible light. *Journal of Solid State Chemistry*, 300, pp. 122208-122219.

Xu, T., Zou, R., Lei, X., Qi, X., Wu, Q., Yao, W. and Xu, Q., 2019. New and stable g-C_3N_4/HAp composites as highly efficient photocatalysts for tetracycline fast degradation. *Applied Catalysis B: Environmental*, 245, pp. 662-671.

Xu, J., Olvera-Vargas, H., Loh, B.J.H. and Lefebvre, O., 2020. FTO-TiO_2 photoelectrocatalytic degradation of triphenyltin chloride coupled to photoelectro-Fenton: A mechanistic study. *Applied Catalysis B: Environmental*, 271, pp. 118923.

Xu, Q., Zhang, L., Cheng, B., Fan, J. and Yu, J., 2020. S-scheme heterojunction photocatalyst. *Chem*, 6, pp. 1543-1559.

Xu, G., Du, M., Li, T., Guan, Y. and Guo, C., 2021. Facile synthesis of magnetically retrievable Fe_3O_4/$BiVO_4$/CdS heterojunction composite for enhanced photocatalytic degradation of tetracycline under visible light. *Separation and Purification Technology*, 275, pp. 119157.

Xu, K., Shen, X., Ji, Z., Yuan, A., Kong, L., Zhu, G. and Zhu, J., 2021. Highly monodispersed Fe_2WO_6 micro-octahedrons with hierarchical porous structure and oxygen vacancies for lithium storage. *Chemical Engineering Journal*, 413, pp. 127504.

Xu, Y., Lin, W., Yuan, D., Chen, S., Li, F., Long, Y., He, C., Zhao, W. and Zhao, C., 2022. "1+ 1> 2": Highly efficient removal of organic pollutants by composite nanofibrous membrane based on the synergistic effect of adsorption and photocatalysis. *Journal of Materials Science & Technology*, 124, pp. 76-85.

Xue, Y., Chang, Q., Hu, X., Cai, J. and Yang, H., 2020. A simple strategy for selective photocatalysis degradation of organic dyes through selective adsorption enrichment by using a complex film of CdS and carboxylmethyl starch. *Journal of Environmental Management*, 274, pp. 111184.

Xue, Y., Tang, W., Si, C., Lu, Q., Guo, E., Wei, M. and Pang, Y., 2022. 0D/2D/1D silver-decorated CuPc/Bi_2MoO_6 Z-scheme heterojunctions enable better visible-light-driven tetracycline photocatalysis. *Optical Materials*, 128, pp. 112400.

Yang, Q., Ma, Y., Chen, F., Yao, F., Sun, J., Wang, S., Yi, K., Hou, L., Li, X. and Wang, D.,2019. Recent advances in photo-activated sulfate radical-advanced oxidation

process (SR-AOP) for refractory organic pollutants removal in water. *Chemical Engineering Journal*, 378, pp. 122149.

Yang, Y., Ashraf, M.A., Fakhri, A., Gupta, V.K. and Zhang, D., 2021. Facile synthesis of gold-silver/copper sulfide nanoparticles for the selective/sensitive detection of chromium, photochemical and bactericidal application. *Spectrochimica Acta Part A: Molecular and Biomolecular Spectroscopy*, 249, pp. 119324.

Yang, Z.Y., Yuan,Y., Li, E.Z. and Zhang, S.R., 2023. Ultra-high dielectric constant and thermal conductivity $SrTiO_3$@VTMS/PB composite for microwave substrate application. Applied Surface Science, 622, pp. 156888.

Yao, X., Hu, X., Zhang, W., Gong, X., Wang, X., Pillai, S. C., D.Dionysiou, D. and Wang, D., 2020. Mie resonance in hollow nanoshells of ternary TiO_2-Au-CdS and enhanced photocatalytic hydrogen evolution. *Applied Catalysis B: Environmental*, 276, pp. 119153.

Ye, S., Yan, M., Tan, X., Liang, J., Zeng, G., Wu, H., Song, B., Zhou, C., Yang, Y. and Wang, H., 2019. Facile assembled biochar-based nanocomposite with improved graphitization for efficient photocatalytic activity driven by visible light. *Applied Catalysis B: Environmental*, 250, pp. 78-88.

Yu, X., Wang, J., Fu, X., Meng, H., Zhu, Y. and Zhang, Y., 2020. Construction of Z-scheme $SrTiO_3$/Ag/Ag_3PO_4 photocatalyst with oxygen vacancies for highly efficient degradation activity towards tetracycline. *Separation and Purification Technology*, 241, pp. 116718.

Yu, Y., Hu, X., Li, M., Fang, J., Leng, C., Zhu, X., Xu, W., Qin, J., Yao, L., Liu, Z. and Fang, Z., 2022. Constructing mesoporous Zr-doped SiO_2 onto efficient Z-scheme TiO_2/g-C_3N_4 heterojunction for antibiotic degradation via adsorption-photocatalysis and mechanism insight. *Environmental Research*, 214, pp. 114189.

Yuan, J., Huang, X., Zhang, L., Gao, F., Lei, R., Jiang, C., Feng, W. and Liu, P., 2020. Tuning piezoelectric field for optimizing the coupling effect of piezo-photocatalysis. *Applied Catalysis B: Environmental*, 278, pp.119291.

Yurtsever, A., Basaran, E., Ucar, D. and Sahinkaya, E., 2021. Self-forming dynamic membrane bioreactor for textile industry wastewater treatment. *Science of The Total Environment*, 751, pp. 141572.

Zeng, B., Wang, S., Feng, Z., Xiao, Y., Li, M., Hong, F., Zhao, Y., Feng, Z., Li, R. and Li, C., 2022. Atomically unraveling the dependence of surface microstructure on plasmoninduced hydrogen evolution on Au/$SrTiO_3$. *Nano Energy*, 91, pp. 2022.

Zhang, W. and Jiang, F., 2019. Membrane fouling in aerobic granular sludge (AGS)-membrane bioreactor (MBR): Effect of AGS size. *Water research*, 157, pp. 445-453.

Zhang, X., Jia, X., Duan, P., Xia, R., Zhang, N., Cheng, B., Wang, Z. and Zhang, Y., 2021a. V_2O_5/Pg-C_3N_4 Z-scheme enhanced heterogeneous photocatalytic removal of methyl orange from water under visible light irradiation. *Colloids and Surfaces A: Physicochemical and Engineering Aspects*, 608, pp. 125580-125591.

Zhang, N., Qiao, S., Wu, H., Fakhri, A. and Gupta, V.K., 2021b. Sustainable nano-composites polyglutamic acid functionalized Ag/g-C_3N_4/SiC for the ultrasensitive colorimetric assay, visible light irradiated photocatalysis and antibacterial efficiency. *Optical Materials*, 120, pp. 111452.

Zhang, W., Xiang, Y., Li, X., Huang, X. and Qian, X., 2022a. Construction of oxygen vacancy mediated direct Z scheme Bi_2WO_6/$SrTiO_3$ hybrid on cellulose fibers for high-performance and recyclable photocatalytic paper. *Journal of Colloid and Interface Science*, 622, pp. 40-49.

Zhang, Y., Li, Y., Ruan, Z., Yuan, Y. and Lin, K., 2022b. Extensive solar light utilizing by ternary C-dots/Cu_2O/$SrTiO_3$: Highly enhanced photocatalytic degradation of antibiotics and inactivation of *E. coli*. *Chemosphere*, 290, pp.133340.

Zhang, Y., Liu, C., Zhou, Y., Wang, J., Li, A. and Corvini, P.F.X., 2023. Boosting light harvesting and charge separation over hollow double-shelled Ag@ $SrTiO_3$-TiO_2 with Z-scheme heterostructure for highly efficient photocatalytic reduction of nitrate to N_2. *Chemical Engineering Journal*, 457, pp.140992.

Zhao, F., Liu, Y., Hammouda, S. Ben, Doshi, B., Guijarro, N., Min, X., Tang, C. J., Sillanpää, M., Sivula, K. and Wang, S., 2020. MIL-101(Fe)/g-C_3N_4 for enhanced visible-light-driven photocatalysis toward simultaneous reduction of Cr(VI) and oxidation of bisphenol A in aqueous media. *Applied Catalysis B: Environmental*, 272, pp. 119033.

Zhao, G., Ding, J., Zhou, F., Chen, X., Wei, L., Gao, Q., Wang, K. and Zhao, Q., 2021. Construction of a visible-light-driven magnetic dual Z-scheme $BiVO_4$/gC_3N_4/$NiFe_2O_4$ photocatalyst for effective removal of ofloxacin: Mechanisms and degradation pathway. *Chemical Engineering Journal*, 405, pp. 126704-126719.

Zhu, P., Chen, Y., Duan, M., Liu, M. and Zou, P., 2018. Structure and properties of Ag_3PO_4/diatomite photocatalysts for the degradation of organic dyes under visible light irradiation. *Powder Technology*, 336, pp. 230-239.

Zhou, M., Chen, J., Zhang, Y., Jiang, M., Xu, S., Liang, Q. and Li, Z., 2020. Shape-controlled synthesis of golf-like, star-like, urchin-like and flower-like $SrTiO_3$ for highly efficient photocatalytic degradation and H_2 production. *Journal of Alloys and Compounds*, 817, pp. 152796.

Zhou, G., Meng, L., Ning, X., Yin, W., Hou, J., Xu, Q., Yi, J., Wang, S. and Wang, X., 2022. Switching charge transfer of g-C_3N_4/$BiVO_4$ heterojunction from type II to Z-scheme via interfacial vacancy engineering for improved photocatalysis. *International*

Journal of Hydrogen Energy, 47, pp. 8749-8760.

Zuo, J., Wang, B., Kang, J., Yan, P., Shen, J., Wang, S., Fu, D., Zhu, X., She, T., Zhao, S. and Chen, Z., 2022. Activation of peroxymonosulfate by nanoscaled $NiFe_2O_4$ magnetic particles for the degradation of 2,4-dichlorophenoxyacetic acid in water: Efficiency, mechanism and degradation pathways. *Separation and Purification Technology*, 297, pp. 121459.

PUBLICATION

Zhao, L., Lam, S. M., Ong, Y. T., Sin, J. C., Zeng, H., Xie, Q. and Lim, J. W., 2022. Fe_2WO_6 coupling on cube-like $SrTiO_3$ as a highly active S-scheme heterojunction composite for visible light photocatalysis and antibacterial applications. *Environmental Technology & Innovation*, 28, pp. 102941.